ABSTRACT

DEVELOPMENT OF LOW ALLOY STEEL BY DIRECT METAL LASER SINTERING
by
Elias Jelis

The US Department of Defense is interested in developing, understanding, and optimizing process parameters for low alloy (4340/4140 steel) for the powder bed fusion process. Low alloy steel is used in parts where high strength and toughness are required. During parameter optimization, several aspects of the process are investigated. Powder size and morphology optimization is important for manufacturability because adequate packing is required to produce full density components. Microstructure evaluation is used in order to provide insight into parameters that lead to optimal mechanical performance and recoating performance. Influence of residual stress is evaluated with this process. Large thermal stress can lead to high distortion and deflection. A general corrosion study is conducted on direct metal laser sintered parts in order to evaluate the factors which lead to corrosion. The main objectives of this effort are to produce mechanical properties of steel that are comparable to wrought 4340 and to understand the factors which influence the qualification of the powder bed fusion process.

DEVELOPMENT OF LOW ALLOY STEEL BY DIRECT METAL LASER SINTERING

by
Elias Jelis

A Dissertation
Submitted to the Faculty of
New Jersey Institute of Technology
in Partial Fulfillment of the Requirements for the Degree of
Doctor of Philosophy in Materials Science and Engineering

Interdisciplinary Program in Materials Science and Engineering

January 2017

.

APPROVAL PAGE

DEVELOPMENT OF LOW ALLOY STEEL BY DIRECT METAL LASER SINTERING

Elias Jelis

Dr. Nuggehalli M. Ravindra, Dissertation Advisor — Date
Professor of Physics, NJIT

Dr. Eon Soo Lee, Committee Member — Date
Assistant Professor of Mechanical and Industrial Engineering, NJIT

Dr. Siva Nadimpalli, Committee Member — Date
Assistant Professor of Mechanical and Industrial Engineering Department, NJIT

Dr. Michael Jaffe, Committee Member — Date
Research Professor of Biomedical Engineering, NJIT

Stacey Clark, Committee Member — Date
Deputy Director, Systems Engineering, US ARMY RDECOM

Donald Skelton, Committee Member — Date
Branch Chief of Advanced Materials Technology Branch,
US ARMY RDECOM-ARDEC

BIOGRAPHICAL SKETCH

Author: Elias Jelis

Degree: Doctor of Philosophy

Date: January 2017

Undergraduate and Graduate Education:

- Doctor of Philosophy in Materials Science and Engineering,
  New Jersey Institute of Technology, Newark, NJ, 2017

- Master of Science in Ceramics and Materials Science and Engineering,
  Rutgers University, New Brunswick, NJ 2007

- Bachelor of Science in Biomedical Engineering,
  New Jersey Institute of Technology, Newark, NJ, 2005

Major: Materials Science and Engineering

Presentations and Publications:

E. Jelis, R. Sadangi, M. Hespos, S. Kerwien, M. Clemente and N. Ravindra, "DMLS (Direct Metal Laser Sintering) 4340 Steel: Influence of Starting Particle Size," in *Materials Science and Technology*, Columbus, OH, 2015.

D. P. Schmidt, E. Jelis and M. Clemente, "Corrosion of 3D Printed Steel," in *Materials Science and Technology 2015*, Columbus, OH, 2015.

E. Jelis, M. Clemente, S. Kerwien, R. Nuggehalli and M. R. Hespos,"Metallurgical and Mechanical Evaluation of 4340 Steel Produced by Direct Metal Laser Sintering," *The Journal of Minerals, Metals, and Material Society* vol. 67, no. 3, pp. 582-589, 2015.

E. Jelis, S. Kerwien, N. M. Ravindra and M. Clemente, "Development of Low Alloy High Strength Steel Process Parameters for Direct Metal Laser Sintering,"in *Materials Science and Technology 2015*, Pittsburgh, PA 2014.

ACKNOWLEDGMENT

I would like to express my appreciation to my advisor Dr. Nuggehalli M. Ravindra for his continued and consistent support of my PhD study. His patience and knowledge was instrumental for the completion of my PhD. I would like to also thank my committee members: Dr. Eon Soo Lee, Dr. Siva Nadimpalli, Dr. Michael Jaffe, Ms. Stacey Clark, and Mr. Donald Skelton for providing valuable feedback on the project.

I appreciate the generous financial support from the DoD SMART Program, and U.S ARMY ARDEC.

I would also like to recognize Mr. Matthew Clemente, Mr. Michael Hespos, and Dr. Rajendra Sadangi from U.S. Army ARDEC for providing valuable technical expertise. The successful completion of the Dissertation would not have been possible without everyone aforementioned.

Finally, I would like to express gratitude to my wife and family for their unwavering love and support which was critical for the completion of my dissertation.

TABLE OF CONTENTS

TABLE OF CONTENTS
(Continued)

TABLE OF CONTENTS
(Continued)

TABLE OF CONTENTS
(Continued)

LIST OF TABLES

LIST OF TABLES
(Continued)

LIST OF TABLES
(Continued)

LIST OF FIGURES

LIST OF FIGURES
(Continued)

Figure **Page**

LIST OF FIGURES
(Continued)

Figure **Page**

LIST OF FIGURES
(Continued)

LIST OF FIGURES
(Continued)

LIST OF SYMBOLS

©	Copyright
L-PBF	Laser Powder Bed Fusion
μm	micrometers (10^{-6} meters)
DMLS	Direct Metal Laser Sintering
CO_2	Carbon Dioxide
AM	Additive Manufactured
mm/sec	Millimeters per second
wt%	Weight percent
g/sec	grams per second
J/mm^3	Joules per cubic millimeter
%	Percent
g/cm^3	Grams per cubic centimeter
TTT	Time Temperature Transformation
D10	Ten percent cumulative volume
D50	Fifty percent cumulative volume
D90	Ninety percent cumulative volume

CHAPTER 1

INTRODUCTION

1.1 Objective

The objective of this research is to understand the influence of process parameters and design criteria on the properties of low alloy steel. From the lessons learned, this effort will provide the necessary foundation for developing a manufacturing guide to produce mechanically sound parts for low alloy steels and a methodology for process parameter development that can be applied to other materials.

1.2 Current State of Technology

DMLS (Direct Metal Laser Sintering) is a laser powder bed fusion (L-PBF) process by which laser fuses powder (full melting) layer by layer in succession until the part is built. The DMLS process is as follows: a stereolithography file (.stl) of the part is loaded to the process software. Then the software is used to place and orient the part, along with support structures, with respect to the build plate to account for overhanging features. The machine software then creates slice files for the components which can then be used by the machine software to build the part. The slices are dependent on the layer thickness (20-50μm) provided by the machine.

Fiber laser sources have enabled the DMLS technology to advance because the powder beds absorb more laser energy than a CO_2 laser sources can produce. Fiber laser sources can fully melt the metallic powder in significantly less time than CO_2 lasers. Adequate energy which is defined by equation (1.1) [1], below, must be delivered to the

powder bed in order for full melting to occur. Hatch distance is the distance between center to center of the laser beam. In this discussion, the stripe scan strategy will be used. Stripe width can be described as scan vector. Stripe width and hatch distance are illustrated in Figure 1.1.

$$E = P/(t*v*d) \tag{1.1}$$

where, E is the volumetric applied energy density, P is laser power, t is layer thickness, d is Hatch Distance; and v is Laser Scan Speed

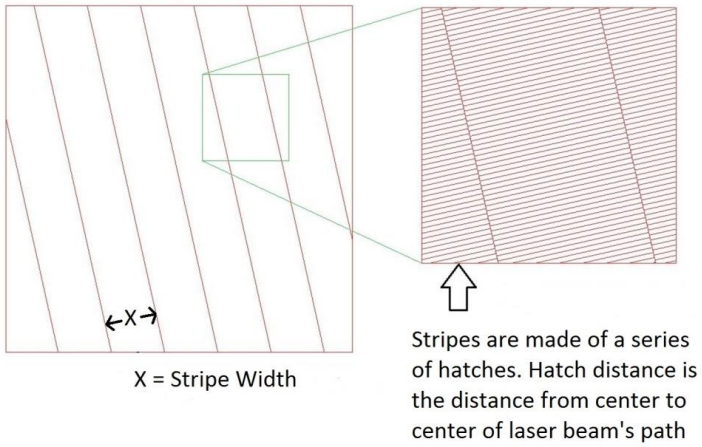

Figure 1.1 Image illustrating the hatch distance and stripe width
Source: [2].

A major advantage of the process is that no additional tooling is needed and the process can handle extremely complex parts without the need for any welding or post-processing [3]. It can build near net, complex geometries which are not attainable by traditional manufacturing processes. Geometries such as lattice structures, molds with conformal cooling channels can be built with this process [4] [5]. Several dissimilar small parts can be built simultaneously on the same build plate – the process is called parallel production [6].

DMLS can also reduce part counts by building multiple parts into one assembly. Previously, impellers were made out of multiple pieces welded together [7]. Now, impellers can be made into one solid component using DMLS. Thus, the mechanical properties of the impeller are more uniform. Furthermore, the lead time for the impellers is significantly less using additive manufacturing rather than producing them by subtractive manufacturing.

Geometries are limited in DMLS because the use of supports are needed for overhanging features and small angles from the horizontal. The support areas are critical for both anchoring the part onto the build plate and providing heat dissipation [8]. For anchoring the parts to the build plate, the supports need to be strong enough to prevent the part from warping [9]. If the supports are only used to provide heat dissipation for overhanging features, they can be offset slightly (~60 microns) below the feature, making them easier to remove. The designer must account for the supports and their removal prior to the build operation.

In addition, the surface roughness of the DMLS compnents are significantly higher than machining. As a result, post machining is needed to reduce the roughness and hold tolerances for critical features such as holes, screw holes, and other parts which have tight tolerances.

1.3 Brief Description of the Sintering Machine

The EOSINT M270 is manufactured by EOS. Basic operation of the machine is as follows: the dispensing bin rises and a ceramic recoating blade pushes the powder over the build platform (Figure 1.2). The excess powder is collected by the collector bin. After the laser

scanning is complete, the recoating blade returns back to its original position and the build platform lowers itself by a layer thickness. Another important factor in the recoating process is that full coverage and adequate packing is needed in order to minimize defects.

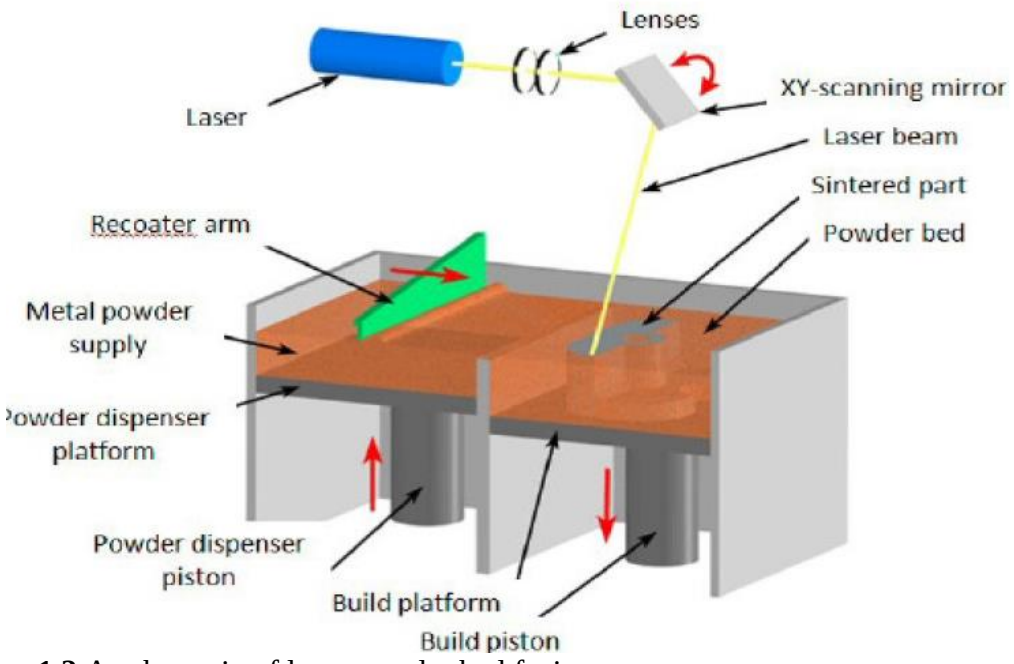

Figure 1.2 A schematic of laser powder bed fusion process.
Source: [10].

The recommended inert gas for steel in the EOS machine is nitrogen. Furthermore, the operator loads the powder from the front of the M270 machine. Thus, the powder is exposed to an air environment during process chamber clean up, part removal, and build stoppage. The temperture of the chamber in the EOSINT M270 during the build is 80^{o}C.

1.4 Mechanical Properties of Steel Alloys Manufactured by L-PBF

Preferred materials for the L-PBF process are alloys that are weldable. For instance, aluminum alloys 6061 and 7075 are difficult to manufacture by laser powder bed fusion and difficult to weld as well [11] [12]. Both materials are susceptible to hot cracking. For

the materials qualified by the manufacturer, the mechanical properties are comparable to wrought. The qualified materials include: Ti-6Al-4V, 17-4 and 15-5 stainless steel, 316L stainless, aluminum alloy Al10SiMg, Inconel 625 and 718, 300 maraging steel, and several others. The process produces components that are near full density. Thus, the mechanical properties of materials made by this process are comparable to their wrought counterparts after heat treatment. Post processing is typically needed for DMLS parts. At a minimum, stress relief is needed prior to part removal to prevent significant part warping once it is removed from the plate. Typically, parts produced by laser sintering, without post processing, do not have the desired mechanical behavior because of the rapid phase transformations of the material. Heat treatment is generally required for the parts to obtain the desired mechanical properties (Table 1.1). For example, 17-4 stainless steel produced using default parameters in a nitrogen environment, with powder supplied by EOS, contains retained austenite [13]. Thus, the samples need to be solutionized with possible cryogenic treatment to produce the martensitic structure needed for the copper to precipitate during precipitation hardening. Copper does not precipitate in an austenitic structure easily because it is highly soluble in the austenite phase. Likewise, other materials, such as maraging steel, would need heat treatment to obtain the desired strength.

As a result, the potential to use metal AM (Additive Manufactured) components to produce functional parts increases in accordance with the steel mechanical properties, summarized in Table 1.1. However, the elongation of maraging steel is significantly lower than typical wrought values after heat treatment. Previous studies suggest that the largest concentration of oxygen is towards the outside of the melt pool in maraging steel 300. Titanium and aluminum oxide inclusions may reduce the performance of the maraging

steel. The elongation is significantly lower than wrought after the part is aged [14]. It may be possible to develop 4340 with ductility comparable to wrought because, unlike maraging steel 300, it does not contain elements which readily acquire oxygen to form significant oxide inclusions.

Table 1.1 Mechanical Properties of Steels Manufactured by L-PBF Versus Wrought

Material/condition	**Yield strength** ksi	**Tensile Strength** ksi	**Elongation** %
300 Maraging steel/age hardened	289	297	2-6 % [15]
300 Maraging steel/ typical wrought	281.6	290	8.6 % [16]
15-5 Stainless DMLS/precipitation hardened H900	182.9	207.1	13.2% [17]
15-5 Stainless/ typical wrought H900	201	209	10.1 % [18]
17-4 Stainless steel/ precipitation DMLS hardened H900	182.9	206.3	11.9% [17]
17-4 Stainless steel/ precipitation hardened wrought H900	185	200	14% [19]

CHAPTER 2

POWDER EVALUATION

2.1 Overview

This chapter will discuss the benefits of the optimization of gas atomized 4340 for this process. Powder size optimization is important for optimal density of the part produced by this process. Microstructure and powder performance analyses will determine an effective particle size range for the process.

2.2 Gas Atomization Process and Performance

The powder used for the DMLS process is typically gas atomized. The gas atomization process is as follows: The solid metal, which can be certifiable scrap material or bar stock is melted, in a vacuum or inert gas to minimize exposure to air. The melt is then introduced to a jet of inert gas which breaks up the melt into individual particles (Figure 2.1a). The gas source has a relatively low thermal conductivity allowing the particles to develop a spherical morphology.

There also have been powders which have been water atomized. Although the particles are fairly spherical, the oxygen content in the powder is typically higher [20]. A high oxygen concentration may lead to balling effect of the melt pool during laser interaction [21].

The gas atomized particles are preferred because they lead to better packing efficiency and have adequate flow [22]. Afterwards, the powder is sieved so that the coarse particle boundary is met (Figure 2.1b). Since the powder is relatively fine, the particles are

air classified to remove the finer particles. The particles are then blended together so that particle sizes are as evenly distributed as possible. The size of the particles is typically less than 60 microns.

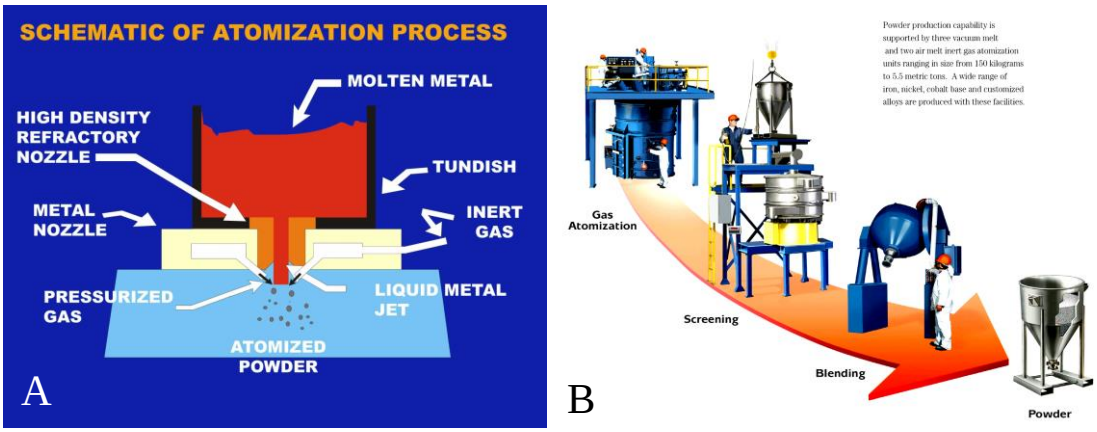

Figure 2.1 Schematic of gas atomization process.
Source: [23].

A major challenge with the DMLS process is the qualification of the powder. Different powder size distributions will lead to different packing densities. The issue is how tight of a powder size distribution is required in order to produce parts with similar mechanical performance. If the laser parameters are the same, there is a limited powder size range which can be melted effectively. For instance, stainless steel 316L powder with a narrower distribution (15-45μm) has a lower part density than the wider size distribution (0-45μm) at higher scan speeds with a power of 50 W. Another conclusion is that the evaporation of smaller particles can be caused by over exposure because the density is lower at slower scan speeds for powder with finer particle size [24]. In addition, packing must be sufficient so that smaller particles can fit in the voids for effective melting from

heat conduction [25]. Powder size distribution will need to be tightly controlled once the laser parameters are selected to ensure high part densities.

2.3 Evaluation of Fine and Coarser Particle Size Distributions

During the laser powder bed fusion process with the EOS M270, the EOS default 17-4 stainless steel laser parameters were initially used to produce 4340 steel samples (-325Mesh, -44 μm) 4340 powder (Table 2.1). It was initially thought that the finer powder would pack adequately [26]. During the experiment, the flow of the powder may have suffered due to the agglomeration of the powder which affects recoating performance. There were signs of powder agglomeration because there were clumps of powder oriented in the horizontal direction on the recoater arm and the microstructure revealed odd shaped defects (Figure 2.2a). It was likely caused by static interaction resulting from the finer particles (Figure 2.2b and Figure 2.3).

After acquiring the larger particle size of 4340 steel (-53+22 microns, -270Mesh+22 microns) (Figure 2.4 and 2.5), the larger irregular shaped pores disappeared as a result of the elimination of the finer particles, but there was evidence of cracking (Figure 2.6 a-b). Furthermore, the process parameters produced some porosity in the 4340 steel sample because adequate laser energy was not applied.

The finer particles pose a safety risk as well because they become momentarily airborne after agitation such as pouring. During pouring, ignition may occur and there is also a higher risk of inhalation of powders. Despite using powders with a larger particle size, pores and cracking remained; this may indicate that the defects are likely the result of parameter selection as opposed to powder size.

Table 2.1 EOS 17-4 Default Stainless Steel Parameters Applied to 4340 Steel Powder

Sample ID	**Scan speed** mm/sec	**Power** watts	**Hatch distance** mm	**Energy Density** J/mm^3
4340	1000	195	0.10	97.5

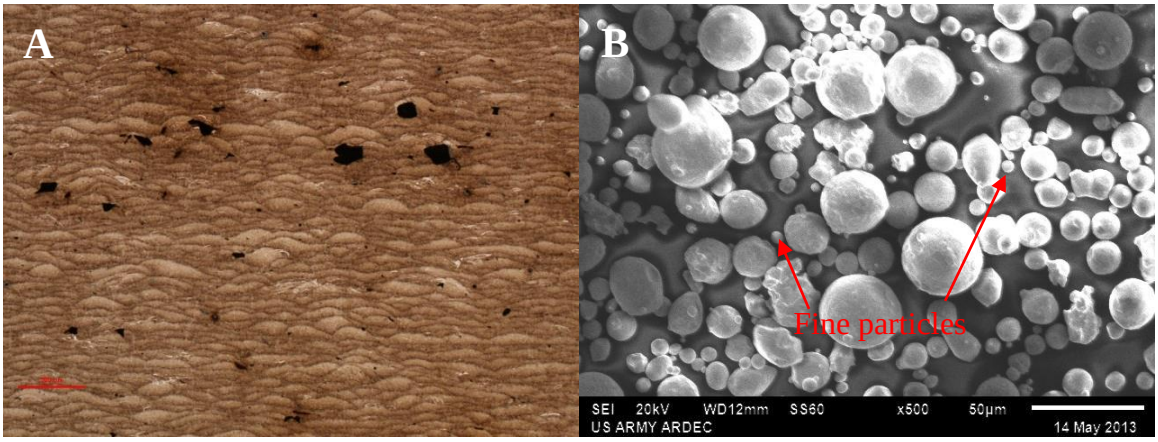

Figure 2.2 (A) Microstructure of DMLS 4340 steel powder (-44 micron) using EOS 17-4 stainless steel laser parameters from Table 2.1. Scale bar in figure (A) represents 200 microns. (B) SEM image of 4340 steel (-325Mesh, -44micron) powder.

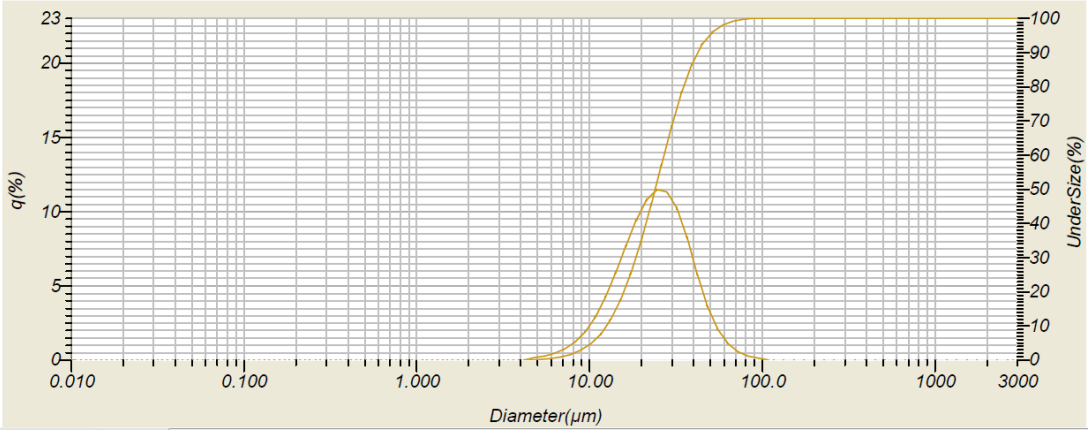

Figure 2.3 Laser diffraction of 4340 steel powder -44 micron particle size.

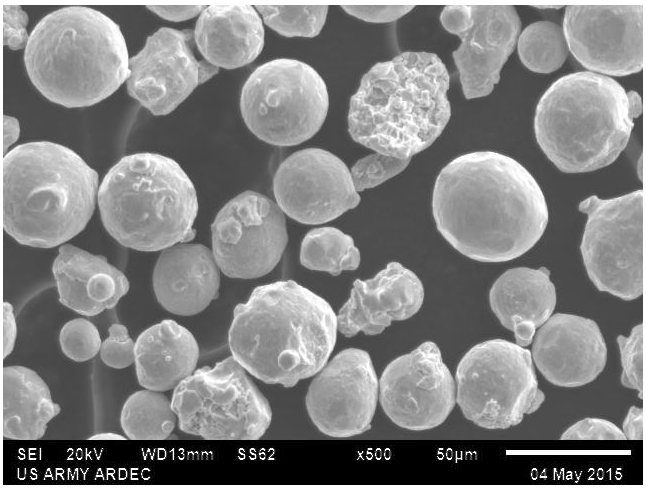

Figure 2.4 SEM image of -53+22 micron 4340 steel powder.

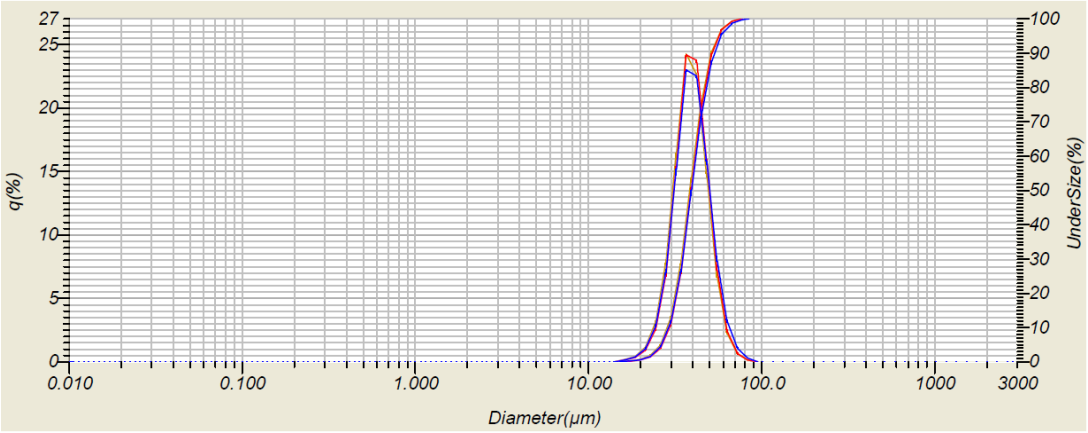

Figure 2.5 Laser diffraction of 4340 steel powder 22-53 micron coarser particle size.

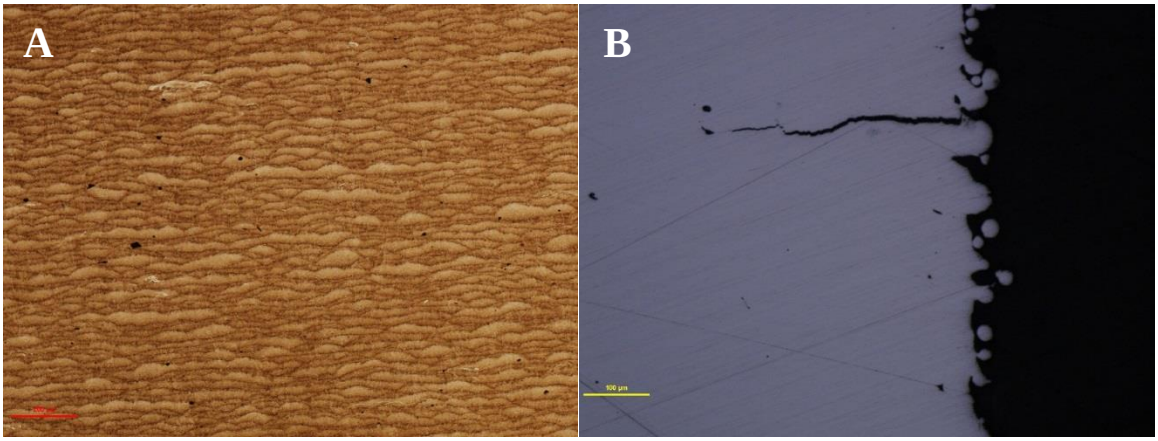

Figure 2.6 Etched (A) and unetched (B) microstructures of DMLS 4340 steel powder (-53+22 micron) using EOS 17-4 stainless steel parameters from Table 2.1. The scale bar represents 200 microns for (A) and 100 microns for (B).

2.4 Recoating Experiment

Particles less than 10 microns were removed in the next set of experiments (-44+10μm). The static interaction of the particles was reduced because the horizontal agglomerates disappeared and the powder flowed more freely. However, the powder feed rate was higher for the manufacture of 4340 and 4140 tensile bars as compared to the nominal feed rate for stainless steel part coverage provided by EOS. Powder size or material interaction was responsible for the difference in powder coverage.

Three 4340 steel powder sizes (-44 μm +16 μm, -44 μm +22 μm, -53 μm +22 μm) were evaluated to determine if the amount of powder needed to feed part 1 in Figure 2.7 would reduce as the particle size increases while keeping the recoating speed the same [27]. The laser parameters were narrowed down as well. The parameters 1-40 indicated in Appendices A.1-A.3 in the image were used to determine if the powder packing was similar with each powder type according to microstructural evaluation [27]. The parts were arranged on the plate as follows in Figure 2.7. The powder is verified to be gas atomized because the powder particles are mostly spherical as can be seen in Figure 2.8. Gas atomized powder is preferable because the spherical particles produce high packing and there is minimal interaction between powder particles (frictional forces) [25]. The resulting microstructures, produced by the process, in this parameter range, has fine grains in the micron size range (Figure 2.9). The powder particles do not appear to pack significantly different between the three size distributions because the resulting porosity is minimal for optimal parameters (Figure 2.10) [27]. The pores are minimal and round in shape. Furthermore, the porosity increases when the parameters are not optimal (Figure 2.11). As a result, the powder size distribution is in a tight range, and appears to be optimized. After

the recoating parameters were determined for the -325Mesh+22micron at 80mm/sec, the recoating speed was increased to determine whether recoating could be improved. First, the recoating speed was increased to 250mm/sec [27]. The feed ratio decreased to 3.42 for full build plate coverage. When the recoating speed was reduced to 50mm/sec, part 1 was not fully covered with powder. As a result, there is a significant interaction of the powder with the recoater blade and sintered part during the build. There is no major difference in powder packing with the three sizes of powder.

There were minor variances in the recoating performance of the powder because the feed ratio was between 3.83 and 4.17 at recoater speed of 80mm/sec (Table 2.2). A higher quantity of powder was needed to cover part 1 in Figure 2.7 because the component has a higher cross section. Furthermore, the 4340 powder with lower apparent density and highest flow rate required the most powder for full coverage. The large differences in feed ratio between stainless steel and 4340 (-270Mesh+22microns), at similar size, is likely due to differences in the magnetic properties of the 4340 steel powder [27].

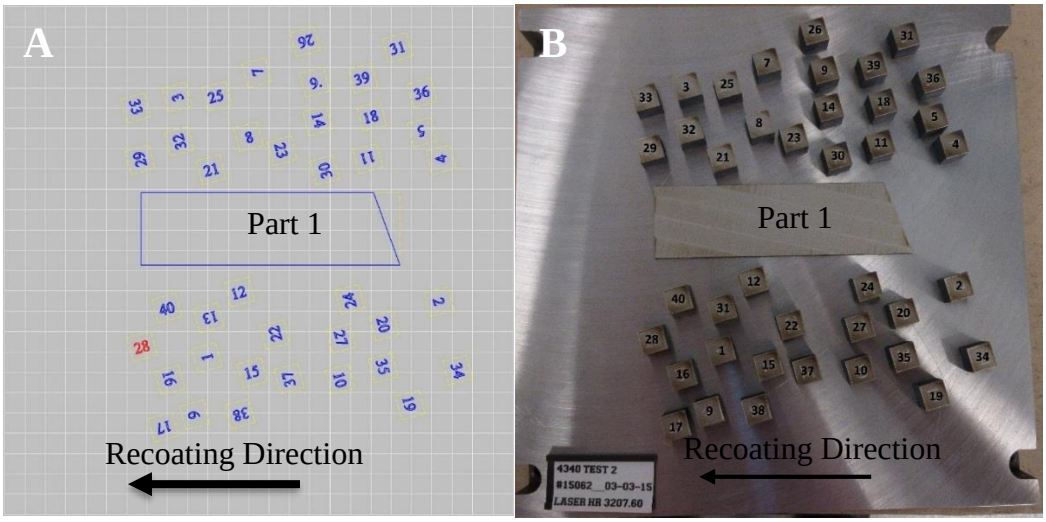

Figure 2.7 Schematic (A) and picture (B) of a build on the plate of the horizontal section of the location of the part, recoating direction and the location of 40 metallurgical cubes. *Source:* [27].

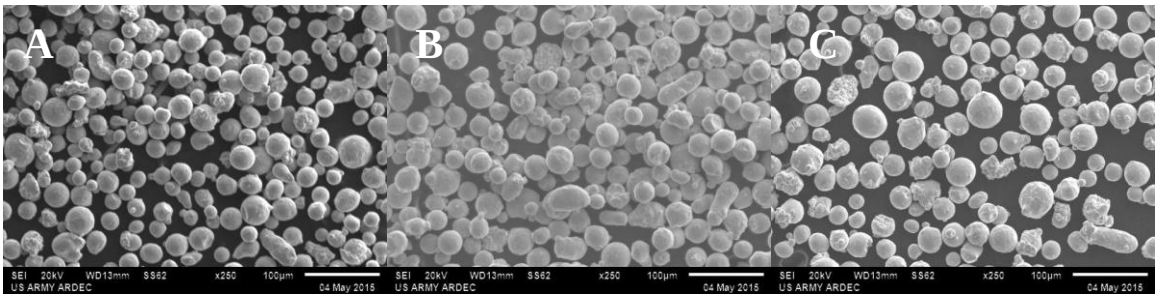

Figure 2.8 250x magnification SEM photos of 4340 steel powder: (A)-325Mesh+16μm, (B)-325Mesh+22μm and (C)-270Mesh+22μm. The scale bar text in Figures 2a-c reads 100μm.
Source: [27].

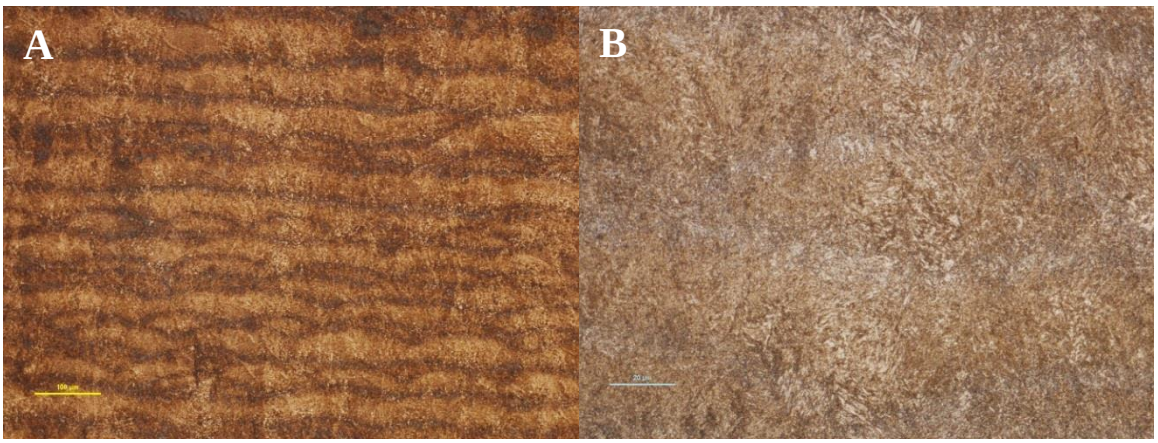

Figure 2.9 100x and 500x of a representative structure of DMLS. The scale bar text in (A) represents 100μm and the scale bar in (B) represents 20 μm.
Source: [27].

Figure 2.10 50x unetched image of the microstructure of the powder (A) -325Mesh+16μm, (B) -325Mesh+22μm, and (C) -270Mesh+22μm at 185W and 725mm/sec. The scale bar represents 200 μm.
Source: [27].

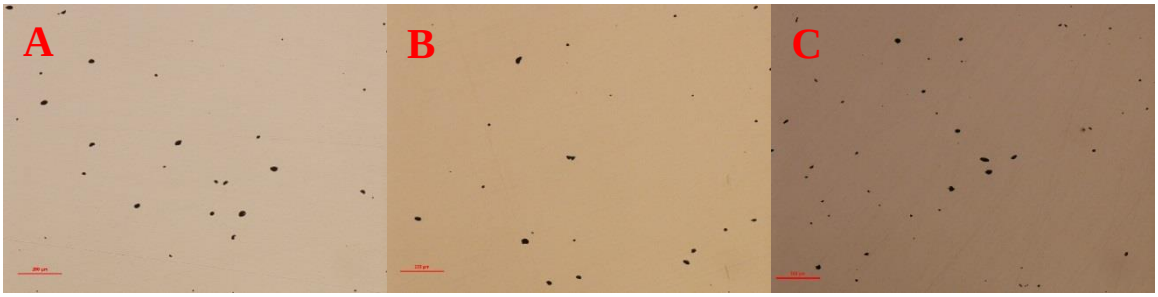

Figure 2.11 50x unetched image of the microstructure of the powder (A) -325Mesh+16μm, (B) -325Mesh+22μm, and (C) -270Mesh+22μm at 185W and 450mm/sec. The scale bar represents 200 μm.
Source: [27].

Table 2.2 Summary of Particle Size, Apparent Density, Flow Rate, and Feed Ratio at 80mm/sec Recoating Speed. EOS Stainless Steel Powder and the Three Different Sizes of 4340 Steel were Analyzed

Powder specification	**D10** μm	**D50** μm	**D90** μm	**Apparent density** g/cm^3	**Flow rate** g/sec	**Feed ratio**
GP1 Stainless steel	27.1	38.4	52.0	4.22	3.47	3.00*
-325Mesh+16μm	23.9	33.5	46.3	4.03	3.26	3.83
-325Mesh+22μm	27.6	37.2	50.6	3.96	3.55	4.17
-270Mesh+22μm	29.5	39.2	51.9	3.98	3.43	4.00

*Feed ratio is based on nominal EOS recoater feed ratio for 17-4 stainless steel
Source: [27].

2.5 Chemical and Morphological Analysis of Powder and Parts

The oxygen combustion and energy dispersive spectroscopy analyses also confirm that the virgin powder is produced by a gas atomization process due to the low oxygen content and spherical morphology (Figure 2.12 and Table 2.3). As the powder is reused, the oxygen concentration increases (Table 2.3). This is partly a result of unsintered powder which melts or vaporizes when exposed to heat in the chamber, combining with other unsintered powder (Figure 2.13). The fan removes the majority of the particles to the recirculating

system. Since the condensate contains larger oxygenated particles, the laser may not have enough energy to fully melt the larger particles to create a fully dense melt pool. Poor recoater performance may result from improper spreading as indicated by (Figure 2.13) [28]. Thus, it is important to sieve the larger particles out after each build. The oxides are likely to be forming during ejection of the particles according to a study of Al10SiMg and 316L stainless. These materials show the presence of oxides resulting from the reactions with Si and Mn, respectively.

In addition, there are also oxygenated particles which cannot be sieved out because they are of an intermediate size (Figure 2.14). Furthermore, there are no significant oxide inclusions in the sample according to oxygen and microstructure analyses of 4340 steel (Table 2.3).

Table 2.3 Oxygen Combustion Analyses of Powder and Part

Sample type	**Oxygen content** wt%
4340 (-44 +10 μm) virgin	.035
4340 (-44 + 10 μm) used sieved with 80 micron	.045
DMLS 4340 part	.008

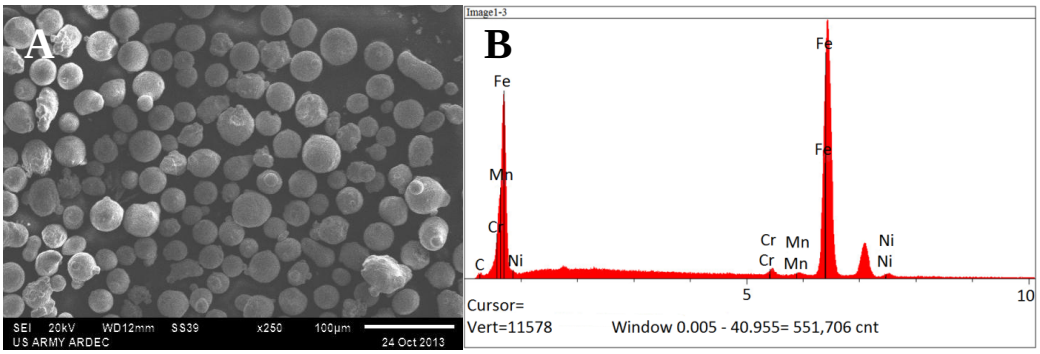

Figure 2.12 Image of virgin powder (A) and EDS spectrum (B) of the oversized oxygenated particle.
Source: [2].

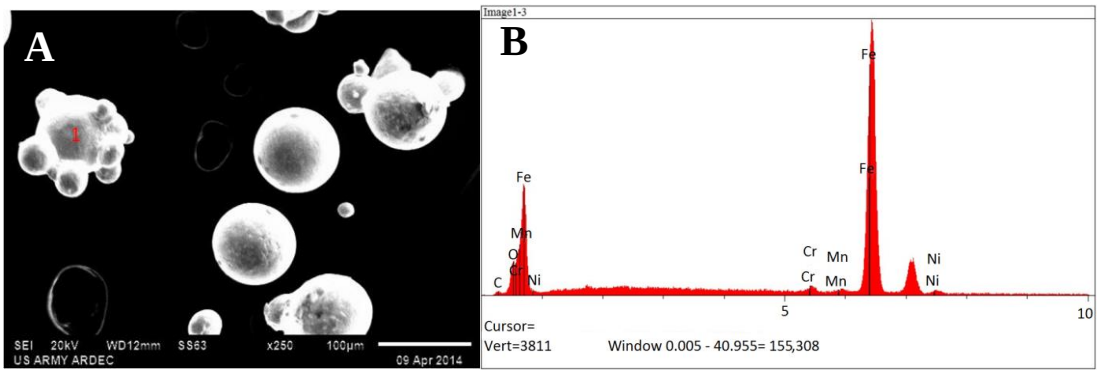

Figure 2.13 Image of the recycled powder (A) and EDS spectrum (B) of the oversized oxygenated particle.
Source: [2].

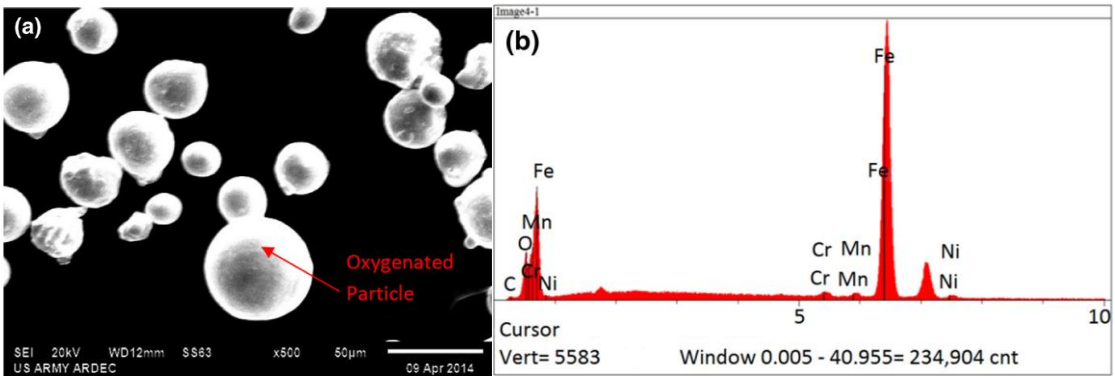

Figure 2.14 Image of the recycled powder (A) and EDS spectrum of the oxygenated particle in the powder after using a 80 micron sieve (B).
Source: [2].

2.6 Conclusion

The powder selection is an important step because adequate packing and flow is required to fabricate effective parts. After the finer particles (<10microns) were removed from 44 micron powder, adequate flow was obtained. However, there was high particle and recoater interaction which required much more powder to feed larger cross section in comparison to 17-4 stainless steel. Therefore, three slightly larger particle sizes in the range of 16-53 microns were investigated to determine feed rate, but feed rate required did not change significantly. As a result, the magnetic properties of 4340 affected the recoating

performance. The process also produced splatter which needs to be removed by the recirculating fan and sieved out before reuse.

CHAPTER 3

OVERALL MICROSTRUCTURE ANALYSIS

3.1 Description of Microstructure Analyses Performed

Generic microstructural characteristics for the low alloy steel was analyzed in the as built condition. Microstructure and phase analysis were also analyzed as a function of material condition in the horizontal (x-y) and (z) vertical orientations.

3.2 General Microstructure of 4340 and 4140 using Laser Powder Bed Fusion

The predicted structure of 4340 DMLS manufactured samples based on the phase diagram is martensitic due to rapid cooling which is indicated by the TTT (Time-Temperature-Transformation) curve in Figure 3.1. Nickel is in solid solution with the iron and it stabilizes the austenite phase [29]. Thus, it allows for a slower cooling rate to form martensite.

According to the previous literature, the top of the build surface was martensitic microstructure due to rapid cooling of steel [30] [31]. As the layers are built on top of the martensitic layer, there is heating which likely converts some of the original martensite into different phases according to a study on plain carbon steel [30].

This is confirmed by the top image of the 4340 microstructure because it appears to be a predominantly martensitic structure (Figure 3.2). The hardness is in the range of 654-725HV HRC (58-61HRC) and is also indicative of high martensite content. The hardness decreases from the top surface because the subsequent layers heat up the martensite and converts some of it to other phases (Figure 3.3). Thus, the hardness

decreases to 387-523HV (40-51 HRC) within the substrate. The microstructure has fine band which consist of sub-grains because of the rapid cooling. It is likely caused by the scan stripe strategy because similar bands were observed on Inconel 625 produced on the EOS M270. The melt overlap and directional heating likely promotes growth of the bands [32].

The second material evaluated is 4140 steel. The TTT (Time-Temperature-Transformation) diagram of 4140 is shifted towards the left in comparison to 4340 (Figure 3.4). Thus, it has a lower hardenability than 4340 due to a decrease in nickel (Table 3.1) content. The microstructure of 4140 steel produced by this process is similar to 4340 steel (Figure 3.5).

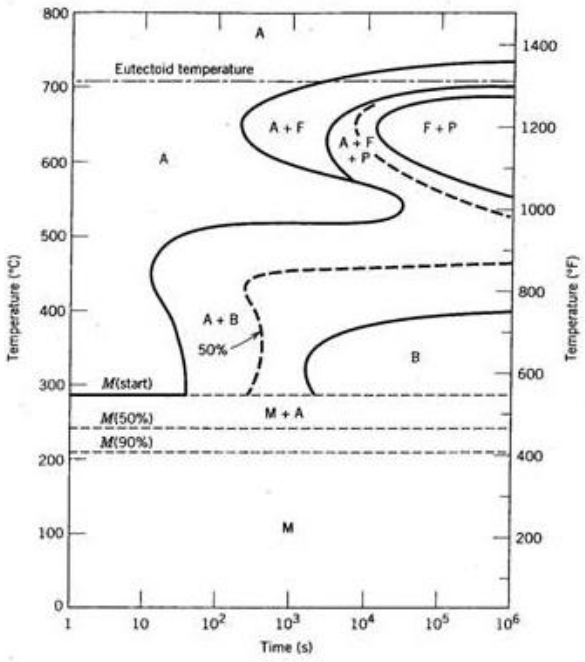

Figure 3.1 TTT diagram for 4340 steel.
Source: [33].

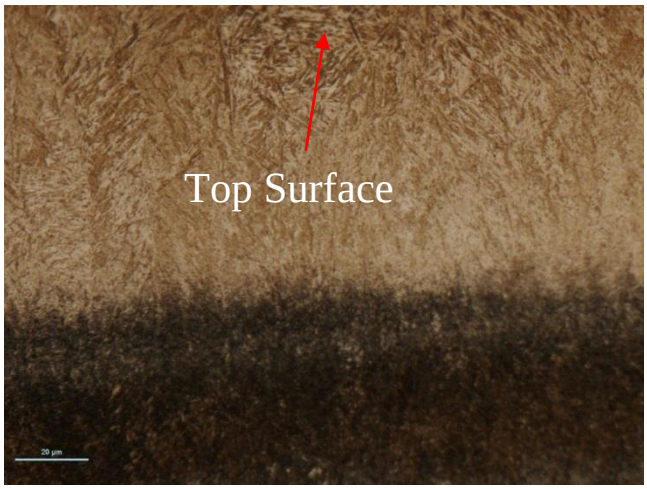

Figure 3.2 DMLS 4340 sample of the top surface. The scale bar represents 20 microns.

Figure 3.3 DMLS 4340 sample of the substrate. The scale bar represents 10 microns.

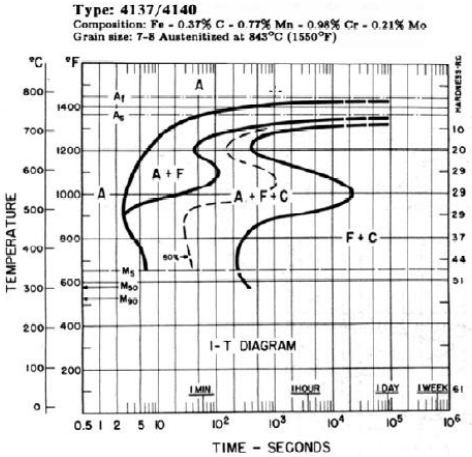

Figure 3.4 TTT diagram for 4140 steel.
Source: [34].

Figure 3.5 DMLS 4140 steel. The scale bar represents 20 microns.

Table 3.1 Chemical Composition of 4340 and 4140 Steel

Element	**AISI 4340** wt%	**AISI 4140** wt%
Fe	Balance	Balance
C	0.37-0.43	0.38-0.43
Mn	0.60-0.80	0.75-1.00
Ni	1.65-2.00	--
Cr	0.70-0.90	0.80-1.10
Mo	0.20-0.30	0.15-0.25
Si	0.15-0.30	0.15-0.30
S	0.04	0.04
P	0.03	0.04

3.3 Previous Fracture Toughness Evaluation

The build platform temperature is near 80^{o}C (176^{o}F). 4340 at similar yield strength (160-180ksi) has a significantly higher crack arrest toughness at 165 ^{o}F than 4140 [35]. It may indicate that 4340 is a more resilient material than 4140 at temperatures near the build platform temperature.

3.4 Heat Treatment Evaluation of 4340 Microstructure

Based on the microstructure evaluation of metallurgical cubes, there are some differences in the microstructure in the longitudinal and transverse direction. Additionally, the parts also have a small concentration of austenite which is removed by stress relief according to XRD (X-ray Diffraction) results (Figure 3.6). The as sintered specimen has heat zone lines (Figure 3.7). However, melt pool line remnants are apparent (Figure 3.8). The hardness does not vary significantly as a function of orientation (Figures 3.7 and 3.8). After normalizing, the melt pool boundaries disappear and produce a coarse grained structure (Figure 3.9). The structure in the longitudinal and transverse directions appear to be more homogenous. Thus, the samples need to be normalized to produce more isotropic parts. The normalizing process introduces small concentration of austenite according to XRD results. Next, the part is austenitized at 1500^{o}F and quenched in oil. Then, the part is tempered at 375^{o}F for two hours. The quench and temper eliminates the retained austenite from normalizing the part (Figure 3.10). The structures in both directions are more uniform. The direction of heat flow is influencing the structure.

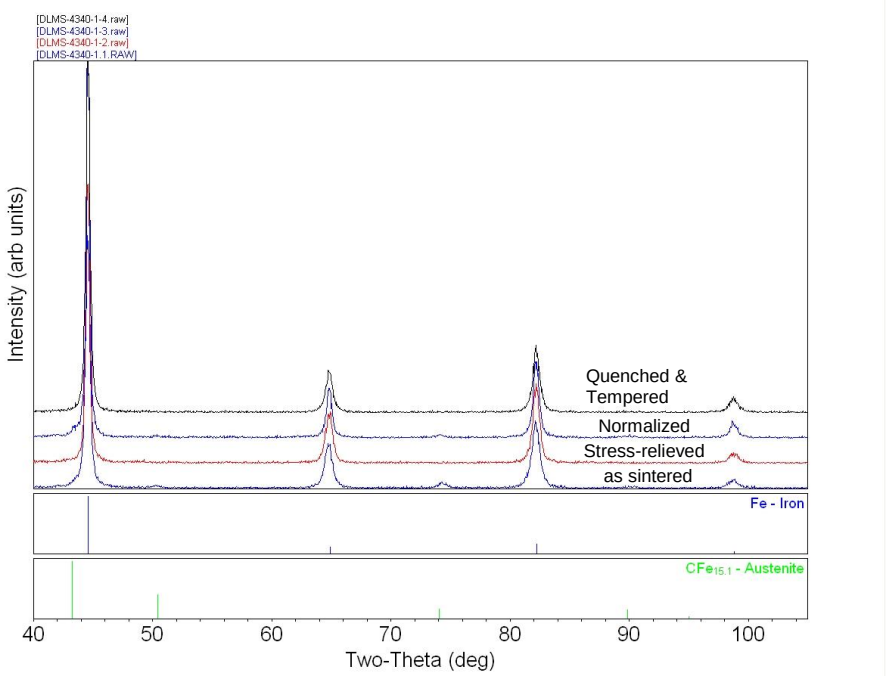

Figure 3.6 XRD analysis of as sintering, stress relieved, normalized, quench and tempered.

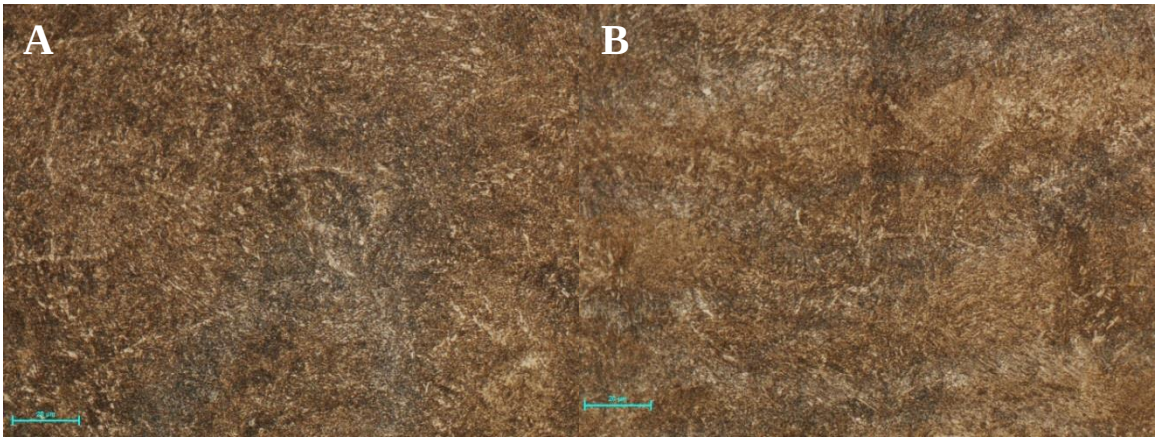

Figure 3.7 500x micrographs of as-sintered condition in the transverse (A) and longitudinal direction (B). The scale bar represents 20 microns. The hardness was between 47-50 HRC for both orientations.

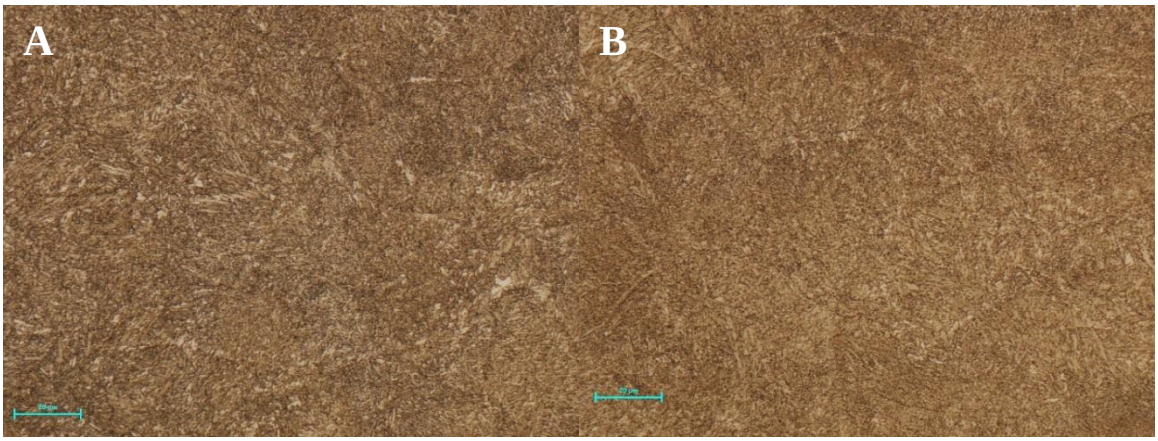

Figure 3.8 500x micrographs of stress relieved condition in the transverse (A) and longitudinal direction (B). The scale bar represents 20 microns. The hardness was between 41-44 HRC for both orientations.

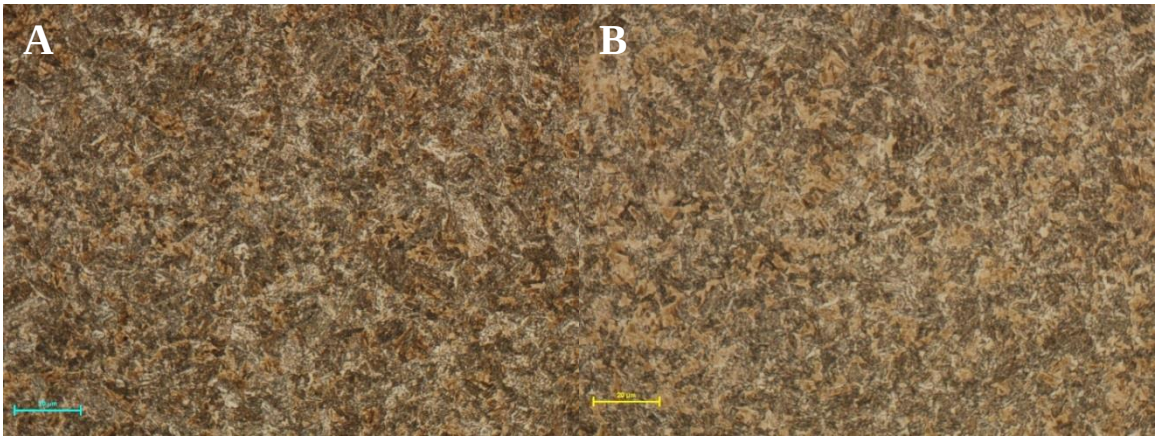

Figure 3.9 500x micrographs in normalized at 1650^{o}F in the transverse (A) and longitudinal direction (B). The scale bar represents 20 microns. The hardness was between 39-44 HRC for both orientations.

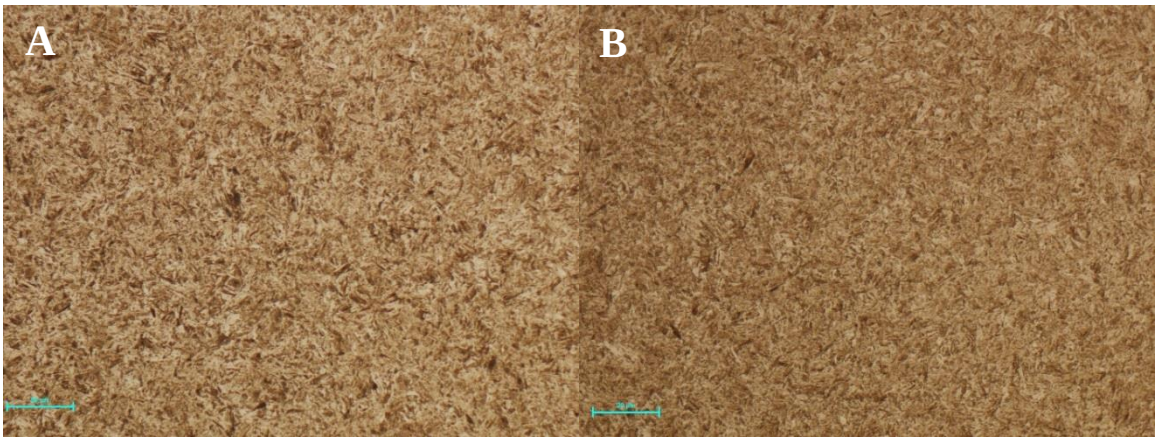

Figure 3.10 500x micrographs normalized, austenitized, quench and tempered in the transverse (A) and longitudinal direction (B). The scale bar represents 20 microns. The hardness was between 55-57 HRC for both orientations.

3.5 Conclusion

4340 steel and 4140 steel were evaluated. The structure of the low alloy steels begins as predominantly martensitic due to rapid cooling. The rapid cooling produces a fine substructure with bands. The structure transforms to a mixed (tempered) structure after subsequent layers are added. A similar structure was observed for 4140. The structure becomes more isotropic after heat treatment of 4340.

CHAPTER 4

MECHANICAL AND MICROSTRUCTURAL EVALUATION OF LASER PROCESS PARAMETERS

4.1 Brief Description of Process Parameter Development

Laser parameter development is required to identify parameters for dense structures of low alloy steel. Microstructural analyses of specimens processed under various laser parameters were performed. By verification of the mechanical performance, we were able to establish energy density to produce mechanically sound components. The parameters were further optimized to establish an effective parameter set for repeatability studies.

4.2 Porosity and Initial Parameter Selection - Literature Review

Porosity is controlled by the process parameters. A study performed on 316L stainless steel provides some valuable insight into the formation of pores in the structure [36]. If the energy density is adequate, then the melt pool will be continuous and the part will achieve a high density. At high part density, random pores may be attributed to trapped gasses in the powder bed. If the energy density is decreased significantly (i.e. increasing laser scan speed or decreasing laser power), the porosity increases according to a study performed on 316L stainless. If hatch distance is too high, the melt pool overlap is not adequate which would lead to porosity. If the laser scan speed is too high while other parameters remain the same, then the melt pools become unstable and are not continuous. The main reason they become unstable is the area of interaction between the melt pool and the underlying substrate is small. As a result, it leads to unfavorable wetting and balling

[21]. If the applied energy density is too high, it may lead to the keyhole effect which produces porosity [37].

4.3 Selection of Parameters

Metallurgical cubes were widely used in these experiments because they reveal the recoating performance and the layer by layer interaction of the laser with the powder bed. When 10-44 micron powder was used, the process parameters were varied significantly from 400-1500mm/sec, 120-195Watts, and 0.1mm hatch distance (Table B.1 in Appendix B). These parameters were evaluated to select and identify the process variables [38]. During the build, the parameters corresponding to high energy density (>180 J/mm^3) were not used due to the build-up of thermal stresses in the specimens. These high thermal stresses cause the lifting of the corners of the cubes. At high energy density, it indicates that the melt pool instability caused slight porosity (Table 4.1; Figure 4.1a). When the energy density was reduced slightly, there was evidence of cracking between layers with moderate porosity and slightly higher hardness (Table 4.1; Figure 4.1b) [38]. When the applied energy was significantly reduced, the melt pool lines were likely to be too thin for adequate melt pool overlap. It may have also been caused by balling due to unfavorable wetting. (Table 4.1; Figure 4.2-a-b) [21].

The parameters which produced samples with minimal porosity are outlined in Table 4.1 [sample B]. This is the evidence of adequate melt pool overlap [39]. The corresponding microstructure is shown in Figure 4.3 a-b. Tensile testing was used to verify whether parameter B was acceptable in the next section.

Table 4.1 Microstructure Analysis of Parameter Sets A-E [38]

Sample ID	**Scan Speed** mm/sec	**Power** Watts	**Hatch distance** mm	**Energy Density** J/ mm^3	**Microhardness** HV
A	500	170	0.10	170	434.6
B	600	170	0.10	142	425.2
C	900	170	0.10	94.4	471.8
D	1200	170	0.10	71	467.4
E	1500	170	0.10	57	497

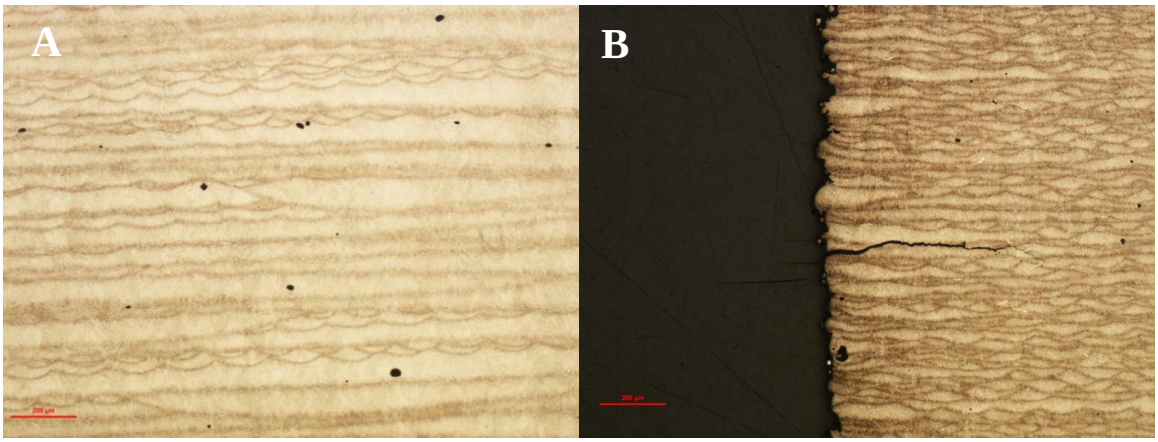

Figure 4.1 50x micrograph of etched longitudinal section of 4340 using Table 4.1 sample A (A) and C (B). The scale bar represents 200 microns.
Source: [38].

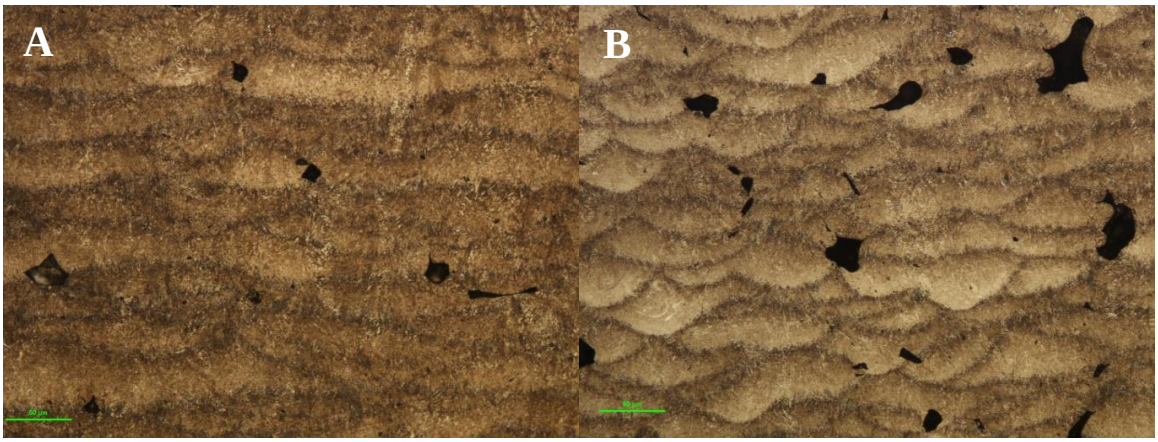

Figure 4.2 200x micrographs of etched longitudinal cross section of low alloy steel using (A) Table 4.1 sample C (B) sample D. The scale bar represents 50 microns.
Source: [38].

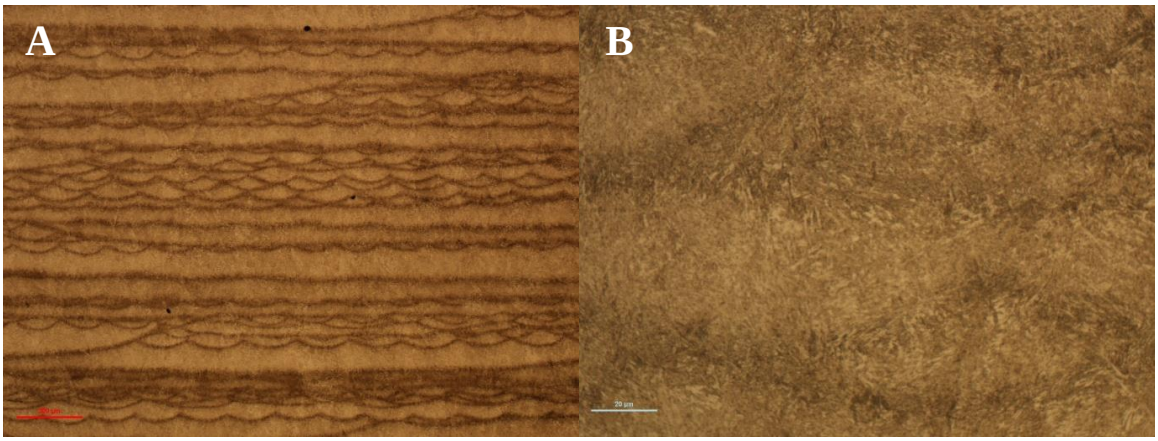

Figure 4.3 50x micrograph for sample B Table 4.1 (A) and 500x sample B (B). The scale bar represents 200 microns for (A) and 20 microns for (B).
Source: [38].

4.4 Literature Review - Tensile Geometry

Tensile properties are slightly anisotropic for DMLS produced parts [40]. Another issue with the process is that different facilities test tensile specimens with different geometries. Flat specimens, whether machined or not, have higher variation in tensile properties than cylindrical specimens. In addition, unmachined specimens have higher variation than machined specimens [41]. In this study, cylindrical tensile specimens were machined in accordance with ASTM E8 in order to have more consistent results [42]. A major downside is that it takes a long time to build large specimens (minimum 4" long with a reduced section of .25"). The total cost, when multiplied by numerous test facilities, is tremendous to build and test the mechanical properties for a particular material to generate statistically significant data.

4.5 Initial Tensile Testing

Mechanical properties were generated for 4340 steel material samples that were produced with parameters that yielded low porosity [38]. These parameters were chosen to

determine if the energy density range was appropriate for the process. The parts were stress relieved at 1100 ^{o}F for 1 hour for this study to prevent warping. The parameter B from Table 4.1 was chosen. The sample had significant ductility because there was significant necking strain according to the stress strain curve (Figure 4.4). The yield strength and the ductility matched 4340 steel according to ASM international Standards (Table 4.2 and Figure 4.4). The parts were initially built in the x-y orientation [2].

Table 4.2 DMLS Stress Relieved using Parameter B from Table 4.1

Material Condition	**Modulus** ksi	**Yield Strength** ksi	**Tensile Strength** ksi	**Elongation** %
Typical Wrought 4340 properties from ASM international	29,000	183	199	15
Run A: DMLS of Virgin Powder	31,000	189-190	199	16-17
Run B: DMLS after once recycled powder.	31,000	187-190	198	16-17

Source: [2].

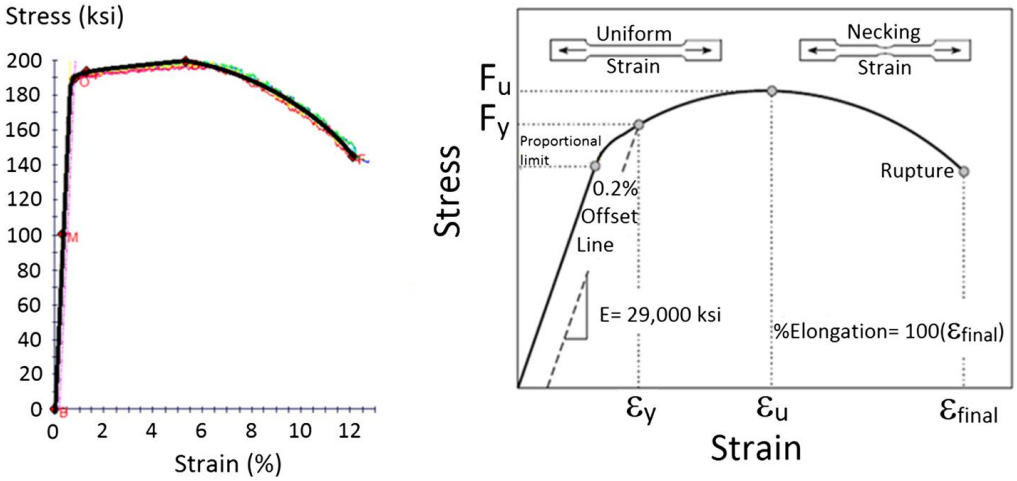

Figure 4.4 Stress strain curve in the stress relieved condition from Table 4.2.
Source: [2].

4.6 Mechanical and Microstructural Evaluation at Optimal Applied Energy Range

The hatch distance, power, and speed were changed to maintain the energy density between 113-163 J/mm^3. All the cubes had a density greater than 99 percent of its theoretical density according to Archimedes density measurements (assuming the density of wrought 4340 is 7.85g/cm^3 [43]. The hardness and density did not vary significantly with these samples (Table B.2 in Appendix B). However, there was some cracking in several of the cubes in the x-y direction which may have been caused by gas flow issues. The gas flow tube was disconnected. The tube assists in controlling the air flow. It may have been an indication of variability of air flow which may have led to cracking of the samples on the left side of the build chamber. Several cubes on the left side of the chamber were darker after laser exposure which likely indicates air flow issues. Mechanical testing was needed to provide further insight into the parameters that provided good tensile properties. All the samples were heat treated afterwards. The samples were stress relieved at 1100 ^{o}F**,** normalized at 1650 ^{o}F for one hour, passively cooled to room temperature, heated to 1500 ^{o}F for one hour, quenched in oil and finally tempered at 375^{o}F for two hours. All ten tensile bars were then machined to 3/8" diameter with a reduced section of 1/4" diameter specimen in accordance with ASTM E8.

One of the objectives in this study was to build successful Z oriented tensile specimens. A relatively low energy density was chosen to fabricate the tensile specimens (~125 J/mm^3) to ensure that they would build successfully. Two parameter sets were chosen in which the hatch distance and laser scan speed were balanced in order to achieve a similar applied energy density (Table 4.3). The tensile bars built smoothly because there was very little sound when the recoater passed over the parts during the application of the

powder layer. It shows that there was minimal interaction with the recoater which indicates that these parameters produce relatively low thermal stress. All the tensile bars exhibited ductile behavior which was indicated by the necking and the engineering stress-strain curves (necking strain) (Figures 4.5-4.6). The modulus of elasticity, yield strength and tensile strength were similar for both samples. Sample **A** showed evidence of cracking near the fracture surface (Figure 4.7). These values are comparable to wrought. However, the elongation values for sample **A** are slightly lower than that of sample **B** (Table 4.4). Both are significantly lower than wrought. The microstructures in the as sintered condition are different in part because the heat affected region for laser parameter set **B** is generally larger than **A** according to Figure 4.8 a-b. Thus, it may indicate that the laser did not penetrate as deep into sample **A** as sample **B**.

Table 4.3 Laser Parameters for Tensile Build for Samples **A** and **B**

Sample ID	**Scan Speed** mm/sec	**Power** Watts	**Hatch distance** mm	**Applied Energy Density** J/mm^3
A	1050	185	0.07	125.9
B	625	185	0.12	123.3

Table 4.4 Tensile Data from Samples **A** and **B** from Table 4.3 Heat Treated to 51 Rockwell C

Material Condition	**Elastic Modulus** ksi	**Yield Strength** ksi	**Tensile Strength** ksi	**Elongation** %
Wrought	29,000	220	270	11
A	29,800	226-234	293-299	6.0-7.6
B	29,500	226-231	293-296	7.1-10.3

Figure 4.5 Photograph showing evidence of necking which is indicative of ductile failure.

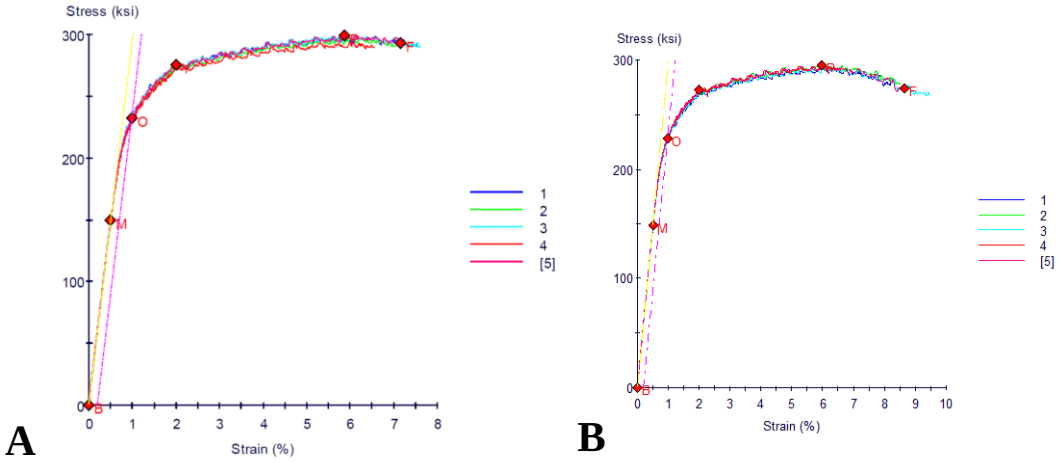

A **B**

Figure 4.6 Engineering stress-strain curves from Table 4.4 sample A (A) and sample B (B), respectively.

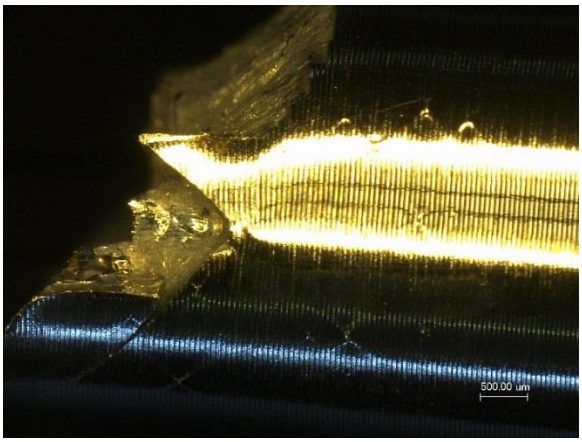

Figure 4.7 Overall image of fracture surface from sample **A** from Table 4.3.

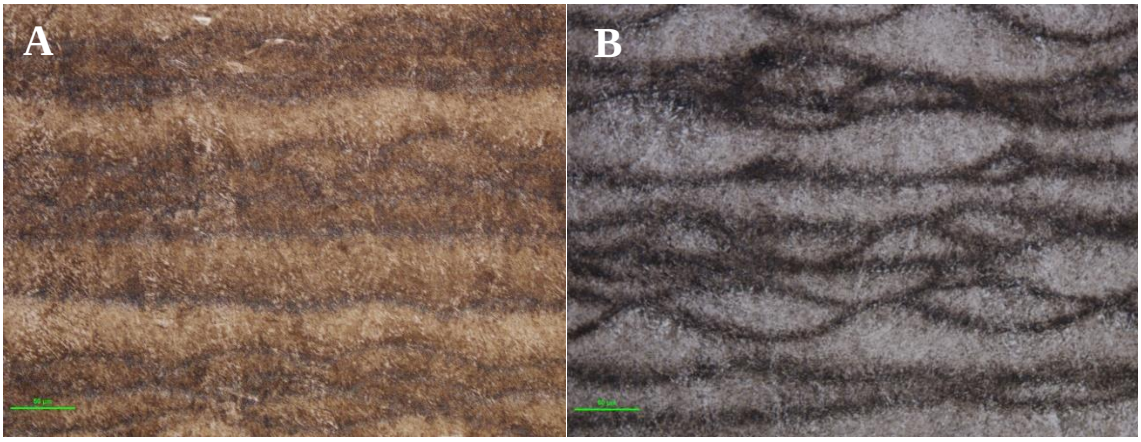

Figure 4.8 200x as-sintered etched micrographs from the laser parameters used in sample **A** (A) and sample **B** (B), respectively. The scale bar represents 50 microns.

Afterwards, the energy density was increased to 134.1 J/mm^3 by decreasing the laser scan speed for sample **B** to 575mm/sec (Table 4.5). The mechanical properties are similar to samples **A** and **B** specimens except the elongation is significantly higher as shown in Table 4.6. The elongation increases to 9-11 wt% in the z direction (Figure 4.9). In the x-y orientation, the elongation is 10- 12 wt% (Figure 4.9). Thus, *the increase in the laser dwell time led to an improvement in the mechanical performance of the specimen*. The maximum heat affected region in the as sintered condition are comparable to sample **B** (Figure 4.10). The improvement may have resulted from a stronger interlayer bonding due to slightly higher absorption of laser energy. The top layer thickness was then evaluated in the next section to further understand laser absorption mechanisms to provide insight into interlayer bonding with respect to applied energy density.

Table 4.5 Laser Parameters for Sample **C**

Sample ID	**Scan Speed** mm/sec	**Power** Watts	**Hatch distance** mm	**Applied Energy Density** J/mm^3
C	575	185	0.12	134.1

Table 4.6 Tensile Data from Sample **C** Heat Treated to 51 HRC

Material Condition	**Elastic Modulus** ksi	**Yield Strength** ksi	**Tensile Strength** ksi	**Elongation** %
Wrought	29,000	220	270	11
Z	29,300	226-234	288-290	9-11
X-Y	29,300	229-233	293-295	10-12

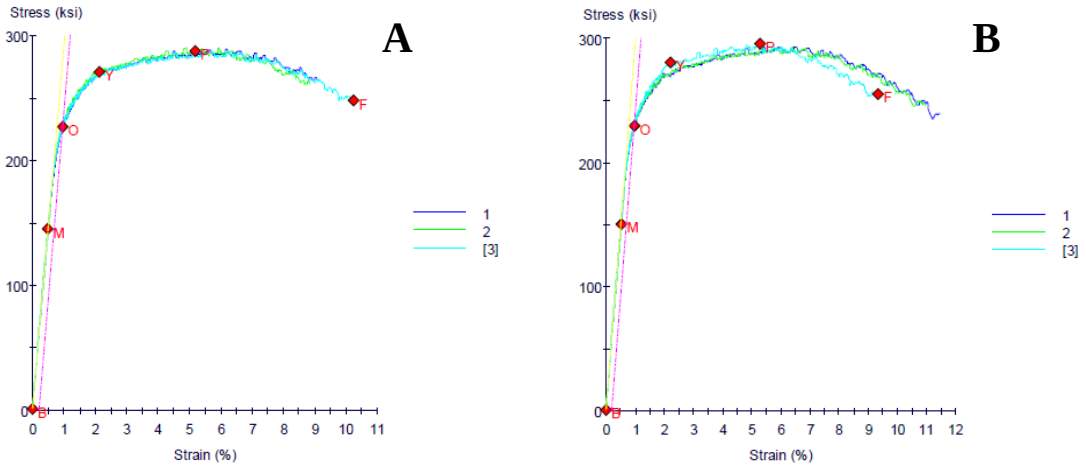

Figure 4.9 Engineering stress-strain from sample **C** in the z orientation (A) and x-y (B), respectively.

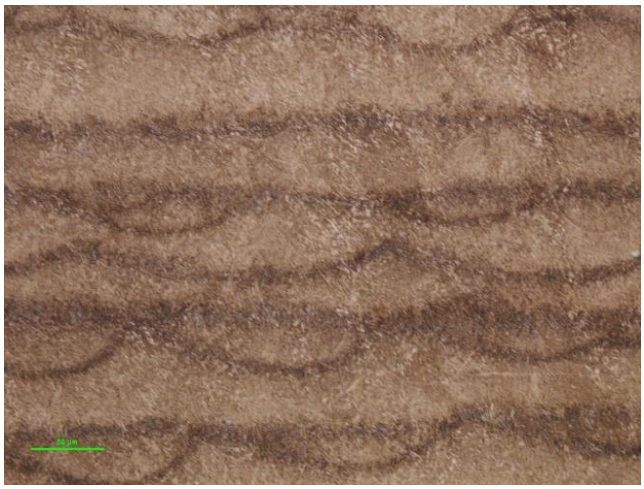

Figure 4.10 200x as sintered microstructure etched micrograph using parameters from Table 4.5 sample **C**. The scale bar represents 50 microns.

4.6.1 Laser Absorption Study

Laser absorption is critical because the powder has higher absorption rate than the substrate due to the higher cumulative surface area of the powder in comparison to the solidified section. It is extremely important to have the proper hatch distance so that there is adequate overlap with the melt pool while having high effective absorption of the laser beam by the powder bed. The maximum martensite layer thickness (12 measurements) is evaluated at 195, 150, and 100 watts with the hatch distance between 0.08 and 0.14mm. The maximum values were taken because there were variances in the layer thickness. The energy density was between (125-145 J/mm^3). When the applied energy density, power, and layer thickness are the same, the absorption of laser energy is different because the initial martensite layer thickness is significantly higher as the speed is decreased after the same energy density is applied (Table 4.7). Thus, the speed of the laser has a major influence on the absorption. When the hatch distance is increased from 0.08mm to 0.10 mm at the same applied energy density, the average martensite layer is significantly thicker than 0.08 mm hatch distance at the same energy density levels for the three different laser powers. At the

same energy density, the higher power generally has a thicker layer than the lower power constituents. Thus, the power and speed have the strongest influence on laser absorption. Furthermore, it shows that the energy density equation is not valid because the martensite layer thickness varies significantly when only hatch distance and speed are changed at the same energy density level. There is a limitation in which speed can be decreased because it will lead to an increase in melt pool instability. Thus, the maximum martensite top layer thickness provides some qualitative insight into the absorption of laser energy. Furthermore, there was a study on 17-4 stainless steel where the laser power and speed were changed to maintain the same energy density [1]. At lower power, the part density reduced significantly because of the reduction in laser penetration. There are other methods to provide insight into the process such as single melt pool analysis which may provide an initial baseline for power and speed needed to make a continuous melt pool with appropriate penetration. For instance, a study on Ti-6Al-4V shows that generally the melt pool depth increases as the laser power is increased and speed is decreased [44]. However, there was unexpected minimal penetration at maximum applied power of 195W at two scan speeds for the EOSINT M270. It suggests that there is possible power fluctuation for the laser. An appropriate hatch distance is selected based on melt pool overlap to make test pads and low porosity samples based on the analysis of the top surface [44].

Table 4.7 Maximum Martensite Top Layer Thickness

Energy Density J/mm^3	**Power** Watts	**Hatch Distance** mm	**Scan Speed** mm/sec	**Layer Thickness** μm	**Standard Deviation** μm
125	195	.08	975	111.1	9.5
125	195	.10	780	150.5	14.0
125	195	.12	650	167.8	13.1
125	195	.14	557.1	159.3	18.8
135	195	.08	902.8	126.4	9.1
135	195	.10	722.2	152.0	16.3
135	195	.12	601.9	157.5	9.5
135	195	.14	515.9	173.1	13.6
145	195	.08	840.5	133.7	6.8
145	195	.10	672.4	164.6	12.6
145	195	.12	560.3	192.6	10.7
145	195	.14	480	220.4	19.0
125	150	.08	750	98.4	7.4
125	150	.10	600	123.8	11.0
125	150	.12	500	144.1	7.5
125	150	.14	428.6	159.7	12.1
135	150	.08	694.4	111.9	14.6
135	150	.10	555.6	134.1	15.9
135	150	.12	463	159.3	8.7
135	150	.14	396.8	178.7	9.0
145	150	.08	646.6	138.5	15.6
145	150	.10	517.2	180.9	12.1
145	150	.12	431	167.8	11.6
145	150	.14	369.5	186.2	10.2
125	100	.08	500	73.1	5.3
125	100	.10	400	89.1	6.8
125	100	.12	333.3	114.7	14.4
125	100	.14	285.7	131.2	11.3
135	100	.08	463	99.6	9.7
135	100	.10	370.4	114.6	6.1
135	100	.12	308.6	126.9	7.2
135	100	.14	264.6	127.4	4.2
145	100	.08	431	97.4	6.5
145	100	.10	344.8	103.2	11.1
145	100	.12	287.4	132.3	11.2
145	100	.14	246.3	132.4	4.4

4.7 Process Optimization

Parameters were further optimized since the previous results are comparable to wrought after heat treatment. The parameters were the centralized parameter set from Table 4.5. The microstructure was analyzed after 40 cubes, with various parameters, were built with three different powder types (in Appendix A Tables A.1-A.3). In order to ensure consistency, the specimens were built in the same location (Figure 4.11). Three parameters were selected based on microstructural analysis (Table 4.8). The applied energy density was around ~135 J/mm^3 for all three samples to determine if there would be significant differences in the interlayer bonding in a tight energy density range. The x-y tensile bars were machined from the block. Meanwhile, the reduced section of the z tensile specimens were machined from the rod. The aspect ratio of the z tensile bars was approximately 11.33 (4.25" tall/.375" diameter). The samples complied with ASTM E8. 22-53 micron powder was used.

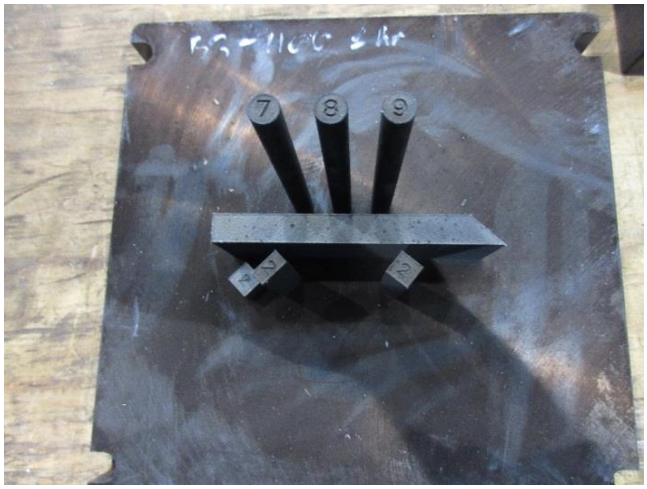

Figure 4.11 Layout of the parts.

Table 4.8 Parameter Set 4340 Steel: 20 Micron Layer and 4mm Stripe Width

Sample ID	**Power** Watts	**Hatch Distance** mm/sec	**Laser Speed** mm/sec
A	185	0.12	575
B	185	0.10	700
C	185	0.11	625

Table 4.9 Tensile Results: Parameters are Based on Table 4.8

Sample ID	**Modulus** ksi	**Yield Strength** ksi	**Tensile Strength** ksi	**Elongation** %
Typical Wrought properties	29,000	220	270	11%
A as sintered(z)	29,000	156-161	175-178	16-18
A as sintered(x-y)	29,000	185-193	201-208	19
A stress relieved(z)	29,000	154-156	166-167	16-17
A stress relieved (x-y)	30,000	177-182	188-192	16-18
A heat treated (z)	30,000*	204-217	276-277	12-15
A heat treated (x-y)	30,000*	204-207	278-279	13-14
B heat treated (z)	29,000	224-227	272-274	12-14
B heat treated (x-y)	27,000-29,000	227-229	275-277	12-14
C heat treated (z)	29,000	228-229	253-262	12-13
C heat treated (x-y)	29,000	230-231	256-264	12-14

* Only one measurement of elastic modulus was taken
Source: [45].

4.7.1 Anisotropy

The samples oriented in the x-y direction have a significantly higher yield strength, ultimate tensile, and elongation than the z orientation as can be seen in Table 4.9 and Figure 4.12. According to tensile data, there is significant anisotropy in the as sintered and stress relieved conditions. There is evidence of ductility based on the fracture surface, necking, and their respective stress strain curve (Figures 4.12-4.13). The results are fairly consistent between the sample points. After the parts were stress relieved; the tensile strength, yield strength, and elongation were slightly reduced. The tensile data showed that it was still anisotropic after stress relief. Another issue is that all the z tensile specimens broke off

center. They broke near the height where the z orientation Charpy specimens finished building (Figure 4.14a samples 19-21). For the vertically built specimens in the as built and stress relieved condition, portion of the decrease in strength is likely related to the significantly higher temperature resulting from less cooling time and lower cooling rate as build height increases [45] [46]. The parts were significantly darker on the top surface after all of the other components were built. Since the parts were also approximately 2" off the build plate, the build plate does not play a significant role in dissipating heat. Thus, excess heat is built up in the z oriented rods.

The tensile specimens may have slight changes in microstructure which may lead to preferential breaking. To confirm this effect, a test cylinder was built with other samples. The height of the cylinder extended beyond the height of the remaining samples. The microstructure was darker at the height where the cylinder was built with other samples versus where the cylinder was built alone (Figure 4.14b). The lighter region also had a slightly lower hardness of approximately 2-3 Rockwell C (converted from Vickers) lower than the darker region [45]. The microstructural and hardness data suggests that the cooling between layers is significantly greater at a height where the part with a uniform cross section is being built with other parts in comparison to where same part is being built alone. Thus, this increasing the time by reducing the recoating speed from the final to the initial position between scans may prove to be beneficial because there is more time for the part to dissipate heat [45].

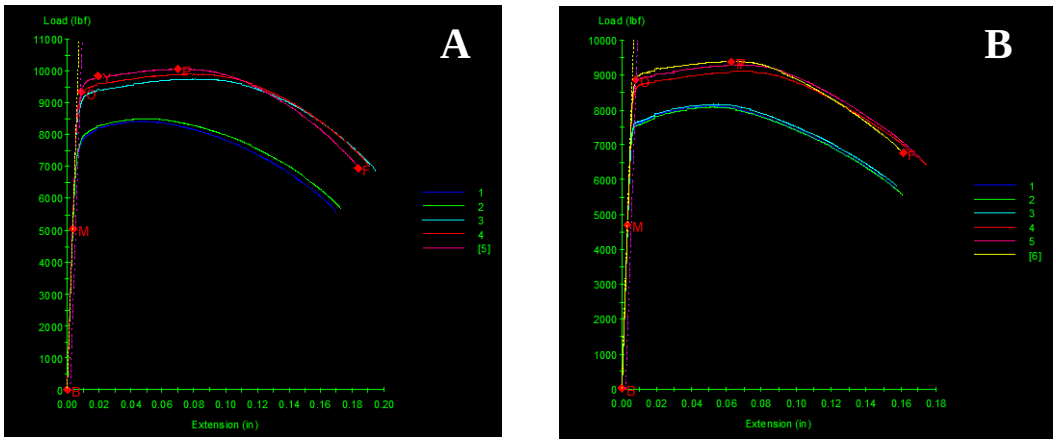

Figure 4.12 Stress strain curves for parameter A in the as sintered (A) and stress relieved (B) conditions.

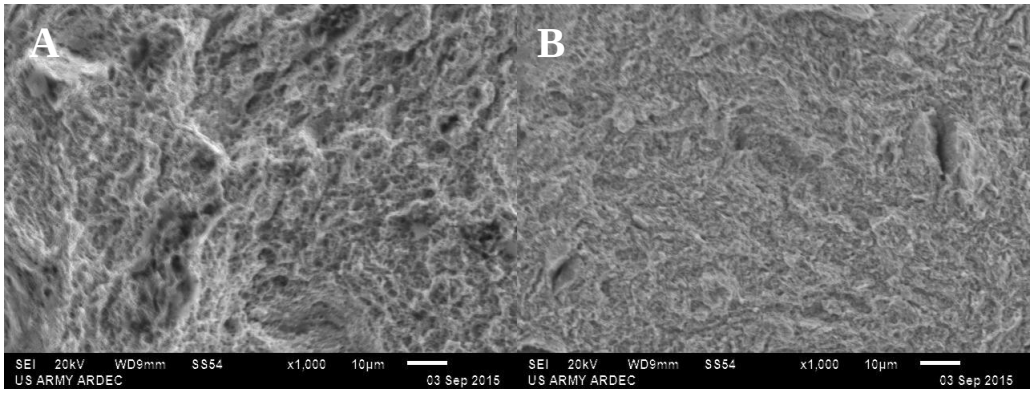

Figure 4.13 Fracture surface of parameter A in the as sintered (A) and stress relieved (B) conditions.

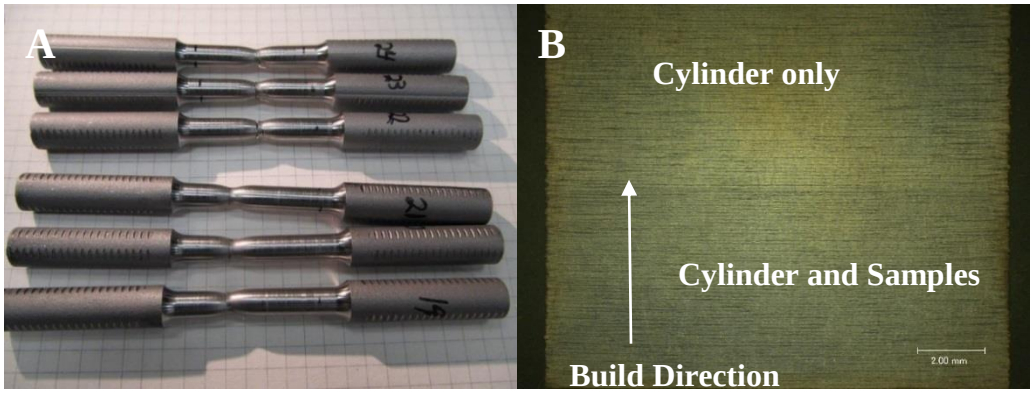

Figure 4.14 Overall image of the pulled tensile specimen parameter set B, Table 4.9 (A) and microstructure of test cylinder (B).
Source: [45].

4.7.2 Heat Treatment

The yield strength, tensile strength, and elongation are nearly isotropic for the three parameters [Table 4.9 (Figure 4.15-4.17)]. The fracture surface indicates ductility with small voids in the microstructure in the heat treated condition (Figure 4.18). However, the vertically oriented bars fractured near the same height which means that the thermal effects are affecting the mechanical behavior even after heat treatment. It may mean that there is slightly higher porosity or slight differences in structure near the height of failure.

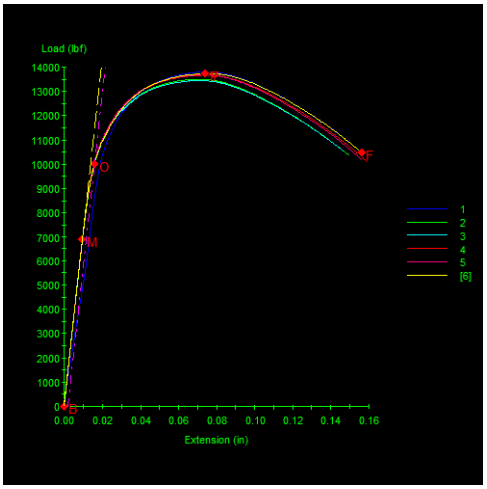

Figure 4.15 Stress strain curve of parameter A in the heat treated condition.

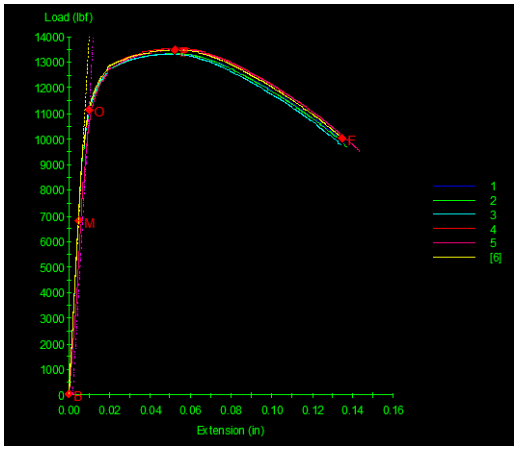

Figure 4.16 Stress strain curve of parameter B in the heat treated condition.

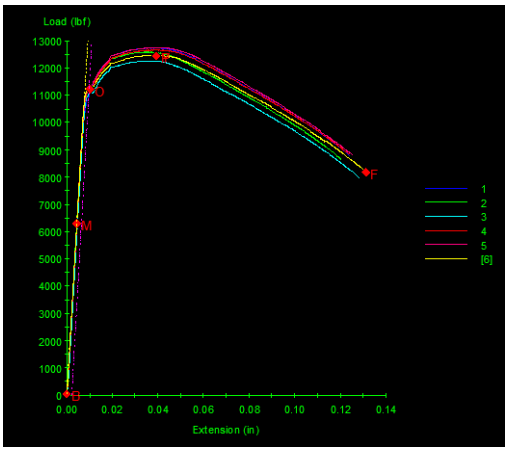

Figure 4.17 Stress strain curve of parameter C in the heat treated condition.

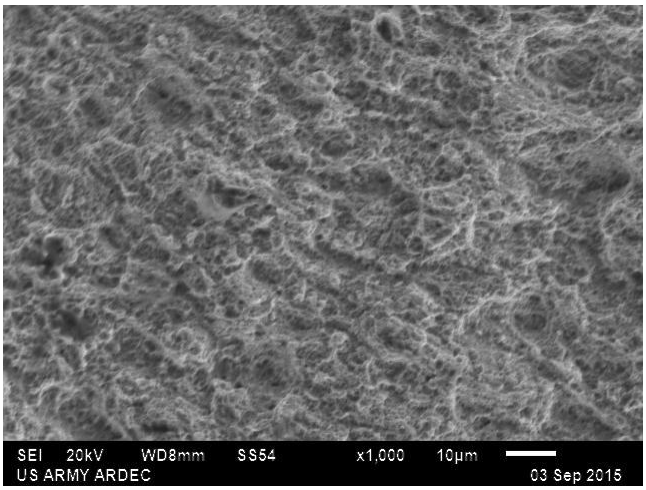

Figure 4.18 Fracture surface of parameter A from Table 4.8 in the heat treated condition.

4.8 Charpy Impact Toughness

Preliminary Charpy testing indicates that the toughness varies as a function of heat treatment condition. In all cases, the notch is oriented in the x-y direction. The parameter set B was selected for repeatability studies because the tensile results and preliminary Charpy results were slightly better than A and C in the heat treated condition (Table 4.10). According to microstructural analysis, parameter B has minimal porosity without evidence of cracking which supports the results of mechanical tests (Figure 4.19).

Table 4.10 Charpy Impact Testing Results According to ASTM 23 with Notch Oriented in X-Y Direction Tested at 80°F using Parameters from Table 4.8

Sample ID	Toughness (J)	Lateral Exp. (mils)	Shear Area (%)
A as sintered	85	35	32
A stress relieved	75	36	42
A heat treated	22	6	22
B heat treated	24	4	22
C heat treated	22	5	22

Source: [47].

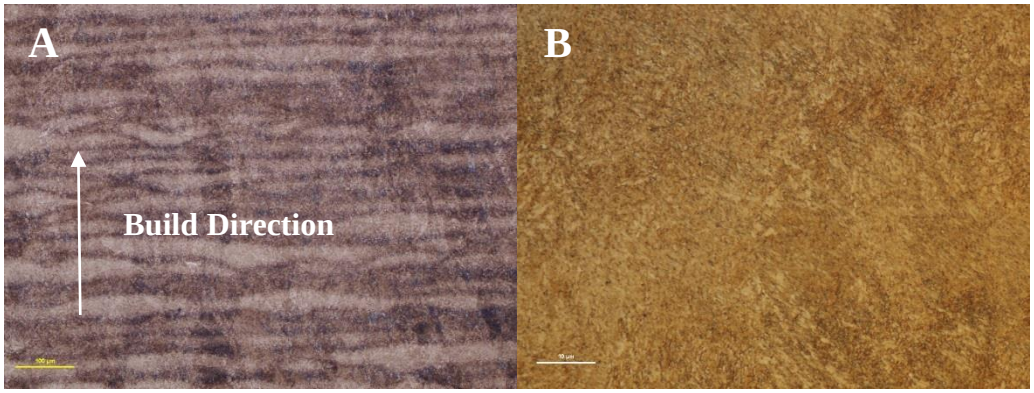

Figure 4.19 As sintered microstructure in longitudinal direction. The scale bars read 100 and 10 microns for (A) and (B), respectively.
Source: [45].

4.9 Conclusion

Laser power and scan speed are the most influential parameters for laser energy absorption near optimal energy densities at a particular layer thickness. The optimal parameters were selected near 130-140 J/mm^3. There is anisotropy in parts which is partly contributed by degree of cooling between layers during the build according to microstructural analysis. In addition, the optimal parameters show mechanical properties that are comparable to wrought after heat treatment and will be used in repeatability studies.

CHAPTER 5

REPEATABILITY STUDIES

5.0 Laser Parameter Microstructure and Mechanical Evaluation

The objective of this study is to evaluate the mechanical performance of builds to determine the factors which contribute to the repeatability of the process after laser parameter development.

5.1 Literature Review

Repeatability, location, and interlayer defects will be discussed based on a review of the literature. They have the potential to affect the mechanical performance of specimens.

5.1.1 Repeatability

The process has been shown to be repeatable according to literature review. According to a study on Inconel 718, Charpy toughness and porosity had minor variations after 14 builds. The particle size distribution increased slightly as well. The evidence shows that the process is repeatable [48].

There was another study in which virgin Ti-6Al-4V powder underwent 12 production cycles. The ultimate tensile strength of the bars was between 1000-1100 MPa and the density was higher according to Archimedes after 12 cycles. However, the size of the pores, and surface roughness in the build direction increased [49].

5.1.2 Location Effects

The National Institute of Standards and Technology (NIST) performed hardness measurements on 17-4 stainless in the as built and stress relief condition as function of location on the EOSINT M270. It showed that the machine can build components with fairly consistent mechanical properties [50].

5.1.3 Interlayer Defects

Large interlayer defects are typically caused by lack of fusion or gas pores. The effective cross sectional area can be significantly reduced for vertically oriented tensile specimens due to high concentration of planar defects. The morphology of the defects is important as well because defects with sharp edges can increase the stress concentrations which lead to inferior mechanical performance.

The anisotropic mechanical performance of components can be caused by interlayer defects. According to a study on 17-4 stainless, vertically oriented tensile and fatigue specimens are more sensitive to interlayer defects in comparison to horizontally oriented sample. The strength and fatigue properties were noticeably inferior in the vertical versus horizontal orientation. Defects include lack of fusion and/or gas pores which result in poor interlayer bonding. Since there are more layers in the z orientation and a smaller cross section, the vertical tensile results are likely to be more sensitive to interlayer process flaws than in the horizontal [51]. In another study, Charpy toughness testing was anisotropic due to planar defects. The V notch Charpy toughness was lower for the notch oriented in the x-y plane vs. the notch oriented in y-z plane (Figure 5.1) [52]. Interlayer flaws are caused by process defects provided that the laser is in proper working order and laser parameters are optimal.

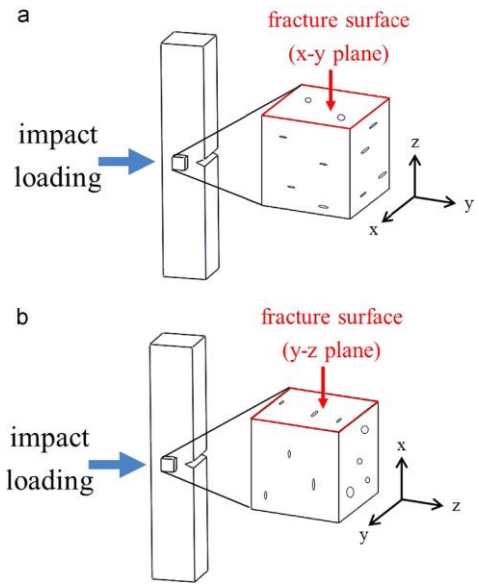

Figure 5.1 Demonstration of the orientation of the fracture surface for Charpy study.
Source: [52].

5.2 Verification Builds

After the parameter development phase, mechanical behavior was evaluated as a function of location and orientation for each build to evaluate the process using optimal parameters (Table 5.1). The same build was repeated three more times consecutively [45].

Table 5.1 Parameter Set 4340 Steel: Layer Thickness 20 Microns and 4mm Stripe Width

Power Watts	**Hatch Distance** mm/sec	**Laser Speed** mm/sec	**Energy Density** J/mm^3
185	0.10	700	132.1

Source: [45].

5.2.1 Experimental

Each build was divided into five clusters or locations: the four corners and the center of the build plate (Figure 5.2). The horizontal (x-y) and vertical (z) orientations were tested with

tensile, fracture toughness (K_{1C}) and v-notched Charpy impact testing. However, the K_{1C} specimens were only in location 3, not the four corners. The powder was sieved through a 63 micron screen after each build to remove the large particles. The Charpy and tensile properties were evaluated at all five locations. The mechanical test specimens were heat treated to 51 HRC according to the previously described process. The tensile bars were machined and tested in accordance with ASTM E8 [42]. The Charpies were milled and notched with a double angle cutter and then tested in accordance with ASTM E23 [47]. The K_{1C} notches were EDM'ed (Electrical Discharge Machined) and surfaces were ground and then tested in accordance with ASTM E399 [53]. Each specimen was built with a three-digit label: the first digit represents build number (1 – 4), the second number represents location (1 – 5), and third number represents specimen number within the defined location. Three specimens were tested for each condition. For example, sample 123 represents build 1, location 2, and specimen 3. Specimen number 1 through 3 are built in the vertical or z direction. Specimen number 4 through 6 are built in the x-y or horizontal direction. The metallurgical cubes are labeled with two numbers: the first is build number and the second is location [45]. 22-53 micron powder was used.

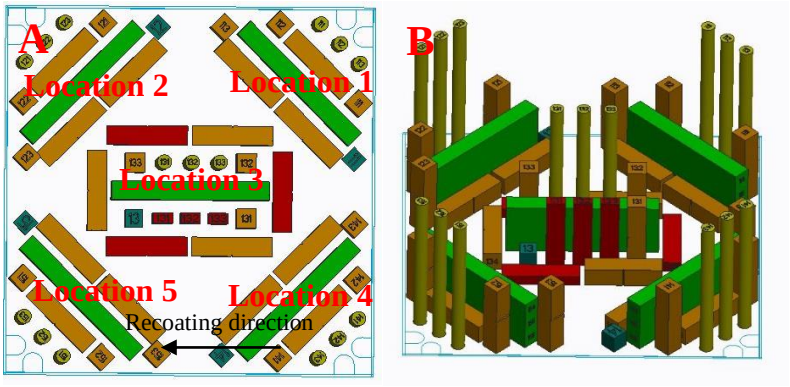

Figure 5.2 (A) Top view image of the verification and (B) ISO image of the build plate.
Source: [45].

5.2.2 Overall Tensile Results

The tensile strength, yield strength, and elastic modulus were consistent across the specimens. There were variations in ductility or elongation and the Charpy impact toughness results varied which will be discussed in the following sections - 5.2.3-5.2.6 [45].

5.2.3 Build Anomalies

There were three tensile specimens that exhibited brittle behavior (included in Table 5.2). Samples 122 and 152, which were z oriented tensile bars, fractured near the same height. There appears to be large defects with evidence of lack of fusion (Figure 5.3). They were in line with each other on the build and relatively farthest away from the dispensing bin (Figure 5.2a). Thus, this indicates that the powder did not fully cover the tensile bars near that height for several layers which would cause weak interlayer bonding [45].

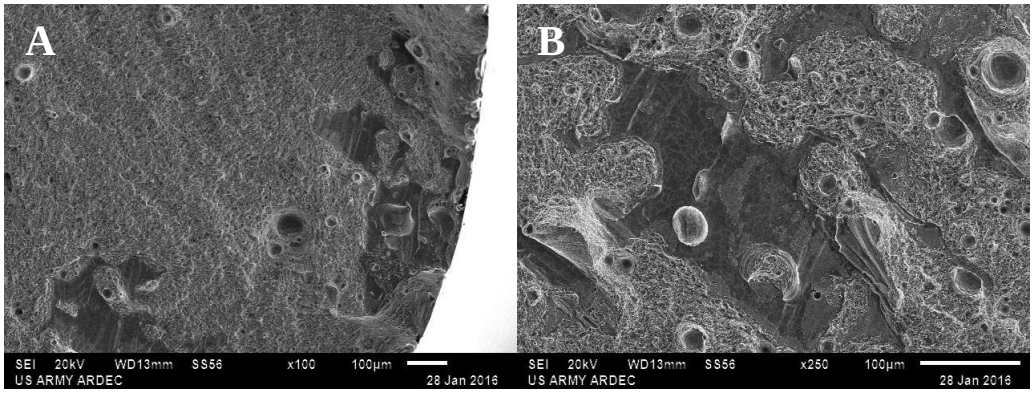

Figure 5.3 (A) 100x image of fracture surface of specimen 122 (B) 100x image of fracture surface of specimen 152.

The 3rd build anomaly occurred in z tensile sample 431 during build 4. The failure occurred in the radius for tensile specimen grip and there appears to be large defects in the

structure according to Figure 5.4 [45]. One explanation may have been that the recoater blade jammed several times on the tensile block in location 2 just below the height at which the fracture occurred. The raised surfaces were filed down and the task continued until completion. Thus, the interrupted layers may not have strongly bonded to each other as subsequent layers [45]. Another possible explanation may have been that condensate could have reached the lens or fell on the part due to long duration of the build ~(180 hours). It is recommended that the lens be cleaned after 75 hours of build time [54]. Condensate particles can interact with the laser which can absorb laser energy and scatter the laser beam which will then bond non-melted particles to the surface. Therefore, it will effectively decrease the laser energy reaching the powder layer [55]. As a result, the beam may not be able to effectively melt the powder which can lead to significant defects [45].

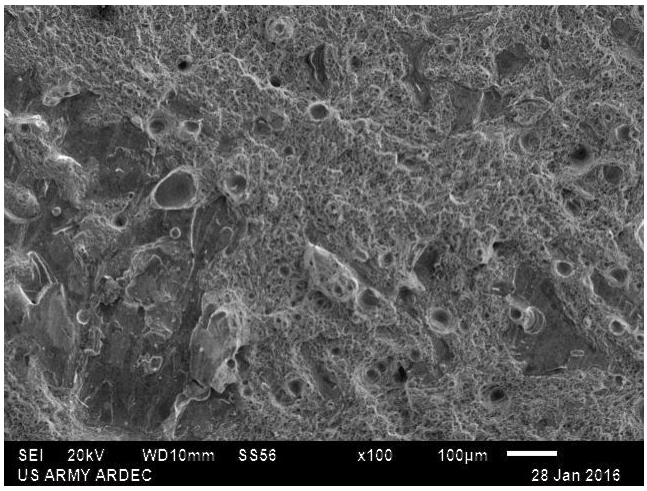

Figure 5.4 100x image of fracture surface of specimen 431.

Table 5.2 Z Oriented Tensile Bars which Exhibited Brittle Failure

Sample number	**Modulus** Mpsi	**Yield Strength** ksi	**Tensile Strength** Ksi	**Elongation** %
122	29	221	282	2.5
152	29	220	278	3.3
431	29	221	263	2.0

Source: [45].

There were also three tensile rounds (111, 112, 113) which were knocked over during the first build and the recoater jammed after the formation of several layers. The knock over was caused by poor part adhesion to 4340 build plate which may be attributed to the surface chemistry and/or condition. The next three builds were on low-carbon steel plate [45].

5.2.4 Tensile Results in Horizontal Orientation

The laser parameters chosen were proven to be effective for builds 1-4 because the average x-y tensile mechanical properties were comparable to wrought at all locations. However, there were two specimens, 324 and 424, at location 2 which had significantly lower elongation values in comparison to the other samples in Table 5.3 [45]. These were located on top region of the tensile block (highest z). Location 2 had the lowest elongation and highest relative standard deviation in the x-y direction compared to the other locations (Table 5.3) [45].

Table 5.3 Results of the Horizontally Oriented (X-Y) Tensile Bars

Sample name	**Modulus** Mpsi	**Yield Strength** ksi	**Tensile Strength** ksi	**Elongation** %	**Standard Deviation of Percent Elongation** %	**Percent Relative Deviation of Percent Elongation** %
Build 1	29	223	284	11.7	0.6	4.8
Build 2	28	224	284	11.7	0.8	7.1
Build 3	29	223	282	11.7	1.1	9.0
Build 4	29	222	282	11.2	1.4	12.1
Location 1	29	223	283	11.6	0.8	6.8
Location 2	29	223	283	10.7	1.5	13.8
Location 3	29	224	284	11.8	0.5	4.0
Location 4	28	223	282	12.1	0.8	6.7
Location 5	29	223	282	11.6	0.7	6.2
X-Y	29	223	283	11.6	1.0	8.6
324	29	220	281	9.2	N/A	N/A
424	29	220	277	6.7	N/A	N/A

Source: [45].

5.2.5 Tensile Results in Vertical Orientation

The z oriented percent elongation varied significantly from build to build. Builds 1 and 3 have significantly higher elongation and lower standard deviation than builds 2 and 4 (Table 5.4). New filters were used during build 1 and build 3 [45]. The gas flow was significantly better during builds 1 and 3 because the filters were not as clogged in comparison to builds 2 and 4. Gas flow is important because the fan removes the condensate particles [45]. Gas flow rate likely decreased as the filters were getting clogged. There was evidence of significant porosity on the fracture surface of the tensile specimens (Figure 5.5). The reduction in condensate removal would lead to an increase in laser interaction with the condensate which results in process defects. Location 2 (top left of Figure 5.2a) performed the worst across the board. Location 2 had the lowest percent elongation and highest relative standard deviation compared to the other locations [45].

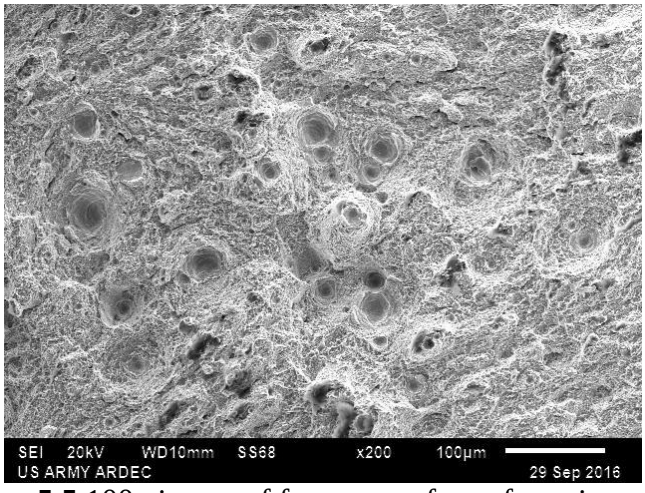

Figure 5.5 100x image of fracture surface of specimen 452.

Table 5.4 DMLS 4340 Steel, Heat Treated Condition, Z Orientation. The 3 Samples in Table 5.2 were not Included in the Data Set

Sample name	**Modulus** Mpsi	**Yield Strength** ksi	**Tensile Strength** ksi	**Elongation** %	**Standard Deviation of Percent Elongation** %	**Relative Standard Deviation of Percent elongation** %
Typical Wrought	29	220	270	11	N/A	N/A
Build 1	29	222	285	10.5	0.7	6.3
Build 2	29	223	280	9.0	1.6	18.0
Build 3	29	223	282	11.5	0.7	5.7
Build 4	29	221	279	9.9	1.2	12.6
Location 1	29	222	281	10.7	1.3	11.7
Location 2	29	221	280	9.2	2.1	23.2
Location 3	29	223	282	10.6	0.8	7.5
Location 4	29	223	282	10.2	1.4	13.8
Location 5	29	223	281	10.3	1.0	9.4
Z	29	222	281	10.2	1.4	14.1
X-Y	29	223	283	11.6	1.0	8.6

Source: [45].

5.2.6 Charpy Impact Toughness Results

The impact toughness in build 4 was inferior to the other builds which may be attributed to multiple build stoppages near the height where the notch was cut in the z direction which may result in poor interlayer bonding [45]. The average impact toughness was the lowest and the variance was the highest for location 2 as well.

Mechanical testing indicated inferior mechanical performance at location 2 which was likely caused by poor gas flow in that region in general because it was the worst performing region by far according to the mechanical testing (Tables 5.3-5.5). In another study conducted by Ferrar et.al, the gas flow was improved by modification of the rail design with nozzles and diffusers which provide a more uniform gas flow across the build platform [55]. As a result, more condensate particles were removed and there was less

variation in porosity and compressive strength of the titanium samples in comparison to the initial design [55]. Condensate removal is an important aspect of the process [45].

Another study from Lawrence Livermore National Labs shows that the melt pool geometry is affected by inert gas pressure. At lower Ar gas pressure, the melt pool height was significantly smaller while the powder depleted region on the side of the melt pool increased [56]. The ejection of particles from the melt was dominated by the vapor pressure during the sintering process. Meanwhile, at higher inert pressure, more powder particles are attracted to the melt which creates larger melt pool and smaller powder depletion region. Thus, significant changes in gas flow can create defects which can degrade the mechanical performance [56].

Table 5.5 DMLS 4340 Steel V notch Charpy and Fracture Toughness Results

	Charpy ft-lb	**Standard Deviation of Charpy** ft-lb	**Percent Relative deviation of toughness** %	**K_{Ic}** (Ksi-$in^{½}$)	**K_{Ic} Standard Deviation** (Ksi-$in^{½}$)	**K_{Ic} Percent Relative Deviation** (%)
Build 1	12.1	1.7	14	49.5	0.6	1.2
Build 2	12.0	1.7	14	47.3	1.0	2.2
Build 3	12.7	2.0	16	49.3	0.5	1.0
Build 4	11.0	1.9	18	48.6	1.8	3.7
Location 1	11.9	1.7	14			
Location 2	11.0	2.6	23			
Location 3	12.7	1.6	13	48.7	1.4	2.8
Location 4	12.3	1.6	13			
Location 5	11.9	1.8	15			

Source: [45].

5.2.7 Chemistry Evaluation of Part

The powder was mixed 50/50 by weight from two different lots of powder. Lot A was recycled powder and lot B was virgin powder. The part was analyzed using optical

emission spectroscopy and combustion analysis for carbon and sulfur content. The chemistry of the part is comparable to the chemistry of the certified powder according to Table 5.6. Lot B had slightly higher combined phosphorus and sulfur which can lower the ductility and fracture toughness to a certain degree [57].

Table 5.6 Comparison of the Chemistry of the Powder Versus Chemistry of the Part

Element	**Lot A from certification** wt%	**Lot B from certification** wt%	**Part chemistry** wt%
C	0.39	0.39	0.39
Mn	0.62	0.66	0.61
P	0.004	0.012	0.012
S	0.005	0.006	0.007
Si	0.24	0.23	0.24
Ni	1.9	1.98	1.85
Cr	0.88	0.90	0.92
Mo	0.27	0.28	0.30
Fe	Bal	Bal	Bal

Source: [45].

5.2.8 Powder Analysis

The powder was slightly coarser and had a slightly higher oxygen content in comparison to initial blend of powder. The slight coarsening and higher oxygen content is likely caused by the condensate formation during the sintering process (Table 5.7). In another study conducted by O'Leary et al., the particle size of titanium increases because the amount of finer particles are reduced and the quantity of larger particle increased as well [58].

Table 5.7 Powder Size and Oxygen Content of the Powder Before Build 1 and After Build 4

Powder Type	**D10** μm	**D50** μm	**D90** μm	**Oxygen content** wt%
Original mix	27.39	39.01	57.29	.061
After Build 4 sieved	31.01	44.81	65.57	.067

Source: [45].

5.2.9 Abbreviated Repeatability Study

The lessons learned from the verification builds were to avoid location 2 and change filters at less than 275 laser hours. Furthermore, the feed rate must be adequate during the recoating operation. The purpose of this study was to evaluate z oriented tensile samples in order to determine repeatability after following the lessons learned from the verification builds. Tensile data was collected for six builds from the top right corner to evaluate repeatability of the process. The yield, tensile strength, and elastic modulus of the parts are consistent (Table 5.8). There is a slight deviation in elongation. The data shows that if a manufacturing plan is followed; the mechanical properties can be repeatable.

Table 5.8 Tensile Results for Vertically Oriented (Z) Tensile Bars

Sample description	**Modulus** Mpsi	**Yield Strength** ksi	**Tensile Strength** Ksi	**Elongation** %
Build 1	30	175-177	184-186	14-16
Build 2	30	174-176	182-185	14-16
Build 3	30	174-176	182-185	16-17
Build 4	30	168-171	179-181	17
Build 5	30	170-172	177-181	15-17
Build 6	30	167-172	176-181	14-17

5.3 Conclusion

There were factors in addition to laser parameters which affect the repeatability of the process. For instance, consistent gas flow is needed to reduce variation in the mechanical properties as a function of location. The location 2 of the machine appears to have inferior gas flow in comparison to the other locations. Furthermore, the filters need to be changed prior to getting clogged. Effective powder coverage should be verified for each layer. The repeatability study showed the ability of the DMLS process to produce mechanically sound parts on a consistent basis provided that the manufacturing plan was followed.

CHAPTER 6

MECHANICAL AND METALLURGICAL EVALUATION AS A FUNCTION OF BUILD ANGLE

6.1 Design Considerations

There are several reasons for regions of a component to be built at an angle from the horizontal during the laser powder bed fusion process. For instance, it is preferable to minimize the scanned area for each layer by increasing the build angle of the largest cross section to minimize distortion. Residual stress can cause larger parts to deflect and distort significantly as demonstrated on a triangular prism built vertically and horizontally [59]. The prism built horizontally (largest cross section) had much higher displacement than the same prism built vertically according to digital image correlation. Furthermore, support structure removal may only be feasible in certain part orientations for components. In addition, internal structures such as lattice structures or channels give rise to angled features which may not be able to be surface finished. Therefore, mechanical and metallurgical behavior of the near net shape specimens due to build angle variation is also needed to understand the process.

6.2 Experimental

4340 tensile specimens were built near net shape between 35 and 90 degrees from the build plate surface with the parts angled away from the recoater (Figure 6.1a-b). The tensile specimens were then stress relieved at 1100^{o}F [45]. There were four tensile specimens analyzed in the as built condition and bead blasted with steel beads. The surface roughness

of sample blocks was analyzed using 3D optical profilometry. The roughness was measured by four scans 45^{o} apart on the top and on the bottom block surfaces (see Figure 6.1b). The Average Roughness (Ra) and RMS (Root Mean Square) surface roughness was measured on the top and the downward facing surfaces of the blocks angles built at 35, 45, 60 and 90 degrees from the surface. The Ra is the average of the peaks and valleys. RMS is the deviation of roughness from the mean [45]. 22-53 micron powder was used.

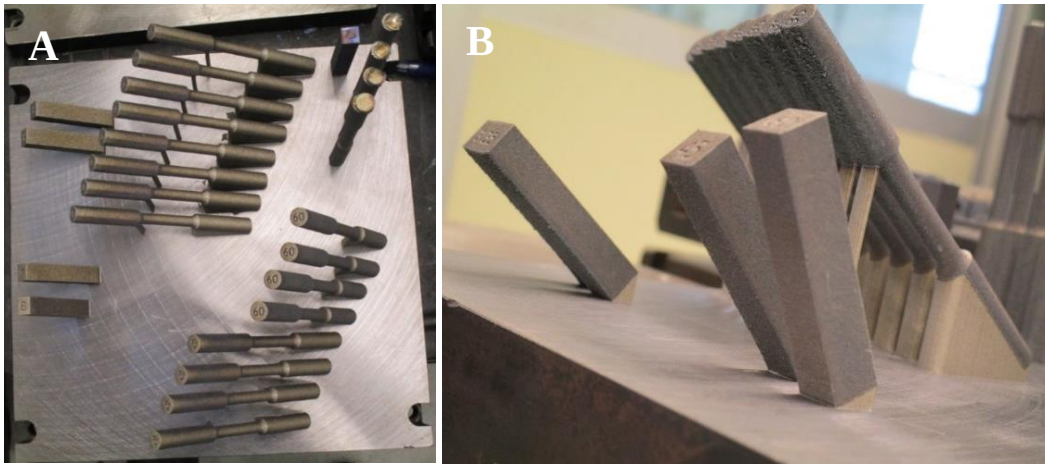

Figure 6.1 (A) Top view image of the surface angle and (B) back view of the build plate *Source:* [45].

6.3 Surface Roughness and Mechanical Performance of Surface Angle Components

The results show that there is a significant difference in tensile properties and surface roughness as a function of build angle from the horizontal after stress relief (Tables 6.1 and 6.2). Generally, the elongation values increase as the build angle is increased from 35 to 90 degrees [45]. However, there were three tensile specimens at 45 degrees which were significantly more brittle than the rest. After investigation of the fracture surface, there were areas that were indicative of lack of fusion with unfused particles (Figure 6.2a). There was evidence of ductility in the fracture surface (Figure 6.2b). In situ process monitoring

techniques will be needed to determine the exact cause of brittle failure [45]. One possible explanation is that the angle of incidence of the laser with the 45 degree specimens are not consistent as a function of position which may lead to locally high energy absorption of the powder bed [60]. Thus, it may lead to higher recoater and sample interaction during the application of powder [45].

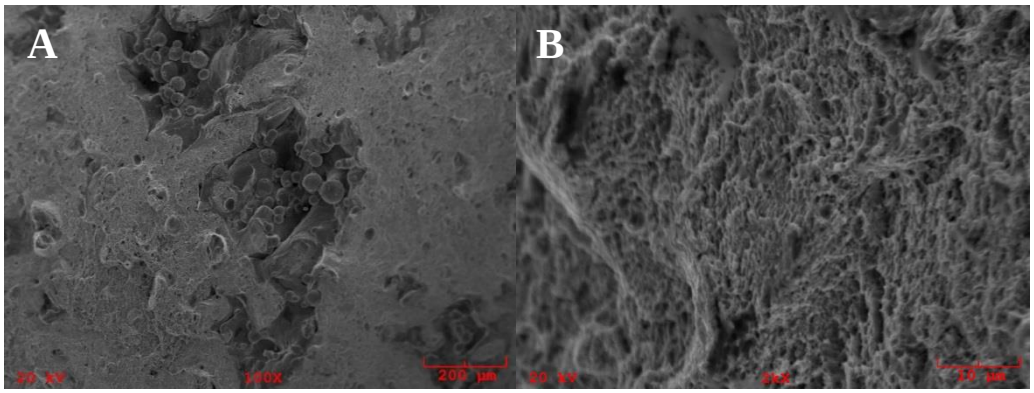

Figure 6.2 150x (A) and 2,000x (B) of 45 degree as built condition.
Source: [45].

The fractures were typically off center on all the specimens and fracture was typically located towards the top of the specimen (Figure 6.3a.) [45]. The 90 and 35 degree specimens were softer on the top versus the bottom according to microhardness results (Table 6.3). This is similar to the phenomenon described in section 4.7.1. That is, as shorter items complete building, the laser returns quickly to the remaining parts resulting in more heat input [45]. Furthermore, when samples are angled between 35 and 60 degrees, the downward (bottom) surface facing the plate is rougher than the top because the top surface has more solid material underneath to absorb the laser energy (Figure 6.4). Thus, more of the surrounding particles will fuse to the bottom surface and create a slightly elliptical cross section (Figure 6.3b). The fracture initiation site is at the transition from

rough to smooth surface (Figure 6.3b.). This transition point coincides with the narrowest cross section [45].

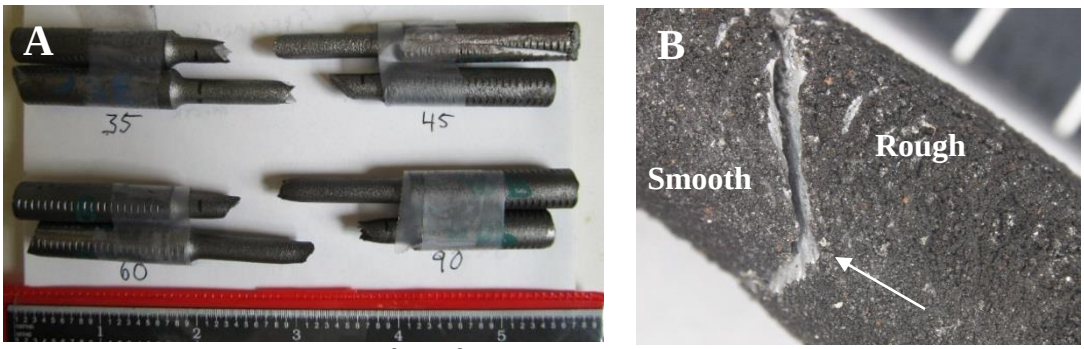

Figure 6.3 Overview image of the fractured bead blasted specimens (A) and low magnification image of the fracture region of the tensile specimen (B).
Source: [45].

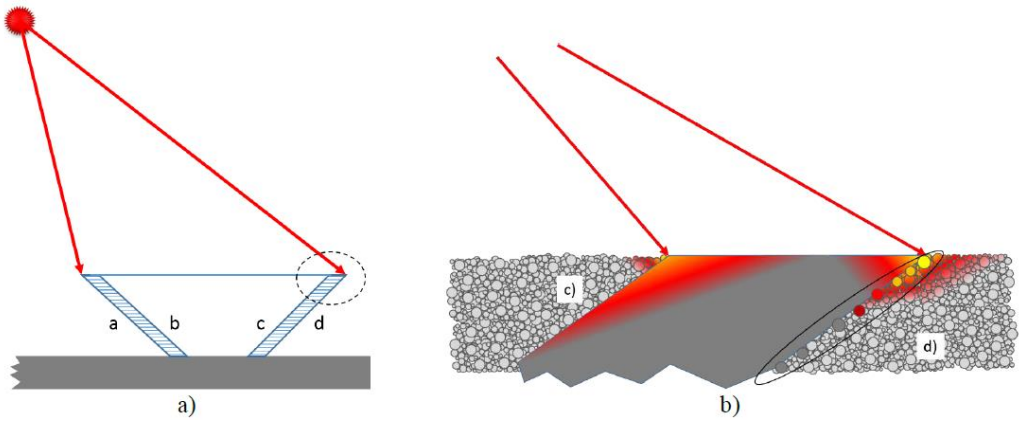

Figure 6.4 Schematic of the laser with the angled surface. Regions c and d represent the top surface and bottom surfaces, respectively.
Source: [60].

Bead blasting reduced the surface roughness of the specimens by the removal of some of the surface imperfection which include partially melted surface particles (Table 6.2). As a result, the mechanical performance improved slightly for 35 degree samples (Table 6.1). Thus, surface finishing may be needed depending on the mechanical criticality

of the part because there are large differences in the ductility between 35 and 90 degrees [45].

There has been supporting data which concluded that bead blasting and machining improves the mechanical performance of L-PBF parts. For instance, it has been shown that bead blasting resulted in an increase in the compressive strength by phase transformation and decrease in surface roughness of 17-4 stainless steel [61]. In addition, machined surface showed significant improvement in mechanical performance in comparison to near net shaped vertical tensile specimens for 17-4 stainless and Ti-6Al-4V for this process [62]. Fatigue evaluation was performed on Ti-6Al-4V in another study. The specimens which were as built and HIP'd (Hot Isostatic Pressed) had lower fatigue properties than machined and HIP'd. Therefore, surface defects likely contributed to the slight reduction in their mechanical performance [63].

Table 6.1. Mechanical Performance of Near Net Shaped Tensile Specimen in the As Built (AB) vs. Bead Blasted (BB) Condition

Sample Description	**Modulus** Mpsi	**Yield Strength** ksi	**Tensile Strength** Ksi	**Elongation** (%)
90 ^{o} Machined	30	170-175	179-183	15-17
90^{o} AB	26-28	157-167	173-176	14.4-14.9
90^{o} BB	28-29	161-167	175-176	14.4-15.0
60^{o} AB	28	165-169	174-177	11.8-12.6
60^{o} BB	29	166-168	177-179	11.6-12.4
45^{o} AB	28	165-168	165-176	1.6-9.8
45^{o} BB	29	168-170	176-180	2.9-12.3
35^{o} AB	28	160-164	170-171	9-10.6
35^{o} BB	28-30	164-170	174-181	10.0-11.0

Source: [45].

Table 6.2 Surface Roughness Evaluation of Near Net Shaped Block Specimens in the As Built (AB) vs. Bead Blasted (BB) Condition

Sample Description	**Average Surface Roughness-Ra Top Surface** μm	**Average Surface Roughness Bottom Surface Ra** μm	**Average Surface Roughness Top Surface Rrms** μm	**Average Surface Roughness Bottom Surface Rrms** μm
90° AB	13.8*	13.8*	16.8*	16.8*
90° BB	5.9*	5.9*	7.6*	7.6*
60° AB	13.5	14.6	16.4	17.8
60° BB	7.3	7.3	9.3	9.2
45° AB	18.5	34.3	22.8	42.4
45° BB	7.2	11.9	9.3	15.1
35° AB	18.9	49.4	23.5	60.7
35° BB	7.6	20.8	9.6	26.1

*surface roughness testing of 90 degree was performed on the sides of the specimens only. The overall average values were noted.
Source: [45].

Table 6.3 Hardness Evaluation of Block Specimen in the As Built (AB) vs. Bead Blasted (BB) Condition

Sample Description	**Hardness Vickers** HV	**Hardness Rockwell converted from Vickers** HRC
90° BB Bottom	380-401	39-41
90° BB Top	347-355	35-36
35° AB Bottom	382-402	39-41
35° AB Top	371-388	38-40

Source: [45].

6.4 Conclusion

The DMLS process enables the designer to build more complex parts which gives rise to features with angles. However, the mechanical properties are dependent on build angle. Increasing the surface angle from the horizontal generally improves the mechanical properties and decreases surface roughness. Bead blasting improves these properties slightly.

CHAPTER 7

RESIDUAL STRESS

7.1 Literature Review of Residual Stress in DMLS Parts

Residual stress is the amount of stress remaining after the external stresses are removed. During DMLS, large thermal stresses are generated because the process is a non-equilibrium process due to high heating and cooling rates. The laser source melts the powder rapidly to a create melt pool. The pool solidifies rapidly leading to high thermal stresses. During melting, the top of the melt pool produces compressive stresses on the substrate because the underlying layer is restricting expansion. When the melt pool cools, it produces tensile forces on the underlying substrate as it contracts. If the forces are greater than the yield strength, it will result in delamination of the layers [64]. In general, the residual stress increases when the energy density increases when one parameter is changed.

Layer thickness is also a factor that influences residual stress. If the layer thickness is decreased while all the other parameters remain the same, the deflection is shown to increase [65].

The hatch distance also contributes to residual stress. The hatch distance has been shown to have an inverse relationship to deflection. The hatch distance needs to be optimal for effective sintering because too small of a hatch distance will lead to an increase in overlap with the adjacent melt pool line. This leads to an increase in residual stress that may be attributed to a higher concentration of energy in a small region [66].

In a study performed by Kruth et al., bridges with overall dimension of (20mmx10mmx8mm) were built by powder bed fusion [67]. Then, the bridges were cut

off the built plate with electro discharge machining (EDM). The angular deflection of the bridges were measured. As the scan vector for building the bridges was decreased from 10mm to 2mm, the deflection decreased. During the build, the stripes were rotated so that the thermal stresses did not build up in the same location. When the rotation angle of the stripe was increased from the reference to 45 degrees, the deflection significantly decreased [67]. The stripes are rotated 67 degrees with the EOS system.

The build platform temperature is another factor affecting residual stress because the increase in temperature will lead to a decrease in deflection. The cantilever method was used to analyze deflection. Basically, the sides of the cantilever are held down by support structures. Then, the wire EDM cuts the supports off and the part deflects due to the thermal stresses. The deflection of the cantilever decreased significantly when the temperature was increased from 80^{o}C to 200^{o}C [65]. The degree in cooling is also decreased when the build platform temperature is increased. This will likely lead to smaller thermal stresses in the material which results in lower deformation.

7.2 Evaluation of Residual Stress on Arc Bridge Sample

Arc bridges were built to reveal residual stress effects. Arc bridges were built to the same specifications as indicated in the Kruth et al. report [67]. Residual stress was measured using XRD. Results for the as sintered and stress relieved are considered here. The residual stress is determined by measuring the strain in three different directions. After the part is cut off with a wire EDM, the ends of the bridges deflect up. Thus, it results in compressive stress. The two principal stresses were highly compressive (156 ksi) on the center of the bridge on top of the arc region and the side of the part on the surface and 0.006” in. At a

depth of 0.01” from the surface, the residual stress became tensile (Figure 7.1-7.2). When the bridge was stress relieved, the residual stress was significantly reduced. The compressive residual stress in the bridge is fairly high in the as sintered condition near and away from the arc. During the stress relief operation, the stress is significantly reduced.

As-Sintered, Over Arch - Stress

	0 deg (length)			-45 deg			-90 deg (width)		
Depth [in]	Stress [ksi]	Dev. [ksi]	Peak Width [°]	Stress [ksi]	Dev. [ksi]	Peak Width [°]	Stress [ksi]	Dev. [ksi]	Peak Width [°]
0.000	-62.6	4.6	6.43	-44.1	3.9	6.37	-45.5	4.3	6.34
0.006	-156.3	15.8	6.82	-129.0	12.1	6.79	-106.7	16.3	6.63
0.010	4.3	3.9	3.39	41.2	2.6	3.33	83.8	2.5	3.31

Figure 7.1 Residual stress results - courtesy of American Stress Technologies for the as-sintered condition over the arch.

Stress Relieved, Over Arch - Stress

Depth	0 deg (length)			-45 deg			-90 deg (width)		
	Stress	Dev.	Peak Width	Stress	Dev.	Peak Width	Stress	Dev.	Peak Width
[in]	[ksi]	[ksi]	[°]	[ksi]	[ksi]	[°]	[ksi]	[ksi]	[°]
0.000	-4.1	1.1	2.88	-1.6	1.2	2.86	1.8	1.7	2.85
0.005	-17.5	3.6	2.93	-12.7	4.2	2.94	-6.8	2.9	2.94
0.010	-0.3	2.1	2.62	5.5	2.2	2.60	11.9	1.3	2.61

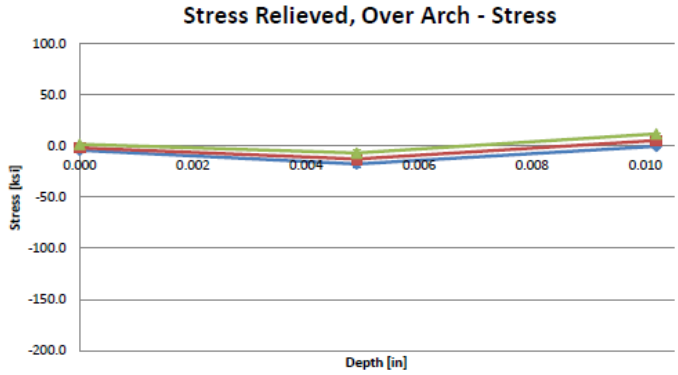

Figure 7.2 Residual stress results - courtesy of American Stress Technologies for the stress relieved condition over the arch.

7.3 DMLS 4140

When 4140 tensile specimens were built using 4340 steel parameters, there was significant cracking (Table 7.1). The cracking was oriented lengthwise when the bars were built in the x-y orientation. The fracture surface of sample A was featureless. Since the fracture surface did not reveal any ductile dimples, it indicated no ductility (Figure 7.3). Initially, it was surmised that the failure of 4140 was due to lower energy input due to lack of interlayer bonding. Thus, higher energy was then applied. The cracking got worse (Figure 7.4). The decrease in speed likely lead to a major deflection in the part which likely explained the significant cracking to the point that there was a complete crack in the part. The literature indicates that reducing the scan vector likely reduces the deflection. The island strategy scans random islands to reduce residual stress. In a study by Amanda Wu et al., it was shown that there was less tensile residual stress in 316L stainless when

3mmx3mm islands were used in comparison to 5mmx5mm islands scan strategy [59]. They used resonance ultrasound spectroscopy and strain from differential interference contrast to calculate the tensile residual stress. The island strategy would scan random islands to reduce residual stress. This report showed that a smaller scan vector reduced tensile residual stress [59]. Additionally, there have been studies in the literature indicating that the stripe width has an impact on residual stress. The change in temperature for the neighboring scans is less for smaller stripe width due to smaller cooling times. Thus, the localized thermal stresses are likely smaller at smaller stripe widths. If the scan vector is too large, the part can undergo significant warping and cracking [68]. Furthermore, according to previous studies, the stresses in the longitudinal direction of the melt pool was shown to have the highest residual stress because it is the direction of highest shrinkage. As a result, decreasing the scan vector may lead to a reduction in residual stress locally [69] [70].

A series of metallurgical cubes were built at 4mm stripe at various parameters to determine whether adjustments were needed. The vast majority of the samples did not reveal significant cracking (Table C.1 in Appendix C). Thus, tensile testing was performed for four different parameters with a 4mm stripe (Table 7.2). According to the tensile results, 4mm stripe eliminated much of the detrimental cracking to produce good mechanical test results (Table 7.3) (Figure 7.5). It is evident that the 4140 samples have a higher tendency to crack than 4340 even though the tensile test results were comparable to wrought (Figure 7.6). DMLS of 4140 is more prone to thermal stress likely because it may be subjected to higher stresses due to a lower hardenability and toughness which may make it more prone to phase transformations.

Table 7.1 Laser Parameter Sets used for 4140 at 10mm Stripe Width

Sample ID	**Scan Speed** (mm/sec)	**Power** Watts	**Hatch distance** mm	**Stripe Width** mm
A	575	185	0.12	10
B	525	185	0.12	10
C	500	185	0.12	10

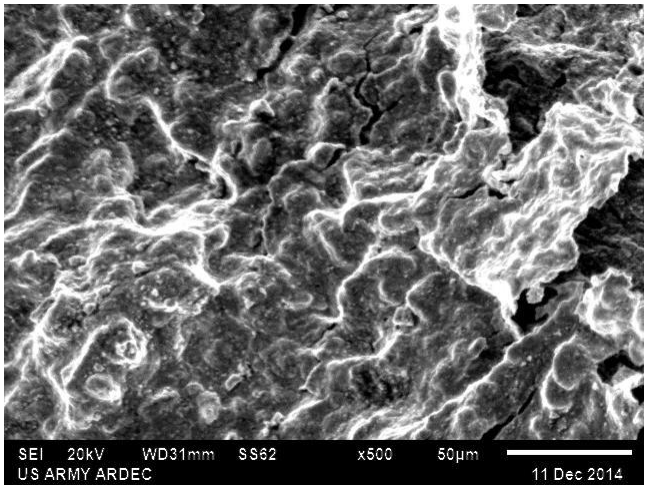

Figure 7.3 Fracture surface of 4140 steel using parameter set A from Table 7.1.

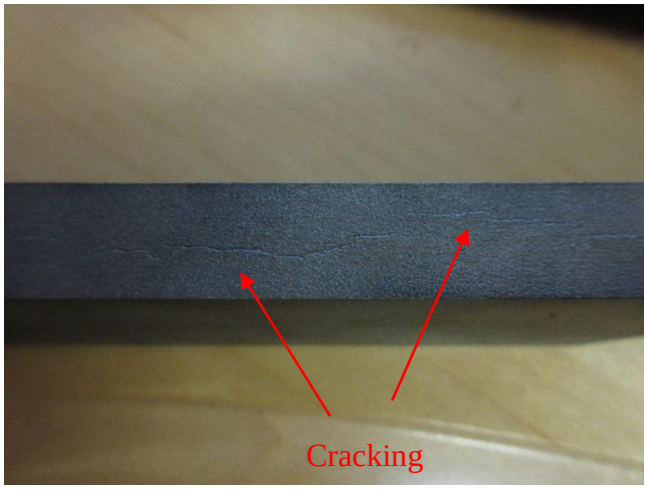

Figure 7.4 Photograph showing cracking using parameters 4140 sample C from Table 7.1.

Table 7.2 Laser Parameters used for 4140 at 4mm Stripe Width

Sample ID	**Scan Speed** (mm/sec)	**Power** Watts	**Hatch distance** mm	**Stripe Width** mm
A	700	195	0.10	4
B	750	195	0.10	4
C	600	195	0.12	4
D	650	195	0.12	4

Table 7.3 Tensile Data from 4140 Steel Heat Treated to 51 HRC at 4mm Stripe Width using Parameters from Table 7.2

Sample ID	**Modulus of elasticity** ksi	**Yield Strength** ksi	**Tensile Strength** ksi	**Elongation** %
A	30,000	227-231	291-293	10-13
B	30,000	230-232	293-296	10-13
C	30,000	229-232	291-292	12-13
D	30,000	228-232	291-292	11-14.9

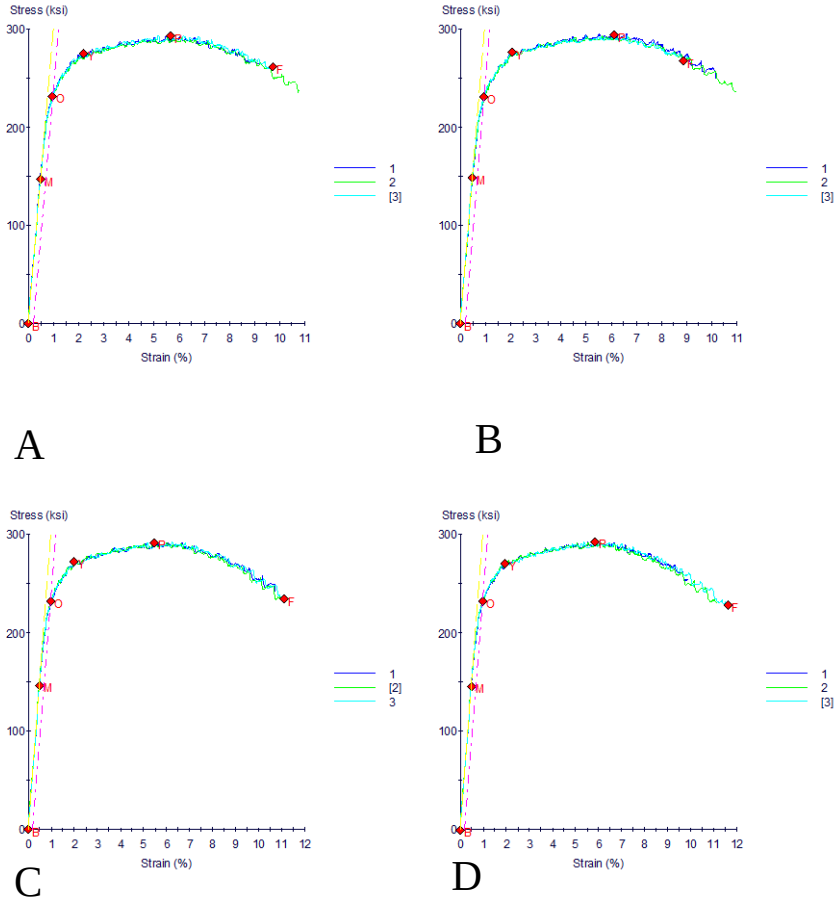

Figure 7.5 4140 stress strain curves sample A thru sample D from Table 7.3, respectively.

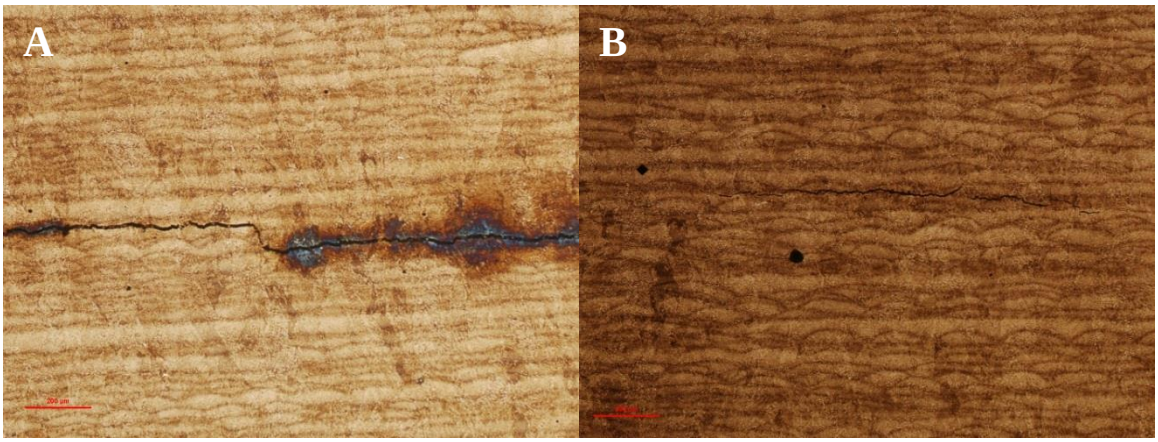

Figure 7.6 4140 Parameters 26 and 37 from Table C.1 from Appendix C. The scale bar represents 200 microns.

There are parameters which can sinter material with good mechanical properties. High density parts are produced at high energy densities. As a result, residual stresses are fairly high. A balance must exist for strong interlayer bonding while minimizing the residual stress on the specimen in order to obtain good mechanical properties without significant deflection and cracking.

7.3.1 Residual Stress Evaluation of Stripe Width for 4340 and 4140

Residual stress was analyzed using XRD of the top as built surface of 4140 and 4340 samples of 12mm x 12mm x (2.5-12mm) millimeter cubes at various stripe widths (2mm-20mm) under the plane stress condition with a Cu Kα source. A large bar with (x,y,z) dimensions of 10mmx108mmx10mm was built using parameters B-E (Table 7.4) for visual inspection.

There was high residual stress variation for 4140 steel as a function of stripe width. In particular, there was very high anisotropic residual stresses for 4 mm stripe width for 2.5mm thin samples (Table 7.5). There was a decrease in residual stress at 7.5mm part

thickness at 4mm stripe width. There may have been cracking which may have relieved some of the internal stresses. For larger bars, there was evidence of cracking on the surface at 10 and 20 millimeter stripe width for 4140 steel (Figure 7.7).

The 4340 bars did not exhibit cracking on the surface according to visual inspection. There is not a significant variation in residual stress in 4340 for each part thickness. Therefore, stripe width does not influence the residual stress significantly in 4340 (Table 7.6). Since 4340 has a higher hardenability and toughness than 4140 material, it is not as prone to cracking.

Table 7.4 Laser Parameters used for 4340 and 4140 XRD Measurements

Sample ID	**Scan Speed** (mm/sec)	**Power** Watts	**Hatch Distance** Mm	**Stripe Width** mm
A	575	185	0.12	2
B	575	185	0.12	4
C	575	185	0.12	7
D	575	185	0.12	10
E	575	185	0.12	20

Table 7.5 Residual Stress DMLS 4140 Particle Size (10-44 Microns) using Laser Parameter Set from Table 7.4

Stripe Width mm	**Sample Thickness** mm	σ_1 Ksi	σ_2 Ksi	T_{12} Ksi
2	2.5	-5.6	-50.5	22.5
4	2.5	103.9	-136.1	120.0
7	2.5	-22.5	-55.2	16.3
10	2.5	-10.1	-70.4	30.1
20	2.5	-26.5	-28.8	1.2
2	7.5	-6.3	-50.6	22.2
4	7.5	-37.1	-48.2	5.6
7	7.5	-18.1	-46.0	13.9
10	7.5	22.1	-29.6	25.9
20	7.5	-31.2	-34.5	1.7
2	12	29.9	-28.4	29.2
4	12	48.1	-49.0	48.5
7	12	24.6	-18.5	21.6
10	12	22.1	-29.6	25.9
20	12	22.2	-11.5	16.9

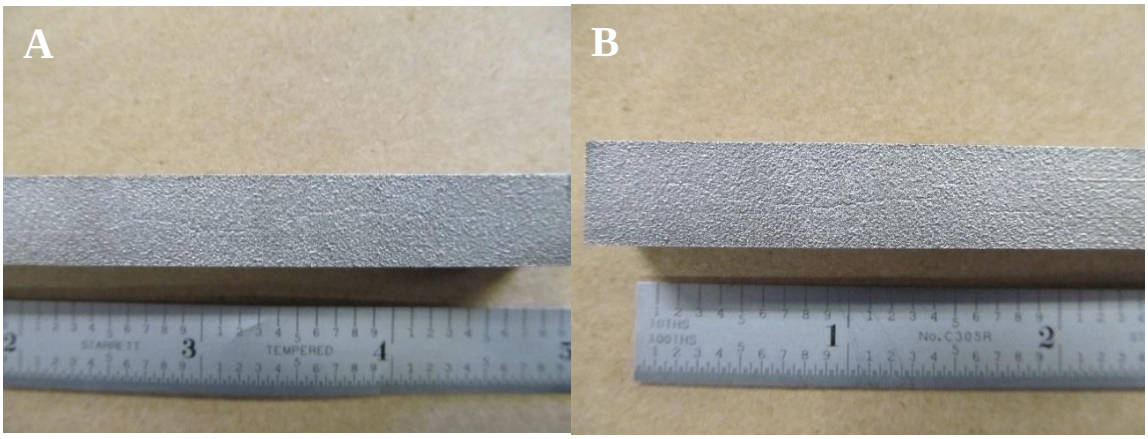

Figure 7.7 Surface of 4140 rectangular bar at 10mm (A) and 20mm (B) stripe width.

Table 7.6 Residual Stress DMLS 4340 Particle Size (22-53 Microns) using Laser Parameter Set from Table 7.4

Stripe Width mm	**Sample Thickness** mm	σ_1 Ksi	σ_2 Ksi	T_{12} Ksi
2	2.5	-13.2	-59.1	22.9
4	2.5	-18.9	-44.8	13.0
7	2.5	-7.7	-98.4	45.4
10	2.5	-8.3	-79.8	35.8
20	2.5	-2.6	-73.3	35.3
2	7.5	11.1	-72.9	42.0
4	7.5	-3.7	-41.2	18.8
7	7.5	-27.6	-34.9	3.6
10	7.5	3.5	-62.1	32.8
20	7.5	-10.5	-53.2	21.3
2	12	19.7	-14.2	16.9
4	12	21.0	-13.9	17.4
7	12	21.9	-34.2	28.0
10	12	3.2	-8.2	5.7
20	12	7.8	-21.3	14.5

7.4 Conclusion

4140 samples have a higher tendency to crack. Stripe width is likely needed to be decreased to reduce the thermal cycling and local longitudinal stress. There was no cracking observed for 4340 as a function of stripe width. It is likely due to the high hardenability and toughness of 4340 steel.

CHAPTER 8

L-PBF 4340 FRACTURE TOUGHNESS EVALUATION

8.1 Objective

The objective of this chapter is to evaluate the toughness of the material as a function of orientation and material condition. Toughness is used to assess the amount of energy needed to fracture in the presence of a flaw or notch. The material conditions include, as built, stress relieved and heat treated. K_{IC} fracture toughness testing will be used to evaluate toughness.

8.2 Previous Study of Fracture Toughness of Ti-6Al-4V

According to previous work performed on Ti-6Al-4V, the fracture toughness of titanium with the DMLS process is lower when the notch is oriented in the x-y direction as opposed to the z direction in the as built condition. A study in the literature claims that the tensile residual stress assists in the crack propagation when the crack is oriented in the x-y direction [71]. After stress relief, the toughness increased and properties became more isotropic. After annealing from the as built condition, anisotropy can exist within the structure of Ti-6Al-4V which is indicated by a lower elongation in the z orientation [71]. Thus, it is indicative of microstructural and residual stress changes during post processing.

8.3 Fracture Toughness as a Function of Build Orientation

Fracture toughness K_{IC} and J-integral testing was performed as a function of material condition at different orientations using parameter set from Table 8.1. The samples were

machined to the final dimension according to ASTM E399 [53]. The material which was evaluated included the as built condition, stress relieved, and heat treated conditions. The samples were built in the x, y, and z orientations which correlate to the largest, medium, smallest cross sectional area in contact with the plate (Figure 8.1). K_{IC} was determined for the heat treated specimens. A side grove was needed for the as built and stress relieved samples for J integral because it was too ductile for the linear elastic plain strain condition. J integral fracture toughness is used when the material has high ductility [72]. J_{IC} results were then converted to K_{IC} numbers.

The high fracture toughness for the stress relief and as built condition supports microstructure and tensile observations. The tensile properties show evidence of ductility in the stress relieved and as sintered condition which is supported by the J-integral testing resulting from the fine microstructure of the part. The fracture toughness differences between stress relief and as built condition may be the result of residual stress for the as built part or slight differences in the microstructure resulting from stress relief (Table 8.2). According to the Arch Bridge study in the previous chapter section (7.2), the residual stress was nearly eliminated after stress relief. The results show that the heat treated condition properties are comparable to wrought 4340 steel. There was not a huge difference in the fracture toughness in the as built condition between the three different orientations. Since the fracture zone is near the build plate along with several samples being built simultaneously, there is fairly adequate cooling between each layer. The results indicate that there was no significant concentration of interlayer defects due to uniformity of properties in all three orientations after heat treatment. Future studies will include the

evaluation of fracture toughness as a function of height to determine the effect of cooling of parts.

Table 8.1 Parameter Set used for 4340 Steel

Power Watts	**Hatch Distance** mm	**Laser Scan Speed** mm/sec	**Layer Thickness** Mm	**Stripe Width** mm
185	0.10	700	.02	4

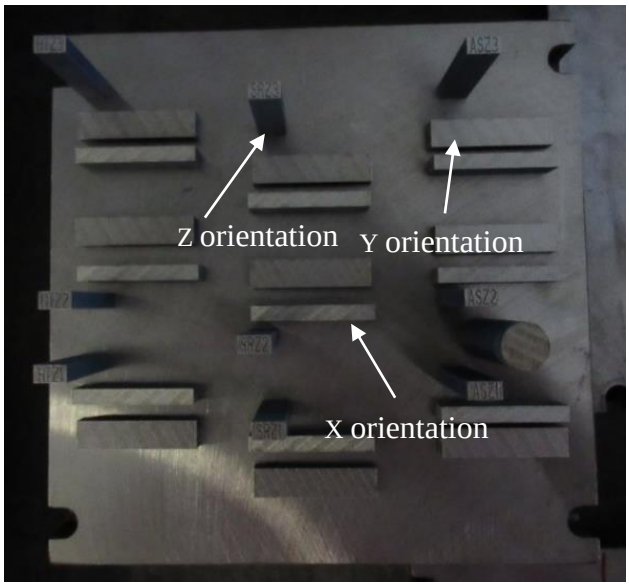

Figure 8.1 Layout of the fracture toughness build where the orientation of components are depicted.

Table 8.2 Fracture Toughness Results as a Function of Condition using Parameter Set from Table 8.1

Sample ID	**Fracture Toughness** (ksi-in$^{.5}$)
As Sintered x	146
As Sintered y	136
As Sintered z	132
Stress Relieved x	153
Stress Relieved y	152
Stress Relieved z	169
Heat Treated x	55
Heat Treated y	54
Heat Treated z	54
Wrought Heat Treated 4340	40 min.

Source: [45].

8.4 Conclusion

The fracture toughness for the as built and stress relieved conditions were ductile and fairly uniform as a function of orientation. Stress relieved parts had a slightly higher fracture toughness than as built condition. Furthermore, there was a very uniform fracture toughness as a function of orientation for specimens in the heat treated condition.

CHAPTER 9

CORROSION RESISTANCE

9.1 Literature Review: Corrosion Resistance Studies

Corrosion is important because it impacts mechanical performance. Tests to assess corrosion resistance include electrochemical potential and atmospheric exposure. Previously, the corrosion resistance of 316L stainless steel produced by powder bed fusion was compared against traditionally manufactured components using accelerated corrosion testing (potential dynamic polarization study) in saline solution. The microstructure was observed optically to assess corrosion properties of the parts. The pore size of the traditionally manufactured component was significantly higher than the laser melted sample after electrochemical testing [73]. The corrosion resistance of the SLM was higher than cast because it has a lower Icorr value. Icorr is the current of the anodic region of the polarization curve. The higher corrosion resistance may be attributed to the finer grains produced by the SLM process.

There was another study on the corrosion resistance on L-PBF, Electron Beam Manufactured (EBM), and wrought Ti-6Al-4V. Potentiodynamic and crevice corrosion were run in simulated body fluid. The L-PBF samples had high corrosion resistance at low voltages (1.2V) which is approximately comparable to levels seen in the body according to Potentiodynamic studies. The improved performance of the L-PBF material maybe due to its high grain boundary density. The EBM samples had the lowest crevice corrosion, but all samples were acceptable. A higher concentration of beta phase may explain the lower crevice corrosion resistance of the L-PBF component [74].

In addition, corrosion resistance of Al10SiMg was evaluated in diluted Harrison's solution. The purpose of this study was to evaluate the corrosion resistance as a function of surface finish, and build orientation. According to the potentiodynamic results, the polished sample had more zone of passivity than as built. The corrosion resistance of shot peened sample was in between as built and polished samples. The x-y had lower corrosion rates than x-z according to Electrical Impedance Spectroscopy (EIS) and Potentiodynamic measurements due to a lower melt pool boundaries concentration. It is likely caused by the preferential corrosion of alpha phase Al in solid solution with silicon at the melt pool boundaries [75].

9.2 Accelerated and Environmental Corrosion Resistance of DMLS 4340

Accelerated and environmental corrosion tests were conducted on stress relieved 4340 steel made by the optimal (LN) and under exposed (LU) sintering conditions as well as the wrought alloy (WR) (Figure 9.1). Based on electrochemical testing in artificial seawater, as can be seen in Figure 9.2, the impedance at a frequency of 10 MHz shows that there is not much of a difference between the three samples. All three materials had a similar response to the phase angle change as a response to the frequencies of the applied potential (Figure 9.3). [76] The potential dynamic scans were relatively similar between the three. The anodic behavior was very similar for all three specimen types because there is not much of a protective barrier in the material (Figure 9.4) [76] . The Ecorr (the potential at which the anodic reaction is equal to the rate of cathodic reactions) and polarization resistance values were relatively similar between the three samples (Tables 9.1-9.2). The microstructure, after electrochemical testing, showed that the under exposed specimen had

the highest porosity (Figure 9.5). The normal sintered specimen had some porosity, but wrought had the lowest porosity according to the microstructure. The non-uniform localized corrosion is likely caused by the initial porosity in the sample [76]. All the samples had similar appearance after salt fog exposure for 1 hour (Figure 9.6) [76] [77]. From preliminary results, the microstructure does not appear to affect the corrosion resistance in saline solution for 4340.

Figure 9.1 Etched Microstructures of 4340 samples, Low porosity parameter (A), under exposed parameters (B), and wrought (C) the scale bar represents 20 microns.
Source: [76].

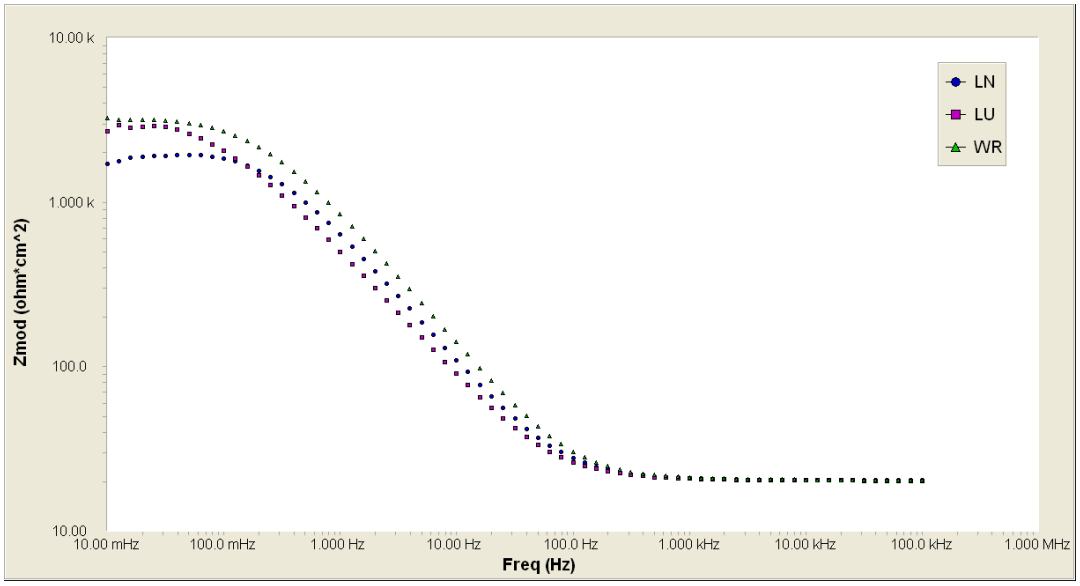

Figure 9.2 EIS-Plot of the modulus of the impedance vs. frequency of 4340 samples.
Source: [76].

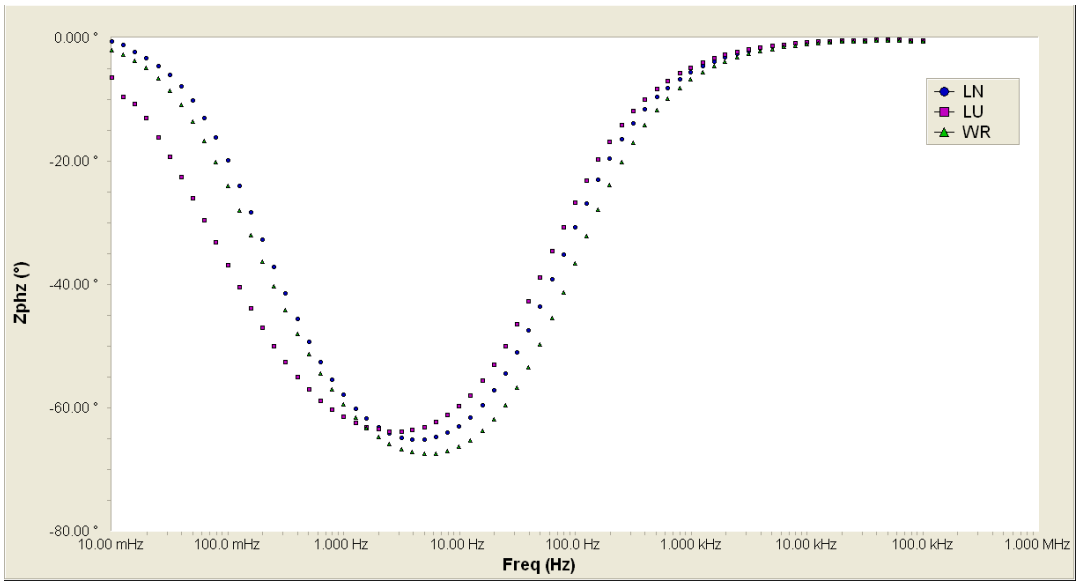

Figure 9.3 4340 EIS results**,** phase angle vs. frequency.
Source: [76].

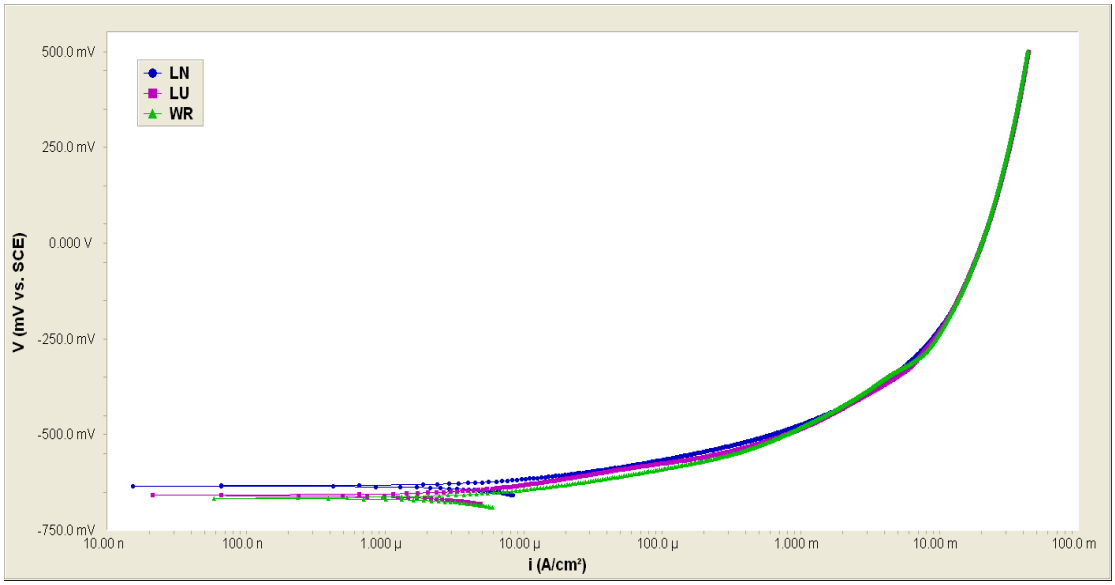

Figure 9.4 Plot of the potentiodynamic scans.
Source: [76].

Table 9.1 Average Results from Polarization Resistance Tests

Type	**Polarization Resistance** (kΩ)	**Current density** (µA/cm^2)	**Corrosion Rate** (mpy)
LN	2.5	10.9	4.9
LU	2.9	8.8	4.1
WR	3.2	8.0	3.6

Source: [76].

Table 9.2 Anodic Polarization Tests

Type	E_{corr} (mV vs SCE)	Current density ($\mu A/cm^2$)	Corrosion Rate (mpy)
LN	-641	5.9	2.7
LU	-664	5.7	2.6
WR	-666	8.5	3.9

Source: [76].

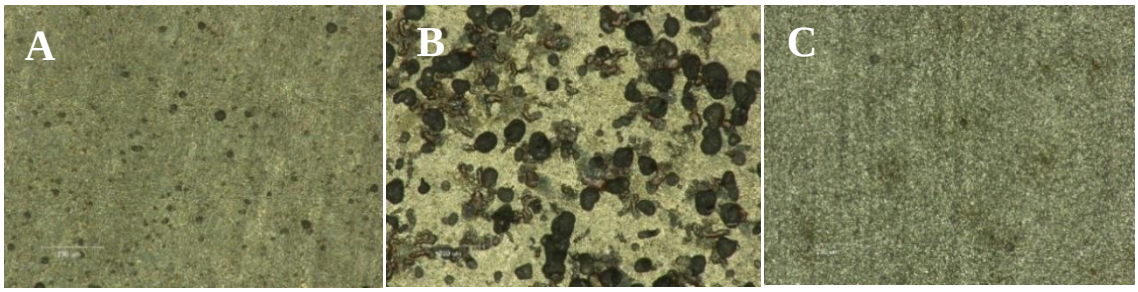

Figure 9.5 4340 microstructures after electrochemical tests: (A) low porosity parameter, (B) under exposed parameters and (C) wrought; the scale bar represents 250 microns. *Source:* [76].

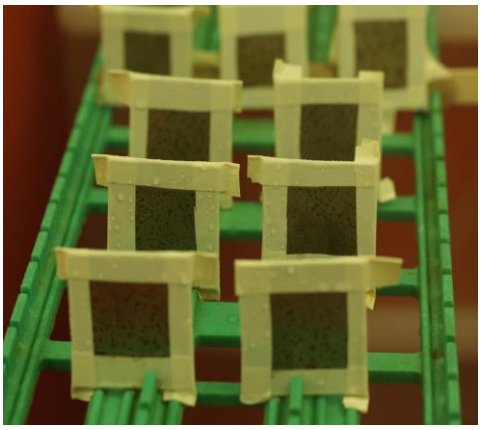

Figure 9.6 Image after 1 hr. salt fog exposure**:** low porosity parameter, under exposed parameters, and wrought.
Source: [76].

CHAPTER 10

CONCLUSION

10.1 Research Findings

The understanding of the DMLS process was established in order to produce parts with mechanical properties on a consistent basis. There were several findings which include the following:

- Several size distributions between 10-53 micron gas atomized 4340 powder provided adequate flow and packing.
- Laser power, scan speed, hatch distance, and stripe width were optimized to produce 4340 and 4140 steel samples with good mechanical properties.
- Gas flow, powder coverage, and filtration is also essential for process repeatability which was demonstrated by verification builds. Repeatability study shows fairly consistent mechanical performance based on the lessons learned from verification builds.
- Mechanical properties and surface roughness vary as a function of build angle for near net shape tensile specimens.
- Anisotropy is based on differences in microstructure and cooling rates between layers.

10.2 Future Work

In process monitoring of the laser, powder coverage, and gas flow is needed to ensure that the process is consistent for the same input parameters. Future work is to employ in situ monitoring techniques for the process such as powder bed imaging and melt pool monitoring to evaluate defects resulting from process anomalies. Anomalies include part deflection, overhanging features, and powder coverage. The challenge is that there will be

significant amount of information which must be interpreted. Thus, it is important to have appropriate standards and specifications in which to employ these techniques.

APPENDIX A

PARAMETER AND POWDER OPTIMIZATION FOR 4340 STEEL

Table A.1-A.3 Reports of density using Archimedes principle and microhardness values for 4340 steel near the optimal laser parameters.

Table A.1 DMLS 4340 Steel (-44+16 Microns) Laser Parameters at 10mm Stripe Width

Sample	**Power** Watts	**Hatch Distance** mm	**Scan Speed** mm/sec	**Density** g/cm^3	**Average Microhardness** HV
1	185	0.1	725	7.83	407.6
2	185	0.1	700	7.82	424.6
3	185	0.1	675	7.80	416.2
4	185	0.1	650	7.82	423.2
5	185	0.11	650	7.79	415
6	185	0.11	625	7.82	424.4
7	185	0.11	600	7.83	417.6
8	185	0.11	575	7.82	423.4
9	185	0.12	600	7.83	405.6
10	185	0.12	575	7.82	427.8
11	185	0.12	550	7.82	414.6
12	185	0.12	525	7.83	409.4
13	185	0.13	575	7.81	424.2
14	185	0.13	550	7.83	460.2
15	185	0.13	525	7.83	422
16	185	0.13	500	7.82	438.6
17	185	0.14	525	7.81	405
18	185	0.14	500	7.82	427.6
19	185	0.14	475	7.82	406.4
20	185	0.14	450	7.81	424
21	195	0.1	750	7.83	415.2
22	195	0.1	725	7.83	431.6
23	195	0.1	700	7.82	416
24	195	0.1	675	7.80	423.8
25	195	0.11	700	7.83	428.8
26	195	0.11	675	7.82	433.8
27	195	0.11	650	7.81	435.8
28	195	0.11	625	7.82	438.8
29	195	0.12	650	7.81	424.6
30	195	0.12	625	7.82	436.2
31	195	0.12	600	7.79	424.2
32	195	0.12	575	7.83	455
33	195	0.13	600	7.82	422.6
34	195	0.13	575	7.81	439.2
35	195	0.13	550	7.78	412.6
36	195	0.13	525	7.77	433
37	195	0.14	550	7.82	415
38	195	0.14	525	7.82	446.6
39	195	0.14	500	7.81	412.6
40	195	0.14	475	7.82	412

Table A.2 DMLS 4340 Steel (-44+22 Microns) Laser Parameters at 10mm Stripe Width

Sample	**Power** W	**Hatch Distance** mm	**Scan Speed** mm/sec	**Density** g/cm^3	**Average Microhardness** HV
1	185	0.1	725	7.78	419.2
2	185	0.1	700	7.81	426.2
3	185	0.1	675	7.83	421.4
4	185	0.1	650	7.79	426
5	185	0.11	650	7.81	429.4
6	185	0.11	625	7.83	421.6
7	185	0.11	600	7.81	422.8
8	185	0.11	575	7.83	422.4
9	185	0.12	600	7.81	427.6
10	185	0.12	575	7.82	422.2
11	185	0.12	550	7.81	413.6
12	185	0.12	525	7.82	429
13	185	0.13	575	7.83	421.6
14	185	0.13	550	7.82	444
15	185	0.13	525	7.83	418.8
16	185	0.13	500	7.82	423.4
17	185	0.14	525	7.58*	413.8
18	185	0.14	500	7.82	428.6
19	185	0.14	475	7.81	415.4
20	185	0.14	450	7.80	423.8
21	195	0.1	750	7.82	411
22	195	0.1	725	7.81	431.8
23	195	0.1	700	7.82	417.6
24	195	0.1	675	7.83	415.2
25	195	0.11	700	7.83	416.2
26	195	0.11	675	7.83	413.4
27	195	0.11	650	7.83	419
28	195	0.11	625	7.82	415.4
29	195	0.12	650	7.82	409.2
30	195	0.12	625	7.83	417.4
31	195	0.12	600	7.83	427.6
32	195	0.12	575	7.83	409
33	195	0.13	600	7.83	432.6
34	195	0.13	575	7.82	421.8
35	195	0.13	550	7.83	435.8
36	195	0.13	525	7.83	404.8
37	195	0.14	550	7.83	413.4
38	195	0.14	525	7.83	419.6
39	195	0.14	500	7.82	432.8
40	195	0.14	475	7.82	414

* Density Greater Than 99 Percent According to Image Analysis

Table A.3 DMLS 4340 Steel (-53+22 Microns) Laser Parameters at 10mm Stripe Width

Sample	**Power** W	**Hatch Distance** mm	**Scan Speed** mm/sec	**Density** g/cm^3	**Average Microhardness** HV
1	185	0.1	725	7.83	419.4
2	185	0.1	700	7.81	441.4
3	185	0.1	675	7.82	426.4
4	185	0.1	650	7.83	458.2
5	185	0.11	650	7.84	445.2
6	185	0.11	625	7.77	437.6
7	185	0.11	600	7.81	436.2
8	185	0.11	575	7.83	423.4
9	185	0.12	600	7.82	435.6
10	185	0.12	575	7.82	429.2
11	185	0.12	550	7.84	470
12	185	0.12	525	7.82	446.2
13	185	0.13	575	7.83	448.8
14	185	0.13	550	7.82	437.4
15	185	0.13	525	7.83	450.2
16	185	0.13	500	7.83	426
17	185	0.14	525	7.83	425.4
18	185	0.14	500	7.83	432.4
19	185	0.14	475	7.83	416.2
20	185	0.14	450	7.82	468.4
21	195	0.1	750	7.83	437.2
22	195	0.1	725	7.83	428.6
23	195	0.1	700	7.83	450.8
24	195	0.1	675	7.83	433.8
25	195	0.11	700	7.83	419.8
26	195	0.11	675	7.82	438.6
27	195	0.11	650	7.83	438.6
28	195	0.11	625	7.83	445.2
29	195	0.12	650	7.83	437.8
30	195	0.12	625	7.83	436
31	195	0.12	600	7.83	444.8
32	195	0.12	575	7.83	437.2
33	195	0.13	600	7.84	443
34	195	0.13	575	7.83	448.4
35	195	0.13	550	7.84	441
36	195	0.13	525	7.83	434.2
37	195	0.14	550	7.83	445.4
38	195	0.14	525	7.83	432
39	195	0.14	500	7.83	449.4
40	195	0.14	475	7.81	451

APPENDIX B

HARDNESS MEASUREMENTS FOR 4340 PARAMETER DEVELOPMENT

Tables B.1 and B.2 evaluated hardness and density for parameter development.

Table B.1 -44+10 Micron 4340 Powder Parameters at 10mm Stripe Width (120-195 Watts)

Sample	**Power** W	**Hatch Distance** mm	**Scan Speed** mm/sec	**Energy Density** J/mm^3	**Average Microhardness** HV
1	120	0.1	400	150	436.4
2	120	0.1	500	120	455.8
3	120	0.1	600	100	465.2
4	120	0.1	700	86	458.6
5	120	0.1	800	75	481.8
6	120	0.1	900	67	498.6
7	120	0.1	1000	60	490.8
8	130	0.1	400	162.5	438.4
9	130	0.1	500	130	442.2
10	130	0.1	600	108.3	454
11	130	0.1	700	92.9	464.6
12	130	0.1	800	81.3	462
13	130	0.1	900	72.2	487.4
14	130	0.1	1000	65	501.6
15	140	0.1	400	175	402.6
16	140	0.1	500	140	432.8
17	140	0.1	600	116.7	450.2
18	140	0.1	700	100	437.4
19	140	0.1	800	87.5	461.8
20	140	0.1	900	77.8	487.6
21	140	0.1	1000	70.0	486.4
22	140	0.1	1100	63.6	483.2
23	150	0.1	400	187.5	406.4
24	150	0.1	500	150	432.2
25	150	0.1	600	125	446
26	150	0.1	700	107.1	447.6
27	150	0.1	800	93.8	456.8
28	150	0.1	900	83.3	460.4
29	150	0.1	1000	75	497.4
30	150	0.1	1100	68.2	481

Table B.1 (Continued) -44+10 Micron 4340 Powder Parameters at 10mm Stripe Width (120-195 Watts)

Sample	**Power** W	**Hatch Distance** mm	**Scan Speed** mm/sec	**Energy Density** J/mm^3	**Average Microhardness** HV
1	160	0.1	500	160	403.2
2	160	0.1	600	133.3	450.8
3	160	0.1	700	114.3	462.6
4	160	0.1	800	100	473
5	160	0.1	900	88.9	488.4
6	160	0.1	1000	80	444
7	160	0.1	1100	72.7	465.8
8	170	0.1	500	170	434.6
9	170	0.1	600	141.7	425.2
10	170	0.1	700	121.4	420.2
11	170	0.1	800	106.3	454.6
12	170	0.1	900	94.4	471.8
13	170	0.1	1000	85	487.2
14	170	0.1	1100	77.3	484.2
15	170	0.1	1200	70.8	467.4
16	170	0.1	1300	65.4	491.6
17	170	0.1	1400	60.7	494.4
18	170	0.1	1500	56.7	497
19	180	0.1	600	150	433
20	180	0.1	700	128.6	461.8
21	180	0.1	800	112.5	455.4
22	180	0.1	900	100	477.4
23	180	0.1	1000	90	466.6
24	180	0.1	1100	81.8	471.8
25	195	0.1	700	139.3	457.8
26	195	0.1	800	121.8	478.4
27	195	0.1	900	108.3	483
28	195	0.1	1000	97.5	466.8
29	195	0.1	1100	88.6	475.6

Table B.2 Hardness and Density of the Parameters for -44+10 Micron Powder at 175-195 Watts and 10mm Stripe Width

Sample	Power W	Hatch Distance mm	Scan Speed mm/sec	Density g/cm^3	Average Microhardness HV
1	175	0.07	800	7.79	454.2
2	175	0.07	850	7.83	452.2
3	175	0.07	900	7.82	461.4
4	175	0.07	950	7.82	446.6
5	175	0.07	875	7.85	456.4
6	175	0.07	925	7.83	432.2
7	175	0.07	1000	7.82	419.6
8	175	0.08	700	7.83	450.6
9	175	0.08	750	7.83	447.8
10	175	0.08	775	7.84	449.4
11	175	0.08	800	7.82	445.5
12	175	0.08	850	7.83	432.6
13	175	0.08	900	7.83	450
14	175	0.09	625	7.83	456.4
15	175	0.09	650	7.83	463.3
16	175	0.09	675	7.83	454.2
17	175	0.09	700	7.83	452.8
18	175	0.09	750	7.84	469.2
19	175	0.09	800	7.83	457
20	175	0.1	550	7.83	431.6
21	175	0.1	600	7.81	432.4
22	175	0.1	625	7.83	437.6
23	175	0.1	650	7.82	459.0
24	175	0.1	700	7.83	451.8
25	175	0.1	750	7.83	462.8
26	175	0.11	500	7.83	456.8
27	175	0.11	550	7.83	441.6
28	175	0.11	575	7.83	453.4
29	175	0.11	600	7.83	433.6
30	175	0.11	650	7.83	446.4
31	175	0.11	700	7.84	429.2
32	175	0.12	475	7.83	427.8
33	175	0.12	500	7.83	437.4
34	175	0.12	525	7.83	421.8
35	175	0.12	550	7.82	429.2
36	175	0.12	600	7.82	449
37	175	0.12	625	7.83	430.2

Table B.2 (Continued) Hardness and Density of the Parameters for -44+10 Micron Powder at 175-195 Watts and 10mm Stripe Width

Sample	**Power** W	**Hatch Distance** mm	**Scan Speed** mm/sec	**Density** g/cm^3	**Average Microhardness** HV
1	185	0.07	850	7.79	458.4
2	185	0.07	900	7.83	452.0
3	185	0.07	925	7.82	461.8
4	185	0.07	950	7.83	438.6
5	185	0.07	1000	7.82	446.4
6	185	0.07	1050	7.83	456.0
7	185	0.08	750	7.83	409.25
8	185	0.08	800	7.83	457.8
9	185	0.08	825	7.83	432
10	185	0.08	850	7.83	448
11	185	0.08	900	7.84	430
12	185	0.08	950	7.83	430.8
13	185	0.09	650	7.83	448.6
14	185	0.09	700	7.82	462.6
15	185	0.09	725	7.83	430.0
16	185	0.09	750	7.82	437.6
17	185	0.09	800	7.83	431.0
18	185	0.09	850	7.83	451.2
19	185	0.1	575	7.83	460.4
20	185	0.1	600	7.83	461.2
21	185	0.1	650	7.83	451.4
22	185	0.1	675	7.83	452.6
23	185	0.1	700	7.83	455.0
24	185	0.1	750	7.83	468.8
25	185	0.11	550	7.83	463.6
26	185	0.11	575	7.80	458.4
27	185	0.11	600	7.83	429.6
28	185	0.11	625	7.82	425.8
29	185	0.11	650	7.83	438.4
30	185	0.11	700	7.83	440.6
31	185	0.12	500	7.82	437
32	185	0.12	525	7.82	436.8
33	185	0.12	550	7.82	424.8
34	185	0.12	575	7.83	435
35	185	0.12	600	7.82	434.4
36	185	0.12	625	7.81	439

Table B.2 (Continued) Hardness and Density of the Parameters for -44+10 Micron Powder at 175-195 Watts and 10mm Stripe Width

Sample	Power W	Hatch Distance mm	Scan Speed mm/sec	Density g/cm^3	Average Microhardness HV
1	195	0.07	875	7.82	422.6
2	195	0.07	900	7.83	443
3	195	0.07	950	7.83	430.6
4	195	0.07	975	7.83	420.4
5	195	0.07	1000	7.83	433.4
6	195	0.07	1050	7.83	429.8
7	195	0.08	775	7.83	435.2
8	195	0.08	800	7.83	426
9	195	0.08	850	7.83	432.4
10	195	0.08	875	7.83	436.8
11	195	0.08	900	7.83	422.6
12	195	0.08	950	7.83	438.8
13	195	0.09	675	7.83	442.4
14	195	0.09	700	7.83	445.4
15	195	0.09	750	7.83	456.2
16	195	0.09	775	7.82	444.2
17	195	0.09	800	7.82	475.4
18	195	0.09	850	7.84	453.8
19	195	0.1	625	7.83	399
20	195	0.1	650	7.81	452.4
21	195	0.1	675	7.82	432.2
22	195	0.1	700	7.82	444.2
23	195	0.1	750	7.82	421.4
24	195	0.1	825	7.83	391.2
25	195	0.11	550	7.82	421.6
26	195	0.11	600	7.83	431.6
27	195	0.11	625	7.83	444.8
28	195	0.11	650	7.82	431.4
29	195	0.11	675	7.83	434.8
30	195	0.11	700	7.83	437.6
31	195	0.12	500	7.82	450.8
32	195	0.12	550	7.82	459.8
33	195	0.12	575	7.81	458.2
34	195	0.12	600	7.82	487.4
35	195	0.12	625	7.82	465.4
36	195	0.12	650	7.82	446.4

APPENDIX C

HARDNESS MEASUREMENTS FOR 4140 PARAMETER EVALUATION

Initial parameter evaluation for 4140 steel.

Table C.1 DMLS 4140 Steel -44+10 Micron Parameters at 4mm Stripe Width and 0.02mm Layer Thickness

Sample	**Power** W	**Hatch Distance** mm	**Scan Speed** mm/sec	**Average Microhardness** HV
1	185	0.1	700	459
2	185	0.1	675	464
3	185	0.1	650	416.8
4	185	0.1	625	444.6
5	185	0.11	650	413.8
6	185	0.11	625	420.8
7	185	0.11	600	404.6
8	185	0.11	575	405.2
9	185	0.12	600	415
10	185	0.12	575	437.2
11	185	0.12	550	431.8
12	185	0.12	525	427
13	185	0.13	550	413.6
14	185	0.13	525	423
15	185	0.13	500	413.8
16	185	0.13	475	411.6
17	185	0.14	525	411.6
18	185	0.14	500	424.2
19	185	0.14	475	414.6
20	185	0.14	450	406.4
21	195	0.1	750	422.6
22	195	0.1	725	423.4
23	195	0.1	700	433.8
24	195	0.1	675	438
25	195	0.11	675	415.4
26	195	0.11	650	424.6
27	195	0.11	625	401.6
28	195	0.11	600	426.4
29	195	0.12	575	406.6
30	195	0.12	600	419.6
31	195	0.12	575	411.2
32	195	0.12	550	416.4
33	195	0.13	575	417.4
34	195	0.13	550	420.8
35	195	0.13	525	420.2
36	195	0.13	500	416.8
37	195	0.14	550	416
38	195	0.14	525	438.6
39	195	0.14	500	421.4
40	195	0.14	475	414.4

REFERENCES

[1] H. Gu, H. Gong, D. Pal, K. Rafi, T. Starr and B. Stucker, "Influences of Energy Density on Porosity and Microstructure of Selective Laser Melted 17-4 Stainless Steel," in *Solid Freeform Fabrication* , Austin, TX, 2013.

[2] E. Jelis, M. Clemente, S. Kerwien, R. Nuggehalli and M. R. Hespos, "Metallurgical and Mechanical Evaluation of 4340 Steel Produced by Direct Metal Laser Sintering," *The Journal of Minerals, Metals, and Material Society* , vol. 67, no. 3, pp. 582-589, 2015.

[3] A. Simchi, F. Petzoldt and H. Pohl, "On the Development of Direct Metal Laser Sintering for Rapid Tooling," *Journal of Materials Processing Technology,* vol. 141, no. 3, pp. 319-328, 2003.

[4] N. Contuzzi, S. L. Campanelli, C. Casavola and L. Lamberti, "Manufacturing and Characterization of 18Ni Marage 300 Lattice Components by Selective Laser Melting," *Materials,* vol. 6, pp. 3451-3468, 2013.

[5] M. Mazur, M. Leary, M. McMillan, J. Elambasseril and M. Brandt, "SLM Additive Manufacture of H13 Tool Steel with Conformal Cooling and Structural Lattices," *Rapid Prototyping Journal,* pp. 504-518, 2016.

[6] M. Baumers, C. Tuck, R. Wildman, I. Ashcroft, E. Rosamond and R. Hague, "Combined Build-Time, Energy Consumption and Cost Estimation for Direct Metal Laser Sintering," in *Solid Freeform Fabrication Symposium*, Austin, TX, 2012.

[7] T. C. Allison, J. Moore, A. M. Rimpel, J. C. Wilkes, R. Pelton and K. Wygant, "Manufacturing and Testing Experience with Direct Metal Laser Sintering for Closed Centrifugal Compressor Impellars," in *Pump and Turbo 2014*, Houston, TX, 2014.

[8] A. Hussein, L. Hao, Y. Chunze, R. Everson and P. Young, "Advanced Lattice Support Structures for Metal Additive Manufacturing," *Journal of Materials Processing Technology,* pp. 1019-1026, 2013.

[9] Y. Liu, Y. Yang and D. Wang, "A Study on the Residual Stress During Selective Laser Melting (SLM) of Metal Powder," *International Journal of Advanced Manufacturing Technology* , 2015.

[10] R. Udroiu, "Powder Bed Additive Manufacturing Systems and Its Application," *Academic Journal of Manufacturing Engineering*, vol. 10, no. 4, pp. 122-129, 2012.

[11] B. A. Fulcher, D. K. Leigh and T. J. Watt, "Comparison of AlSi10Mg and Al 6061 Processed Through DMLS," in *Solid Freeform Fabrication*, Austin, TX, 2014.

[12] M. L. M. Sistiaga, R. Mertens, B. Vracken, X. Wang, B. Van Hooreweder, J.-P. Kruth and J. Van Humbeeck, "Changing the Alloy Composition of Al7075 for Better Processability by Selective Laser Melting," *Journal of Materials Processing Technology 238 (2016) 437–445*, vol. 238, pp. 437-445, 2016.

[13] H. K. Rafi, D. Pal, N. Patil, T. L. Starr and B. Stucker, "Microstructure and Mechanical Behavior of 17-4 Precipitation Hardenable Steel Processed by Selective Laser Melting," *Journal of Materials Engineering and Performance*, vol. 23, no. 12, pp. 4221-4228, 2014.

[14] E. Yasa, K. Kempen and J.-P. and Kruth, "Microstructure and Mechanical Properties of Maraging Steel 300 After Selective Laser Melting," in *Solid Freeform Fabrication*, Austin, TX, 2010.

[15] E. G.-E. O. System, "Material Data Sheet- EOS Maraging Steel MS1," 2011. [Online]. Available: http://www.eos.info/material-m. [Accessed 23 September 2015].

[16] P. M. Novotny and G. E. Maurer, "Ultra-High-Strength Steels Vs. Titanium Alloys," in *Advanced Materials & Processes*, Materials Park, OH, ASM International, 2007, pp. 37-40.

[17] Incodema Group, "DMLS Materials Comparison Chart," [Online]. Available: http://www.unmannedsystemstechnology.com/wp-content/uploads/2014/06/DMLS-Materials-Chart.pdf. [Accessed 23 September 2015].

[18] AK Steel Corporation, " Produce Data Bulletin 15-5 PH Stainless Steel," 2007. [Online]. Available:

http://www.aksteel.com/pdf/markets_products/stainless/precipitation/15-5_ph_data_sheet.pdf. [Accessed 23 September 2015].

[19] ASM International, "UNILOY 17-4: Age Hardenable Martensitic Stainless Steel," December 1981. [Online]. Available: http://products.asminternational.org/hbk/index.jsp. [Accessed 23 September 2015].

[20] C. T. Schade, T. F. Murphy and C. Walton, "Development of Atomized for Additive Manufacturing," [Online]. Available: http://www.gkn.com/hoeganaes/media/Tech%20Library/Schade-Atomized%20Powders%20for%20Additive%20Manufacturing%20(1).pdf. [Accessed 23 September 2015].

[21] R. Li, L. Jinhui, S. Yusheng and L. Wang, "Balling Behavior of Stainless Steel and Nickel Powder During Selective Laser Melting Process," *International Journal of Advanced Manufacturing Technologies*, vol. 59, pp. 1025-1035, 2012.

[22] N. Karapatis, G. Egger, P. Gygax and R. Glardon, "Optimization of Powder Layer Density in Selective Laser Sintering," in *Solid Freeform Fabrication*, Austin, TX, 1999.

[23] J. D. Hunter, D. C. J and D. J. Novatnak, "Benefits of Using Powder Metal Advanced Materials for Rolling Mill Applications," 2012. [Online]. Available: www.rolldesigns.com/.../CPP_IRD_Presentation_Spring_2012_Mtg.ppt. [Accessed 20 July 2015].

[24] B. Liu, R. Wildman, C. Tuck, I. Ashcroft and R. Hague, "Investigation the Effect of Particle Size Distribution on Process Parameter Optimisation in Selective Laser Melting Process," in *Solid Freeform Fabrication*, Austin, TX, 2011.

[25] A. B. Spierings and G. Levy, "Comparison of Density of 316L Parts Produced with SLM using Different Powder Grades," in *Solid Freeform Fabrication*, Austin, TX, 2009.

[26] A. B. Spierings, N. Herres and G. Levy, "Influence of the Particle Size Distribution on Surface Quality and Mechanical Properties in Additive Manufactured Stainless Steel Parts," in *Solid Freeform Fabrication*, Austin, TX, 2010.

[27] E. Jelis, R. Sadangi, M. Hespos, S. Kerwien, M. Clemente and N. Ravindra, "DMLS (Direct Metal Laser Sintering) 4340 Steel: Influence of Starting Particle Size," in *Materials Science and Technology*, Columbus, OH, 2015.

[28] M. Simonelli, C. Tuck, N. T. Aboulkhair, I. Maskery, I. Ashcroft, R. D. Wildman and R. Hague, "A Study on the Laser Spatter and the Oxidation Reactions During Selective Laser Melting of 316L Stainless Steel, Al-Si10-Mg, and Ti-6Al-4V," *Metallurgical and Materials Transactions A*, vol. 46A, pp. 3842-3851, 2015.

[29] M. Maalekian, "The Effects of Alloying Elements on Steel," Technische Universität Graz, Graz, Austria, 2007.

[30] T. Nakamoto, S. Nobuhiko, Y. Miyata and H. Inui, "Selective Laser Sintering of High Carbon Steel Powders as a Function of Carbon Content," *Journal of Materials Processing Technology*, vol. 209, pp. 5653-5660, 2009.

[31] J. J. S. Dilip, B. Stucker and T. L. Starr, "Effects of Process Parameter and Heat Treatment on the Microstructure and Mechanical Properties of SLM-Built HY100 Steel," in *Solid Freeform Fabrication*, Austin, 2014.

[32] M. A. Anam, J. Dilip, D. Pal and B. Stucker, "Effect of Scan Pattern on the Microstructural Evolution of Inconel 625 during Selective Laser Melting," in *Solid Freeform Fabrication*, Austin, 2014.

[33] H. Boyer, Atlas of Isothermal Transformation and Cooling Transformation Diagrams, American Society of Metals, 1977.

[34] M. Samler, "Jominy End Quenching of 4140 Steel: The Effect of Time and Temperature on Austenitic Grain Growth," Worcester Polytechnic Instsitute, Worcester, MA, 2010.

[35] E. Ripling and P. Crosley, "Crack Arrest Toughness of 4140, 1340, and 4340 Steel," Materials Research Laboratory Inc., Glenwood, IL, 1981.

[36] D. Gu and Y. Shen, "Processing Conditions and Microstructural Features of Porous 316L Stainless," *Applied Surface Science*, vol. 255, pp. 1880-1887, 2008.

[37] G. Kasperovich, J. Haubrich, J. Gussont and G. Requena, "Correlation Between Porosity and Processing Parameters in TiAl64V Produced by Selective Laser Melting," *Materials and Design*, vol. 105, pp. 160-170, 2016.

[38] E. Jelis, S. Kerwien, N. M. Ravindra and M. Clemente, "Development of Low Alloy High Strength Steel Process Parameters for Direct Metal Laser Sintering," in *Materials Science and Technology*, Pittsburgh, PA, 2015.

[39] M. Tang and P. C. Pistorius, "Oxides, Porosity and Fatigue Performance of AlSi10Mg Parts Produced by Selective Laser Melting," *International Journal of Fatigue*, 2016.

[40] M. Jamshidinia, A. Sadek, W. Wang and S. Kelly, "Additive Manufacturing of Steel Alloys Using Laser Powder-Bed Fusion," ASM International, January 2015. [Online]. Available: http://www.asminternational.org/documents/10192/23429018/amp17301p20.pdf/8e97d8d6-90fa-41a4-96b4-ef0b3c3e606f.

[41] M. Frey, M. Shellabear and L. Thorsson, "Mechanical Testing of DMLS Parts," [Online]. Available: http://gpiprototype.com/files/dmls/Whitepaper%20-%20Mechanical%20Testing%20of%20DMLS%20Parts.pdf. [Accessed 21 July 2015].

[42] ASTM E8/E8M, "Standard Test Methods for Tension Testing of Metallic Materials," ASTM International, Conshohocken, 2015.

[43] "AISI 4340 Steel, normalized, 13mm (0.5 in) round," MatWeb, [Online]. Available: http://www.matweb.com/search/DataSheet.aspx?MatGUID=948f14a1d835445ab11c681ddb1bc2c6&ckck=1. [Accessed 2015].

[44] H. Gong, H. Gu, K. Zeng, J. Dilip, D. Pal, B. Stucker, D. Christiansen, J. Beuth and J. J. Lewandowski, "Melt Pool Characterization for Selective Laser Melting of Ti-6Al-4V Pre-alloyed Powder," in *Solid Freeform Fabrication*, Austin, TX, 2014.

[45] E. Jelis, M. R. Hespos and N. M. Ravindra, "Evaluation of Structure and Properties of 4340 Steel Produced by DMLS Process," *Journal of Materials Engineering and Performance,* (Submitted for Publication).

[46] W. Wang and S. Kelly, "A Metallurgical Evaluation of the Powder-Bed Laser Additive Manufactured 4140 Steel Material," *The Journal of Minerals, Metals, and Material Society* , vol. 68, no. 3, pp. 869-875, 2016.

[47] ASTM E23, "Standard Test Methods for Notched Bar Impact Testing of Metallic Materials," ASTM International, West Conshohocken, PA, 2012.

[48] L. C. Ardila, F. Garciandia, J. González-Díaz, P. Álvarez, A. Echeverria, M. M. Petite, R. Deffley and J. Ochoa, "Effect of IN718 Recycled Powder Reuse on Properties of Parts Manufactured by Means of Selective Laser Melting," *Physics Procedia* , vol. 56, pp. 99-107, 2014.

[49] V. Seyda, N. Kaufmann and C. Emmelmann, "Investigation of Aging Processes of Ti-6Al-4V Powder Material in Laser Melting," *Physics Procedia* , vol. 39, pp. 425-431, 2012.

[50] W. E. Luecke and J. A. Slotwinski, "Mechanical Properties of Austenitic Stainless Steel Made by Additive Manufacturing," *Journal of Research of the National Institute of Standards and Technology,* vol. 119, pp. 398-418, 2014.

[51] A. Yadollahi, N. Shamsaei, S. M. Thompson, A. Elwany and L. Bian, "Effects of Building Orientation and Heat Treatment on Fatigue Behavior of Selective Laser Melted 17-4 PH Stainless Steel," *International Journal of Fatigue,* pp. 1-18, 2016.

[52] M. Wei Wu, P. Hsin Lai and J. Kuang Chen, "Anisotropy in the Impact Toughness of Selective Laser Melted Ti–6Al–4V alloy," *Materials Science & Engineering A,* vol. 650, p. 295–299, 2016.

[53] ASTM E399 - 12e3, "Standard Test Method for Linear-Elastic Plane-Strain Fracture Toughness KIc of Metallic Materials," ASTM International, West Conshohocken, PA.

[54] S. Moylan, J. Slotwinski, A. Cooke, K. Jurrens and M. A. Donmez, "Lesson Learned in Establishing the NIST Metal Additive Manufacturing Laboratory," National Institute of Standards and Technology, Gaithersburg, MD, 2013.

[55] B. Ferrar, L. Mullen, E. Jones, R. Stamp and C. J. Sutcliffe, "Gas Flow Effects on Selective Laser Melting (SLM) Manufacturing Performance," *Journal of Materials Processing Technology,* vol. 212, pp. 355-364, 2011.

[56] M. J. Matthews, G. Guss, S. A. Khairallah, A. M. Rubenchik, P. J. Depond and W. E. King, "Denudation of Metal Powder Layers in Laser Powder Bed Fusion Processes," *Acta Materialia* , vol. 114, pp. 33-42, 2016.

[57] H. Mishler, R. Moroe and P. Rieppel, "Welding of High Strength Steels for Aircraft and Missile Applications," Defense Metals Information Center, Columbus, OH, 1959.

[58] R. O'Leary, R. Setchi, P. Prickett, G. Hankins and N. Jones, "An Investigation into the Recycling of Ti-6Al-4V Powder Used Within SLM to Improve Sustainability," *Sustainable Design and Manufacturing 2015,* pp. 377-388, 2015.

[59] A. S. Wu, D. W. Brown, M. Kumar, G. F. Gallegos and W. E. King, "An Experimental Investigation into Additive Manufacturing- Induced Residual Stresses in 316L Stainless Steel," *Metallurgical and Materials Transactions,* vol. 45, no. 13, pp. 6260-6270, 2014.

[60] S. Kleszczynski, A. Ladewig, K. Friedberger, J. Zur Jacobsmühlen, D. Merhof and G. Witt, "Position Dependency of Surface Roughness in Parts From Laser Beam Melting Systems," in *Solid Freeform Fabrication*, Austin, TX, 2015.

[61] B. AlMangour and J.-M. Yang, "Improving the Surface Quality and Mechanical Properties by Shot-Peening of 17-4 Stainless Steel Fabricated by Additive Manufacturing," *Materials & Design*, 2016.

[62] W. Everhart, E. Sawyer, T. Neidt, T. Dinardo and B. Brown, "The Effect of Surface Finish on Tensile Behavior of Additively Manufactured Tensile Bars," *Journal of Materials Science,* vol. 51, p. 3836–3845, 2016.

[63] T. M. Mower and M. J. Long, "Mechanical Behavior of Additive Manufactured Powder Bed of Laser Fused Materials," *Materials Science & Engineering A* , vol. 651, pp. 198-213, 2016.

[64] K. Kempen, L. Thijs, B. Vrancken, S. Buls, J. Van Humbeeck and J.-P. Kruth, "Producing Crack-Free, High Density M2 HSS Parts by Selective Laser Melting: Pre-Heating the Baseplate," in *Solid Freeform Fabrication*, Austin, TX, 2013.

[65] M. F. Zaeh and G. Branner, "Investigations on Residual Stresses and Deformations in Selective Laser Melting," *Production Engineering Research & Development,* vol. IV, pp. 35-45, 2010.

[66] H. Pohl, A. Simchi, M. Issa and H. Dias, "Thermal Stresses in Direct Metal Laser Sintering," in *Solid Freeform Fabrication,* Austin, TX, 2001.

[67] J.-P. Kruth, M. Badrossamay, E. Yasa, J. Deckers, L. Thijs and J. Van Humbeeck, "Part and Material Properties in Selective Laser Melting of Metals," in *16th International Symposium on Electromachining,* Shanghai, China, 2010.

[68] A. Simchi, "Direct Laser Sintering of Metal Powders: Mechanism, Kinetics, and Microstructural Features," *Materials Science & Engineering A,* vol. 42, no. 148-158, pp. 148-158, 2006.

[69] B. Vrancken, R. Wauthle, J.-P. Kruth and J. Van Humbeeck, "Study of the Influence of Material Properties on Residual Stress," in *Solid Freeform Fabrication,* Austin, TX, 2013.

[70] L. Parry, I. A. Ashcroft and R. D. Wildman, "Understanding the Effect of Laser Scan Strategy on Residual Stress in Selective Laser Melting Through Thermo-Mechanical Simulation," *Additive Manufacturing,* vol. 12, pp. 1-15, 2016.

[71] V. Cain, L. Thijs, J. Van Humbeeck, B. Van Hooreweder and R. Knutsen, "Crack Propagation and Fracture Toughness of Ti6Al4V Alloy Produced by Selective Laser Melting," *Additive Manufacturing,* vol. 5, pp. 68-76, 2014.

[72] X.-K. Zhu and J. A. Joyce, "Review of Fracture Toughness (G, K, J, CTOD,CTOA) Testing and Standardization," *Engineering Fracture Mechanics,* vol. 85, pp. 1-46, 2012.

[73] K. Anthony and S. Prasad, "A Comparison of Corrosion Resistance of Stainless Steel Fabricated with Selective Laser Melting and Conventional Processing," *International Journal of ChemTech Research,* vol. VI, no. 7, pp. 2632-2635, 2014-2015.

[74] Z. Bingjing, W. Hong, Q. Ning, W. Chao and H. Min, " Corrosion Resistance Characteristics of a Ti-6Al-4V Alloy Scaffold that is Fabricated by Electron Beam Melting and Selective Laser Melting for Implantation in Vivo," *Materials Science & Engineering C,* 2016.

[75] M. Cabrini, S. Lorenzi, T. Pastore, S. Pellegrini, D. Manfredi, P. Fino, S. Biamino and C. Badini, "Evaluation of Corrosion Resistance of Al–10Si–Mg Alloy Obtained by Means of Direct Metal Laser Sintering," *Journal of Materials Processing Technology* , vol. 231, pp. 326-335, 2016.

[76] D. P. Schmidt, E. Jelis and M. Clemente, "Corrosion of 3D Printed Steel," in *Materials Science and Technology*, Columbus, OH, 2015.

[77] ASTM B117-16, "Standard Practice for Operating Salt Spray (Fog) Apparatus," ASTM International, West Conshohocken, PA.